UNIVERSIDADE ESTADUAL DE CAMPINAS
INSTITUTO DE FÍSICA
GLEB WATAGHIN

13

PROPRIEDADES ÓPTICAS DE NANOESTRUTURAS DE Si/Ge

FERNANDO CERDEIRA

DEPARTAMENTO DE FÍSICA
DO ESTADO SÓLIDO E
CIÊNCIA DOS MATERIAIS

INSTITUTO DE FÍSICA
"GLEB WATAGHIN"

UNICAMP

notas de física ifgw

1997

Capitulo VI: Optical Properties

(Fernando Cerdeira)

do livro:

"Ge-Si Science and Technology"

(Robert Hull and John C. Bean editors)

Um volume na serie:

Semiconductors and Semimetals

(R.K. Willardson and A.C. Beer editors,Academic Press, NY)

Optical Properties

Fernando Cerdeira

Instituto de Física "Gleb Wataghin"

Universidade Estadual de Campinas, UNICAMP

13083-970 Campinas, São Paulo, Brasil

(November 1, 1997)

CONTENTS

I. INTRODUCTION

The optical properties of semiconductors have provided rich information on such diverse aspects of their physical properties as their electronic and vibrational states, the existence and nature of defects and impurities etc. In the particular case of semiconductor heterostructures, some optical techniques have provided information about their structure (super-peridocities, layer thicknesses etc.) and that of their interfaces.

Light incident on a semiconductor surface is partly reflected and partly transmitted. The reflected light carries information about the electronic states of the material. Part of the light that enters the semiconductor is absorbed or scattered while the remainder is transmitted, if the sample is thin enough. The energy from the absorbed radiation can be dissipated (absorption) or re-emitted as photons of different frequencies (photoluminiscence). Photons can also be inelastically scattered by creating or annihilating elementary excitations within the semiconductor (Brillouin or Raman Scattering). By now, so much information has accumulated about these forms of interaction of electromagnetic radiation with semiconductors and other materials, that good accounts of the basic physics and experimental details involved in this interactions can be found many textbooks and review articles [1–4].We shall not attempt to duplicate this work. Rather, we shall give brief introductory descriptions of the optical techniques which have most contributed to the understanding of the properties of Si/Ge heterostructures. We shall offer this introduction in the sections of this chapter dedicated to the discussion of the results obtained by a given technique. Thus, section II is dedicated to discussing techniques based on reflectivity or absorption of light, section III describes the results of inelastic light sacattering and section IV is devoted to photoluminiscence. Finally, in section V we try to summarize the main points developed in the previous sections. Since sometimes several techniques have contributed to the understanding of a given issue, this division into sections is not ironclad and the results from several techniques must be discussed together. In doing so, the results from techniques which have not yet been introduced are summarized, postponing more detailed discussions to the appropriate

subsection.

II. FORMS OF DIFFERENTIAL SPECTROSCOPY BASED ON REFLECTION OR ABSORPTION OF LIGHT

A. General Considerations

The quantities experimentally determined by these techniques are related to the real $[\varepsilon_1(\omega)]$ and imaginary $[\varepsilon_2(\omega)]$ parts of the dielectric constant. The latter is sensitive to processes in which a photon is absorbed, lifting an electron from the valence into the conduction band. In these processes the total crystal momentum is conserved. Since the wave vector of the light is very small, compared to electronic wavevectors inside the Brillouin Zone (BZ), such transitions are essentially vertical and connect conduction and valence band states of virtually the same **k**-vector. Peaks and shoulders appear in $\varepsilon_2(\omega)$ when the joint density of states of the bands involved in the transitions have singularities. These peaks and shoulders can be correlated to similar structures appearing in the reflectivity, $R(\omega)$, or the absorption coefficient, $\alpha(\omega)$, of the material. The photon-energy at which these structures appear give precise values for the energy difference between valence and conduction band states at important symmetry points (or along symmetry axes) of the BZ, at which the joint density of states is singular (van Hove singularities) [1–5]. As an example we show in fig.1 the band structure of bulk Ge. In this figure the various electronic transitions responsible for structure in the optical properties are indicated. The most prominent structures in the optical coefficients are given names such as E_0 (direct transitions at the BZ center), E_1 (direct transitions along the (111) axis in the BZ) etc. Table I lists their transition energies for bulk Si and Ge [1]. Notice that in both these materials the fundamental gap is indirect, so that optical transitions across this gap must be assisted by large-wavevector phonons in order to conserve crystal momentum. Hence, these transitions provide only weak contributions to the optical constants. These show clear structures only for direct transi-

tions [fig.2].In the upper curve of fig.2 we display the reflectivity of this material. As we can see, not all the vertical transitions indicated in fig.1 show up clearly in the reflectivity spectrum of fig.2(a). During the sixties several techniques were developed for modulating either some sample parameter or the incoming or outgoing beams. These modulations produce spectra which are related to some derivative of the dielectric function. The process of differentiation suppresses uninteresting backgrounds and produces sharp structures in the photon-energy region of the optical singularities. This point is illustrated in fig.2(b), where the electro-refelctivity spectrum of bulk Ge is shown. In this technique an ac-electric field modulates the optical properties of the material and the resulting spectrum is related to the third derivative of the dielectric function [6,7]. Bumps and shoulders in $R(\omega)$ (upper curve) are highlighted in the modulated refelctivity spectrum (lower curve). The latter gives good resolution of critical points which are almost invisible in the plain refelectivity spectrum. Because of this advantage, modulation spectroscopy had a decisive influence in understanding the band structure of bulk semiconductors. Most of the work in this area was performed in the sixties and early seventies and has been extensively reviewed [5,7]. With the advent of semiconductor microstructures, there was a revival of interest in these techniques. Their applications to semiconductor superlattices and quantum wells have been recently reviewed by several authors [8–10] . Of particular importance have been the techniques of photo- and electro-modulated reflectivity , in which an electric field is modulated within the sample by either depositing a semi-transparent metal layer on the sample surface and applying an ac-voltage between the front and the back of the sample or by photo-injecting carriers by a modulated secondary beam. The measured quantity is the ratio between the modulated (ΔR) and the *dc*- parts of the reflectivity (R). This is related to the third derivative of the dielectric constant and is well represented by a, now, standard lineshape function [7]:

$$\frac{\Delta R}{R} = \sum_j \mathrm{Re}\left\{ \frac{C_j e^{i\phi_j}}{[(\hbar\omega - E_j) + i\Gamma_j]^n} \right\} \quad , \tag{1}$$

where each term in the sum corresponds to a critical point, of energy (lifetime broadening) E_j (Γ_j); C_j and ϕ_j are amplitude and phase factors, respectively, of the transition.The

exponent n depends on the type of critical point.. Choosing a value of this parameter for SLs and QWs has been the subject of much debate [10]. However, the value obtained for the critical energies by fitting the experimental data with eq(1) is remarkably independent of this choice. The usefulness of this technique depends greatly on this feature of ER and PR lineshapes.

An oblique angle of incidence technique which has been very useful in the last decade or so is that of spectroscopic ellipsometry. Its name refers the fact that when linearly polarized light, which is neither polarized parallel or perpendicularly to the plane of incidence, is reflected obliquely from the semiconductor surface it emerges elliptically polarized. By determining the orientation and the ratio of the polarization ellipse axes, the real and imaginary parts of the dielectric constant can be obtained. Because of present day accuracy in these measurements, numerical differentiation of $\varepsilon(\omega)$ can be performed which produces similar results to those of modulation spectroscopy [1,7]. This is illustrated in fig.3, where the third derivative of $\varepsilon_2(\omega)$, taken from ellipsometric data is compared with electroreflectance results [7]. Ellipsometric measurements have provided excellent values of dielectric constant and refractive indexes of a large variety of bulk semiconductors [11].

The accurate information about critical point energies obtained by the methods described above have had a symbiotic relationship with band structure calculations in the physics of semiconductors. In the following subsections we discuss the application of differential optical techniques to the determination of critical points in the electronic transitions of Si/Ge microstructures. When interpreting experimental data we shall use simple concepts such as those of zone-folding or confinement of electronic states that can be derived from those of the bulk components. This method gives a good intuitive understanding of some results but is not applicable to all cases, so the reader is advised to read chapter 5 of this volume, where the electronic structure of these materials is described in great detail.

B. On Pseudo-direct Optical Transitions

It is expected that superlattices (SL) alternanting n-monolayers of Ge with m-monolayers of Si ($Ge_n Si_m$), should produce, through zone-folding, a direct band-gap material with appropriate choices of n, m and the amount of strain in each type of layer (see chapter 5 in this volume). The strain can be controlled by the choice of substrate (Si or Ge) and buffer layer on which the superlattice is grown (see chapter by J.C Bean in this volume). In these superlattices the conduction band edge is formed from bulk-Si $\Delta-$states, while the top of the valence band originates in bulk-Ge Γ-point states. The Δ-conduction band of bulk Si forms a degenerate sextuplet, one for each (100) equivalent direction. In the SL the multiplet splits into a doublet ($\Delta_\perp$) and a quadruplet ($\Delta_\parallel$), for the valleys perpendicular and parallel to the plane of the layers respectively. Choosing the SL-period appropriately, the $\Delta_\perp$ can be folded into the Brillouin Zone center. This results in a direct gap material if the two-fold $\Delta_\perp$ minima are lower in energy than the four-fold $\Delta_\parallel$ ones. This could be achieved by subjecting the Si-layers to a tensile strain. Hence, we should not expect to find direct gaps in SLs grown lattice matched on Si. Paradoxically, it was a report of a strong optical transition at very low photon energies in such a material that produced a flurry of activity on the subject. Room-temperature electroreflectance measurements in a $Ge_4 Si_4$ five-period SL exhibited a very strong line at $\backsim$ 0.76 eV, which was tentatively identified as direct transition between the valence band and the $\Delta_\perp$-folded conduction band. [12] The spectrum, shown in fig. 4(a), exhibits several other lines which can be attributed to direct transitions and in which zone-folding plays no role. The fact that the line at $\backsim$ 0.76 eV (labelled "1" in fig 4(a)) has an intensity which is comparable to those of these other lines was interpreted as a signature of a quasi-direct transition (i.e., a transition made direct through zone-folding). Although a tight binding band calculation by Brey and Tejedor [13] gave support to this interpretation, the majority of calculations predicted an indirect gap (i.e., they predicted that the lowest conduction-bands minima were produced by $\Delta_\parallel$ states) [14,15]. Even for a pseudo-direct transition, the calculated oscillator strength is much smaller than the observed

one. Subsequent measurements of photocurrent and electroreflectance in the same sample, interpreted with a first-principles band calculation, established the existence of two indirect absorption edges, at $\backsim$ 0.78 and 0.90 eV respectively, but not of a direct one [15]. The photocurrent measurements are shown in fig.4(b).The anomalous oscillator strength of these indirect transitions remained unexplained, although Hybertsen et al. [15] mention end effects (their SL is only five periods long) and interface roughness as probable causes. The other lines in the ER spectrum of fig.4(a) were discussed in more detail in a later paper by the same group [16] and their interpretation includes other transitions from the valence band to folded conduction band states whose intensity greatly exceeds that of the predictions of band calculations. These results shall be discussed in section II.D, in the context of higher-energy direct transitions in Ge_nSi_m SLs.

Next, electroreflectance measurements performed on two Ge_nSi_m ($n+m = 10$) SLs grown commensurately on Ge substrates are reported by Pearsall et al. [17]. These SLs should have pseudo-direct band gaps, produced by the folding of the $\Delta_\perp$ conduction band edge, since they satisfy both the periodicity and strain conditions previously explained. Their spectra show a rich pattern of strong structures at photon energies just above that of the direct E_0 peak of bulk Ge, which they attribute to pseudo-direct transitions. First principles band calculations show that such pseudo-direct gaps exist in this photon energy region, although the transitions associated with them should have negligible oscillator strength [18]. Hence, the existence of a pseudo-direct gap not necessarily explains the structure observed in the spectra of Pearsall et al. [17]. This assignment is even less firm when we take into account the actual structure of the samples used in the experiments. Besides the thick Ge buffer layer, each sample contains twenty repetitions of the basic 5-period Ge_nSi_m SL separated from one another by 25nm-thick Ge layers. These thicker Ge layers contribute to the total spectrum with their own E_0 transition and a strong pattern of Franz-Keldysh oscillations induced by the applied electric field [7,10]. These contributions fall in the same photon energy range as that of the pseudo-direct transitions from the Ge_nSi_m parts of the sample. In order to overcome the problem of the Franz-Keldysh oscillations Yin, Yan and Pollak [19] performed

a piezo-reflectance study on a series of Ge_nSi_m SLs which includes those previously studied by Pearsall et al [17]. Their piezo-reflectance results show that the spectral features that had been identified as due to pseudo-direct transitions from the SL parts of the samples are, instead, quantum-confined E_0 transitions originating in the 25nm Ge spacer layers. But the search for pseudo-direct transitions continues. Pearsall et al. recently reported measurements of differential transmission on these samples that seem to support the idea of anomalously strong optical absorption at the pseudo-direct band edge [20,21].

While the controversial results of the modulated reflectivity work were being actively discussed, new evidence from photoluminiscence (PL) work performed on Ge_nSi_m SLs was added to the debate. Zachai et al. [22] reported photoluminiscence experiments performed on a series of Ge_nSi_m SLs with different periods and states of strain. The strain variations were achieved by using either Si or Ge substrates and buffers of partially relaxed Si-Ge alloys. In all cases their SLs have many periods (total SL-thicknesses of $\backsim$ 200nm), so end-effects cannot be invoked here. On the other hand both the density of misfit dislocations and interface roughness should be larger here than in the shorter SLs used in the electrorefectance work (see chapter by J.C Bean in this volume). fig. 5 summarizes the results of Zachai et al. [22]. A very broad and inhomogeneously broadened peak at $\backsim$ 0.84 eV appears in a strain symmetrized sample with $n + m = 10$. This sample has the right period and strain to have a pseudo-direct gap. This peak is either absent or very weak in samples which do no meet this criteria (i.e., samples with indirect gaps). Hence, these authors identified the PL line as a direct recombination, at the BZ-center, from the bottom of the folded $\Delta_\perp$conduction band to the top of the Ge-like valence band. This interpretation was hotly disputed by Schmidt et al. on the basis of their comparison of the photon-energy position of the PL peak and the value of the pseudo-direct gap obtained in their ab-initio calculation for the SL used in the PL experiment [23]. Also, the calculated oscillator strength for this pseudo-direct recombination is orders of magnitude smaller than that which would be required to observe this strong emission. They suggest that the emission line is associated with defects (the samples in question are known to have dislocation densities between 10^8 and $10^{10} cm^{-2}$) and

point out that remarkably similar emission lines were observed by other authors in samples where the active region was composed of an homogeneously strained layer of Ge_xSi_{1-x} alloy [24]. In these samples the gap is definitely indirect and no zone-folding can be invoked. To counter this criticism, Meczingar et al. [25] studied the absorption (via photocurrent) and PL spectra of two $Ge_n Si_m$ superlattices with $n + m = 10$. These samples were grown in conditions that guaranteed a very low dislocation density. Figure 6 reproduces their PL and absorption spectra for a Ge_4Si_6 SL (upper curves) and a $Ge_{0.4}Si_{0.6}$ alloy grow under the same conditions. The onset of the SL absorption is shifted towards lower photon-energies, by $\backsim 100$ meV, in relation to that of the alloy. Comparison between the absorption and the PL features in the former sample supports the interpretation that the latter originates in a no-phonon recombination across the gap which produces the absorption edge (see sec. IV). Joining both results we conclude that the PL of the SL sample is due to a no-phonon recombination which takes place in the part of the sample containing the Ge_4Si_4 SL and not in the alloy buffer layer. This seems to support the interpretation of Zachai et al. [22]. However, this interpretation is not unique. First we notice that the similar PL feature observed by Nöel et al. [24] in Ge_xSi_{1-x} quantum wells are also due to a no-phonon recombination process across the alloy's **indirect** energy gap i.e., to explain this line no direct gap is necessary. Second, the buffer layer is not the only place in the sample which contains alloy layers. The results from Raman scattering experiments in Ge_nSi_m SLs show that alloy layers form spontaneously at the Ge/Si interface(see section III.E.3). So these superlattices contain a certain amount of Si-Ge alloy even when it has not been intentionally included in the sample. Hence, the PL peak could be equally well interpreted as due to recombination in the alloy regions of the sample located around the Si/Ge interfaces of the Ge_4Si_6 SL.

The discussion above shows that, although zone-folding does result in pseudo-direct gaps for samples of appropriate periods and strain, no clear evidence exists that the strong optical structures observed in reflectivity, absorption or PL spectra of some Ge_nSi_m superlattices are associated with transitions across this gap. This is made especially plain by the fact that these strong spectral features also appear in samples where the gap is clearly indirect.

Thus. zone folding does not appear to be the main reason behind these strong features in the optical spectra, but rather other components of the sample which appear unintentionally during growth might be responsible for them. This view is supported by recent theoretical calculations which show that if a disordered layer exists, extending only ± 1 monolayer (ML) about the Si/Ge interfaces of a 10-ML period superlattice, alloy scattering becomes the dominant mechanism for recombination [26].This point is thoroughly discussed in Chapter 5 of this volume, so we need not elaborate any further here. One additional remark is in order about the interpretation of the results from the type of optical experiments discussed so far. Most of the uncertainties when interpreting spectra arise from the failure to answer the following question: which part of the sample is responsible for the observed spectral feature? The optical spectra results from the response of the whole sample, which, aside from the actual Ge_nSi_m SL, includes buffer and spacer layers as well as thin layers of disordered material at the interfaces. In some cases the technique of Resonant Raman Scattering is able to give an experimental answer to this question (see discussion in section III.E). However, it is not always possible to perform such experiments. In these cases theoretical studies must be used to answer this question (see chapter 5).

C. Other Optical Transitions in Si/Ge_xSi_{1-x} and Ge/Ge_xSi_{1-x} Microstructures

The early optical work in Si/Ge microstructures was conducted on quantum wells (QWs) and superlattices obtained by alternating relatively thick (2.5 - 25 nm) layers of Si and Ge_xSi_{1-x} alloys grown lattice matched on Si (001) substrates [27]. In these structures the quantum wells are composed of a disordered, strained, material. In order to describe the electronic states of the SLs it is necessary first to understand those of the strained alloy. Experience shows that these can be described fairly well in the spirit of the virtual crystal approximation [28]. Within this framework we can attribute to the alloy a band structure which is a weighted average of those of Si and Ge and that responds to strain in very much the same manner as those of the constituent materials [29–32]. Figure 7 shows a schematic

representation of a biaxially compressed $Ge_{0.5}Si_{0.5}$ alloy derived using the approximations just described [33]. A comparison between figs 7 and 1 shows the similarities between the band structures of the alloy and those of the constituent materials. Figure 7 also shows the optical transitions responsible for the main features in the modulated reflectivity spectrum. These transitions are clearly seen in the ER-spectra of bulk, unstrained, alloys. The evolution of the transition energies as alloy composition changes is illustrated in fig.8 [34]. This figure shows that the optical transitions in the Ge_xSi_{1-x} alloy evolve continuously, and indeed linearly in most cases, from those of Si into those of Ge as x varies from 0 to 1. Disorder seems to affect optical spectra only by introducing extra broadening in the observed lines. This could be interpreted, within the virtual crystal approximation, as a disorder-induced relaxation of the conservation of crystal momentum in the optical transitions. Hence it is possible to think of the states of the quantum-well as resulting from confined alloy bulk states, in the same manner as if the material of the QW were pure Si or Ge [28].

These ideas, however, needed to be put to the experimental test. To the best of our knowledge, the first observation of optical transitions attributable to confined states in Si/Ge_xSi_{1-x} SLs were the resonant Raman scattering measurements of Cerdeira, Pinczuk and Bean [35]. The Raman spectrum of these materials is discussed in detail in section III. Here we merely remark that the intensity of a given Raman peak is enhanced when the incoming or scattered beams have a photon-energy which coincides with that of a direct electronic transition involving states confined within the same layer as that in which the vibration originating the peak is confined. Hence, plotting the intensity of a given Raman line as a function of the photon-energy of the incoming laser ($\hbar\omega_L$) one obtains a curve which has peaks whenever $\hbar\omega_L$ coincides with such a transition. These authors [35] report a resonant enhancement in the cross section of an alloy phonon, which can be attributed to vibrations of the Si-Ge bond (see section III.B), at photon energies in the range $\hbar\omega_L \backsim 2.0$ - 2.6 eV , in a series of Si/Ge_xSi_{1-x} SLs with a variety of QW-widths ,d, and alloy compositions (see fig.9), x. This signals the presence of an optical transition (or a family of closely spaced optical transitions) between states confined within the alloy QW. These transitions were

tentatively identified as the strain-split E_0 doublet of the alloy layers, modified by stress and confinement (see fig.7).

Encouraging as this first indication of quantum confinement in this type of materials were, the resonant Raman experiments did not provide accurate transition energies for the optical transitions involved. Indeed, even their identification as E_0-like transitions is not unequivocal, because of the proximity of E_1transitions of the alloy layers. More detailed information about optical transitions in these materials was later reported by Pearsall et al. [36]. These authors reported electroreflectance measurements in Si/Ge_xSi_{1-x} SLs in a wide photon-energy range (2.0 - 4.0 eV). A typical ER-spectrum is shown in fig.10, where the arrows indicate assignments of spectral features to transitions between electronic states in the SL derived from bulk-alloy electronic states modified by strain and confinement. These assignments are complicated by the fact that two multiplets overlap in energy: the $E_0(1)$ and $E_0(2)$ strain-split doublet and the E_1 and $E_1+\Delta_1$ of the bulk alloy (see fig.7). Also, the spectral lines for this strained and disordered QW-material are rather broad, as can be seen in fig.10. Even so, the assignments in this figures for the E_0 doublet are in good agreement with calculations made on the basis of the well-known behaviors of these gaps with strain, alloy composition and a simple Kronig-Penney-type model, with constant effective masses,to account for the effects of quantum confinement [37]. The quantum wells were constructed using band alignments at the Si/Ge interface proposed by Van de Walle and Martin [38], which involve very shallow wells for holes and deep QWs for electrons (as much a 1.8 eV for some of the samples of ref [36]). These deep QWs should produce a multiplet of transitions associated with each of the strain-split E_0 gaps. The width of the ER lines in the spectrum of fig. 10 does not allow to resolve the members of these multiplets produced by quantum confinement. For the E_1-multiplet confinement cannot be included in a straightforward way, so in was ignored by Pearsall et al. [36]. Even so, fairly good agreement is found between predictions made on this basis and optical structures in their ER spectra.

The pioneering work described above proved that optical spectra in these structures could be interpreted successfully on the basis of direct optical transitions in the bulk-QW

material, modified by the effects of strain and confinement. These effects were reasonably well described, for zone-center transitions, by elastic theory and very simple Kronig-Penney-type models respectively. In order to obtain more accurate information for comparison with theoretical models, it would be necessary to produce materials in which the E_0 and E_1multiplets were not overlapping. Also, a better quality QW-material would produce sharper spectral lines. This was accomplished by growing the structures commensurately on Ge substrates and alternating alloy with Ge layers, i.e.: $Ge/Ge_x\ Si_{1-x}$ quantum wells and superlattices. In these structures the QW-material is pure, unstrained, Ge while the strain and disorder appears only in the barrier (alloy) material. An additional advantage is that in bulk Ge the E_0 and E_1 transitions are well separated in energy ($\backsim$ 1.4 eV, as can be seen in table I), so the multiple transitions associated with the E_0 optical gaps in the QWs do not overlap in energy with the structures associated with the bulk E_1 gaps. Optical multiplets associated with the E_0 transitions of bulk-Ge were first observed by piezo-reflectance in the thick (29 -143 MLs) Ge QWs formed in the Ge-spacer layers separating thin Ge_nSi_m short-period SLs [19]. These results were already discussed in the previous subsection. The observed multiplets were described qualitatively by a Kronig-Penney type model using constant effective masses. However, predictions differ from actual peak positions by as much as 110 meV in some cases. These predictions can be made more accurate by including the effects of non parabolicities in the conduction band. These effects are non-negligible in cases such as these. where the confinement energy can be comparable to, or even larger than, the E_0 gap in the bulk material. The matter was later taken-up by Rodrigues et al., who reported photoreflectance (PR) measurements on two $Ge/Ge_{0.7}\ Si_{0.3}$ SLs with relatively thick($\sim$ 10nm), unstrained, Ge quantum wells [39]. A typical spectrum from one of these samples is shown in the upper curve of fig.11. For comparison, the PR spectrum of bulk Ge is shown in the lower curve of this figure. The multiplet associated with the bulk Ge E_0 transitions is clearly seen in the spectrum of the Ge-QW of fig.11. The lines associated with bulk-Ge E_1 transitions are also clearly seen, but they appear at much higher photon energies. We discuss first the SL spectral features associated with the E_0 gap, which are shown in

greater detail in fig.12. Eight lines (labelled A through H, in order of increasing photon-energy) are clearly identified in this multiplet. These lines were interpreted in terms of the predictions of a simple Kronig-Penney-type model, using the offset of the average valence bands ($\Delta E_{v,av}$) as an adjustable parameter. The results of these calculations are shown in this figure as solid (dashed) curves for parity-allowed transitions at the mini-zone center (edge), while experimental transition energies are represented by horizontal dotted lines. The figure on the left-hand side of the spectrum was calculated with constant effective masses, while that on the right-hand side was produced by energy-dependent masses calculated with the Kane model [39,40]. For constant masses the agreement is poor for all but the lowest photon-energy lines, regardless of the choice of band offset. In contrast, excellent agreement is obtained when non-parabolicities are included (fig.12(c)) for a value of the band offset of $\Delta E_{v,av} \backsimeq 0.14 \pm 0.03$,which agrees with that proposed by Van de Walle and Martin [38]. Table II compares experimental and calculated values for the transition energies. In these assignments not only the lines associated with heavy (h) or light hole (l) transitions are identified. but also the effects of miniband dispersion is brought into focus as the structures produced by singular points at the mini-zone center (Γ) and edge (Π) become progressively resolved when the transition index (n) increases.

The above discussion vindicates the use of simple models based on confinement in square wells for the optical structures associated with the E_0 gap. This is a non-trivial conclusion, since the conduction minima at Γ, in bulk Ge, is higher in energy than other conduction band states (see fig.1) and inter-valley mixing could occur (see chapter 5). The nagging question remains as to whether the same would hold for SLs with ultra-thin layers. We tackle this question in the following section. Before coming to that, let us examine the part of the spectrum of fig.11 associated with the E_1 and $E_1 + \Delta_1$ transitions. No multiplets are observed here. In fact the spectrum of the SL and that of bulk Ge are almost identical, except for a small shift in the lines of the former towards higher photon-energies, which increases as the width of the Ge-QW (L) decreases (52 meV for $d = 11.1nm$ and 72 meV for $d = 10.2nm$) [41]. This argues in favor of confinement effects, even for optical gaps such

as these that extend through a large portion of the BZ [1]. The actual confinement of the electronic states is confirmed by resonant Raman results, which shall be discussed in sec. III.E. However, it is far from obvious how this concept applies to electronic states which have such a large energy-width that they overlap with many other states in the BZ. This complex situation precludes the use of square-well models to treat this confinement. In fact, the very concept of confinement becomes dubious, especially for SLs with very thin layers. This discussion will be taken up in the next section, devoted to optical results in Ge_nSi_m SLs.

D. Other Optical Transitions in Ge_nSi_m Quantum Wells and Superlattices

In sec.II.B we discussed some aspects of the ER-spectra of ultra-thin Ge_nSi_m SLs ($n, m \lesssim 5$), namely the existence of low photon-energy spectral lines which had been attributed to pseudo direct transitions at the folded fundamental gap. A representative ER-spectrum from a Ge_4Si_4, from ref [15], is reproduced in fig.4(a). Besides the line assigned to this pseudo-direct transition, other strong ER-lines appear at higher photon-energies. These are assigned to direct transitions between electronic states originating in bulk-Ge states modified by the superlattice potential. A more complete study of ER in this type of materials was later reported by Pearsall et al. [33]. In this work the spectra of Ge_nSi_m SL´s (grown commensurately on Si substrates) with $n = m = 1, 2$ and 4 are discussed in detail. The spectrum of fig.4(a) is representative of those of these samples. The sample with $n = m = 4$ shows several lines that are attributed to E_0 or E_1transitions. Since the Ge layers are biaxially compressed two E_0 lines are expected, corresponding to transitions between the strain-split heavy and light hole valence bands and the confined state (only one for very thin layers) of the conduction band. The members of this doublet are called $E_0\,(1)$ and $E_0\,(2)$, in order of increasing energy. This doublet (at 2.20 and 2.38 eV respectively) is identified in the ER-spectra of Pearsall et al. Also present in their spectra are two doublets, one strong (at 2.60 and 2.82 eV) and one weak (at 3.04 and 3.22 eV), which are assigned to

E_1 and $E_1 + \Delta_1$, respectively, modified by the superlattice potential. The nature of these modification is not made clear by Pearsall et al. They also discuss the spectra for samples with $n = m = 1, 2$, assigning spectral lines with the assumption of perfect interfaces. In view of the fact that interface roughness extends at least one monolayer on each side of the interface, these assignments are not likely to be reliable.

Photoreflectance (PR) measurements by Dafesh et al. [42,43], performed on a strain-symmetrized 60-period $Ge_{32}Si_8$ SL, are shown in fig.13. The thick Ge-QW should produce a multiplet for each one of the two strain-split E_0 gaps, in a manner analogous to that of the upper curve in fig.11. Instead only two strong lines, associated with the $n = 1$ transitions of $E_0\,(1)$ and $E_0\,(2)$, respectively, appear in the spectra of fig.13 (lines B and C respectively). A series of weak structures (D through P) also appear in the spectra. They are identified as higher transitions of the E_0 multiplets, E_1 and $E_1 + \Delta_1$ transitions from the Ge layers or transitions in the thick, strained-relaxed, alloy buffer layer. The label A in fig.13 designates a photon-energy region where indirect transitions might appear. None are reported by the authors [42]. The assignments are made exclusively on the basis of the photon energy of a given line. It is not clear, for instance, why the line attributed to the E_1 transition is so weak, knowing that this transition is responsible for the strongest line of the optical spectrum of bulk Ge in this photon energy range (see fig.2). On the other hand, SLs with such thick Ge-layers may have poor interfaces (see chapter by J.C Bean in this volume), so it would not be surprising if these weaker lines are related to defects rather than to the interband transitions of a perfect structure. In any case, there are a good number of these lines in a photon energy range where different electronic transitions overlap, so a more detailed knowledge of the band structure of the SL would be required in order to make reliable assignments of optical structures.

The combination mentioned above, of detailed band calculations with a sensitive optical technique, is present in the work of Schmidt et al. [44]. These authors report ellipsometric measurements, both at room temperature and at $T = 10K$, performed on a Ge_4Si_6 strain-symmetrized SL. They compare the second derivative of $\varepsilon_2\,(\omega)$, obtained by numer-

ical differentiation of experimental data, with that generated by a linear-muffin-tin-orbital (LMTO) ab-initio calculation. In figs 14(a) and (b), respectively, we show the comparison between their experimental and theoretical optical spectra and their results for the band structure calculation. Each interband transitions indicated in fig.4(b) produces a peak in the theoretical optical spectra of fig4(a) (arrows). Comparison between the experimental and theoretical optical spectra is excellent, once the theoretical photon-energy is given a uniform 0.1 eV shift to account for a systematic artifact of the calculation [44].Also, note that experimental spectra can only be obtained after the sample has become opaque to the incoming light ($\hbar\omega \gtrsim 2.7ev$). At lower photon energies the optical spectra is dominated by interferences produced by multiple internal reflections. This is a feature that affects most optical measurements based on reflectivity to a larger or lesser degree. Several techniques have been developed to remove the effects of these interferences [41], but it is always an ultimate limiting factor to the accuracy of reflectivity-based measurements in multi-layer systems. Taking these limitations into account, we can summarize the main conclusions of this work as follows :

- The lowest direct energy gap occurs at the Γ-point ($\backsim 1.1eV$). This gap appears as a result of zone-folding (see section I.B), but gives no significant contribution to the optical spectra because of its negligible oscillator strength.

- Strong absorption starts at $\backsim 2.3eV$ and it is associated with transitions along the $\Gamma - N$ line in the mini Brillouin-zone. This is a multiplet which originates in bulk E_1 transitions, modified by the effects of the superlattice potential through zone-folding and confinement. They are named E_1^{α} ($\alpha = a, b, c$ and d).

- The first transition at the Γ-point of the mini-zone which gives a significant contribution to the optical spectrum occurs at 2.6eV and originates in bulk-Ge E_0 transitions, shifted to this high energy by the effects of quantum confinement.

- In addition to the bulk-like features discussed above, fig.14(a) shows a series of weak

peaks, labelled S_i $(i = 1 - 6)$. These are attributed to transitions from the bulk-like valence band to folded conduction band states.

Subsequent theoretical [18] and ellipsometric [45] work confirms these results and trace the evolution of these optical structures for different sample parameters.

The discussion above exemplifies the importance of having a reliable band calculation when interpreting the optical spectra of Ge_nSi_m SLs. In this spirit, subsequent ER-measurements [46] in a series of strain-symmetrized SLs were examined within the general scheme of optical transitions illustrated in fig.14(b). In fig.15 we display their ER-spectra, taken at T = 77K, for samples with different layer thicknesses. Each spectrum shows a large number of structures, which result from a variety of transitions with overlapping critical energies. The authors assumed that the number of critical points were those of the LMTO calculation for the $n = m = 5$ case [18] and fitted their experimental data with this number of standard ER-lineshapes[*eq.*(1)]. The continuous lines in fig.15 represent the best fit to the data (open circles). The individual lineshapes composing each fit are shown below each spectra and the arrows indexed A, B,..etc. are the critical energies obtained from these component lines. The upper arrows indicate the critical energy and assignment of the LMTO calculation for a Ge_5Si_5 SL [18]. Also indicated in fig.15 are the calculated positions of the strain-split E_0 doublet, calculated by a simple Kronig-Penney model with energy-dependent effective masses [39]. Table III summarizes the numerical results of these assignments for the samples with short periods $(n + m \leqq 10)$. Here we also list the onset of strong absorption (E_{abs}) in these samples, obtained from the exponentially decaying envelope of the interference oscillations that precedes it, in the manner explained in ref [46]. Extending the same analysis to samples with larger periods, the evolution of these optical transitions as a function of period-length can be studied. The main results can be summarized as follows:

- The spectra always contain a feature whose origin can be traced to confined bulk-Ge E_0 transitions. This feature is very sensitive to the thickness of the Ge layer and its position is well explained by simple Kronig-Penney type models . This is illustrated

in the inset of fig.16, where the experimental transition energies from ER-spectra (open circles) are plotted against the predictions of such a model (open diamonds and continuous line) and those of the LMTO calculation (full diamonds). For $n+m \gtrsim 10$, this transition defines the onset of strong absorption in these materials. For smaller periods, the E_0 transitions move up in energy and falls among the members of the E_1-multiplet (to be discussed next). In this case one of the members of this multiplet defines the onset of strong absorption.

- As we already discussed,the E_1-transitions of the bulk materials originate a multiplet as a result of the modifications which the superlattice potential imposes on them. The evolution of the members of the multiplet as the thickness of the Ge layer increases is shown in fig.16. This figure suggests that this multiplet is mainly composed of a Ge-like doublet (E_1^a and E_1^b) and a Si-like one (E_1^c and E_1^d), which evolve towards the E_1 and $E_1 + \Delta_1$ transitions of bulk Ge and Si respectively, as the Ge layers become thicker.

- The E_1^a-transition of thin-layered SLs ($n \leqq 6$) is responsible for the most intense line of the ER-spectrum and constitutes the onset of strong absorption in these SLs. As the Ge layer thickness increases this line evolves continuously towards the bulk-Ge E_1 transition. but it always occurs at a higher photon-energy than the latter. This is true even for very thick Ge layers, such as those of the Ge/Ge_xSi_{1-x} SLs discussed in the previous subsection. Although this might suggest confinement of a bulk-Ge state, this energy increase could also result from an admixture of Si-like states which diminishes progressively as the thickness of the Ge layer increases. With the data discussed so far it would not be possible to distinguish between these two alternatives.

The last point in the above discussion could be clarified by studying how the E_1 multiplet is generated as the number of Ge-quantum wells increases from a single QW to a full superlattice, for fixed thicknesses of the Si and Ge layers. In the case of admixture of Si and Ge wavefunctions we would expect a weak dependence of these structures on the

number of periods, since this admixture depends mostly on the relative thicknesses of the Si and Ge layers. On the other hand, confined states would develop into multiplets with the wave function of its members still mainly confined in one or the other layer. An experiment of this type was attempted by Rodrigues et al. [41], who report photoreflectance (PR) measurements on three samples containing one (1QW), two (2QW) and six (6QW) Ge quantum-wells. The samples were grown lattice matched on Si (001) substrates. The Ge QWs have a thickness of five monolayers. In the samples with multiple QWs these are separated by 5MLs of Si. Each structure is repeated between 10 and 25 times and each unit is separated from the next by a 30nm-thick Si spacer-layer. Low temperature (77K) PR and room temperature resonant Raman scattering (RRS) experiments were performed on these samples. Their PR-spectra is shown in fig.17(a), where open circles represent experimental data and the solid curve is a fit with the standard lineshapes of eq.(1). Each line composing a given fit is shown below the respective spectrum. We see a continuous evolution in the spectra of the NQW samples, from one line for N=1, to two for N=2 and four for N=6, respectively. If we identify the spectral line in the single-QW as E_1, then the spliting of this feature into two components for the double-QW (A and B in fig.17(a)) is analogous to the splitting of a given electronic state into a symmetric and an antisymmetric component by the double well, while the multiplet generated by a fully periodic superlattice would already appear for six QWs. This assignment coincides with that made by Freeouf et. al on the basis of ellipsometric and RRS experiments performed on thin ($\backsim 0.7nm$) Ge-layers buried in a Si matrix [47]. The evolution of this structure as the number of Ge QWs increases is illustrated in fig.17(b), where the data for the strain-symmetrized Ge_5Si_5 SL from ref [46] was included ($N = 150$). The arrows at the side of this inset indicate the E_1 and $E_1 + \Delta_1$ transitions of biaxially strained bulk-Ge and strain-free bulk-Si respectively. There is a remarkable agreement between the multiplet of the 6QW sample and that of the SL. This agreement is even more impressive when we consider that both samples have different strain profiles. In order to say something about the actual confinement of the electronic states involved in these transitions, we turn to the RRS results. The exact manner in which this

technique gives information about wavefunction confinement shall be described in sec.III.E. Here we just mention that the Raman cross section of a vibration, known to be localized in a given layer, is enhanced **only** when the incoming (or outgoing) beam is in resonance with an electronic transition among states localized in the **same** layer. In table IV we list the photon energy and assignments of the lines in the PR-spectra, as well as the degree of confinement of the electronic states derived from the resonant Raman experiments. These results support the idea of wavefunction confinement for the electronic states involved in the E_1 transitions.

The parts of the discussion in the last two sections that was centered around spectral features in Ge single and multiple quantum wells which could be attributed to either E_0 or E_1 transitions of the bulk materials can be summarized as follows:

- Multiplets associated with the E_0 transitions are clearly observed in QWs and SLs with relatively thick Ge layers ($\backsim 10nm$) and alloy barriers. As these layers become thinner, this rich multiplet structure becomes obscured. This happens both because narrower wells have fewer confined states and also because interface imperfection becomes more important in thinner wells, leading to broader spectral lines. Another complicating factor is that confinement shifts these peaks into the region of the stronger E_1-multiplets. However, in all cases the lines identifiable as E_0 transitions have a strong dependence on layer thickness which can be quantitatively explained with simple square-well models.

- In single Ge-QWs confinement of the Λ-line states of bulk Ge occurs. This is not obvious, since these states cover a wide range of energies which overlaps (although at different **k**-vectors) with states along the same line in the barrier material. In a superlattice, these lines split into two doublets which have wavefunctions mostly confined into the Ge (Si) layers for the doublet at lower (higher) photon energy. These doublets appear as a consequence of zone-folding and the manner in which this happens cannot be described by simple square-well models.

The results of this whole section were discussed within the framework of electronic calcu-

lations performed for microstructures with perfect interfaces. As we shall see inn sec.III.E, actual interfaces always have disordered layers that affect at least $\pm 1 ML$ around the Ge/Si interface, and frequently present larger-scale roughness in the form of terracing an island formations. This real interfaces might have a decisive influence on the optical spectra which might, in turn, lead us to revise the previous assignments. The subject of electronic states in imperfect structures, and their influence in their optical properties, is amply discussed in chapter 5 of this book.

III. RAMAN SCATTERING

A. General Considerations

Inelastic light scattering by phonons has been used for several decades to obtain information about the electronic and vibrational states of semiconductors. Among the numerous reviews on the subject, we cite two representative examples: that of Cardona for bulk semiconductors [48] and that of Jusserand and Cardona for semiconductor quantum-wells and superlattices [49]. In what follows we shall give a brief summary of the elementary concepts and equations that we shall use throughout this section to describe the applications of this technique to Ge/Si microstructures.

The scattering event consists of an incoming photon of well-defined energy ($\hbar\omega_L$) and momentum ($\hbar\mathbf{k}_L$) which is scattered inelastically into another photon ($\hbar\omega_S$, $\hbar\mathbf{k}_S$) by creating or annihilating a phonon of energy $\hbar\omega$ and crystal-momentum $\hbar\mathbf{q}$. Let us focus on the process of creation of a phonon (Stokes line). Energy and crystal-momentum conservation require that:

$$\hbar\omega_L = \hbar\omega_S + \hbar\omega \qquad ,(a) \tag{2}$$

$$\hbar\mathbf{k}_L = \hbar\mathbf{k}_S + \hbar\mathbf{q} \qquad .(b)$$

Experiments are usually performed with lasers emitting in the visible or near infrared parts of the spectrum so, normally: $\omega_L \backsimeq \omega_S \gg \omega$. In opaque semiconductors most experiments are performed in backscattering ($\mathbf{k}_L \backsimeq -\mathbf{k}_S$), which results in a phonon wavevector given by:

$$q = \frac{4\Pi\eta}{\lambda_L} \quad , \tag{3}$$

where η is the refractive index of the material and λ_L ($\backsim 500nm$) the incident laser wavelength (in vacuo). Phonon wavevectors are measured in terms of the length of the Brillouin zone (Π/L, for a superlattice of period L), so,for most cases of interest, q$\backsimeq$ 0. Because acoustical phonons in bulk materials, at these small wavevectors, have very small frequencies, scattering by these phonons (Brillouin Scattering) is not observable in normal Raman scattering experimental arrangements. Hence, first-order Raman scattering in bulk semiconductors probe only the q$\backsimeq$ 0 optical phonons. When dealing with superlattices with a periodicity L, it is often useful to define a reduced wavevector:

$$Q = \frac{q}{q_{max}} = \frac{4\eta L}{\lambda_L} \quad , \tag{4}$$

which is measured in terms of the BZ-length along the growth direction. By an appropriate selection of L and λ_L, it is possible to probe both the optic and acoustic branches at arbitrary points along this BZ-axis.

The incoming and scattered photons are closely correlated, both in polarization and in energy. The intensity of a Raman line, associated with the creation of a given phonon of the ω_j-branch is given by:

$$I_S \propto |\mathbf{e}_L.\mathbf{R}_j\mathbf{e}_S|^2 \quad , \tag{5}$$

where $\mathbf{e}_L$ ($\mathbf{e}_S$) is a unit vector in the direction of the polarization of the incoming (scattered) light and $\mathbf{R}_j$ is the Raman tensor (a tensor determined by the symmetries of the material and that of the j-th vibrational mode). For Si, Ge and their alloys the triply-degenerate $\mathbf{q}\backsimeq 0$ optical modes have Raman tensors given by:

$$\mathbf{R}_x=\begin{bmatrix}0&0&0\\0&0&d\\0&d&0\end{bmatrix} \quad , \quad \mathbf{R}_y=\begin{bmatrix}0&0&d\\0&0&0\\d&0&0\end{bmatrix} \quad , \quad \mathbf{R}_z=\begin{bmatrix}0&d&0\\d&0&0\\0&0&0\end{bmatrix} \quad . \tag{6}$$

In eq.(6) d is a constant and x, y and z define the direction of the vibrational eigenmode in terms of the cubic axes. Thus, for QWs and SLs grown along the (001) direction (z), the first and second tensors correspond to in-plane vibrations, while the last one corresponds to vibrations along the growth axis. Raman scattering configurations are usually specified in the notation: $x_1\,(x_2, x_3)\,x_4$, where the first (last) x_i designates the direction of the incoming (scattered) photon, while the first and second letters in the parentheses define the polarization of the incoming and scattered beams, respectively. Inspection of eq.(6) reveals that the combination of polarizations (xy) selects scattering events by phonons vibrating along the growth axis while in-plane phonons are visible in configurations (x, z) and (y, z).

In archetypal GaAs/AlAs SLs acoustical branches are very similar in both materials , while optical branches do not overlap in frequency. Here the dispersion relations for the SL-phonons can be visualized by folding the average bulk acoustic branches into the reduced Brillouin zone of the SL and confining the optical vibrations within each layer. This procedure is schematically shown in fig.18 for the longitudinal branches of a hypothetical A_2B_2 SL, made up of two zinc-blende or diamond-type bulk semiconductors A and B. The optical branches of an A_nB_m SL are virtually dispersionless and obey the confinement conditions:

$$\omega_\nu^{A(B)} = \omega_{A(B)}^{bulk}\,(q_\nu) \quad , \ (a) \qquad \text{with} \tag{7}$$
$$q_\nu^{n(m)} = \frac{4\Pi\nu}{[n\,(m)+\delta]} \qquad (\nu = 1, 2, ...) \quad (b) \quad .$$

In eq.(7) δ accounts for the fact that the atomic displacement, instead of vanishing at the last A or B atom of a given layer. has a small penetration into the adjacent layer. Notice that the confined optical mode vibrating along the growth axis (perpendicular to it) are always derived from the dispersion relation of the bulk LO-modes (TO-modes), irrespective

of the direction of propagation of the phonon. This happens because these vibrations are longitudinal or transverse in relation to the quantized **q**-vector defined in eq.(7*b*), which is more important in defining the T or L-character of the phonon than the small propagation wavevector. The first experimental demonstration of this, for GaAs/AlGaAs, was given by Zucker et al. SLs [50].

The acoustic modes of the A_nB_m SL are obtained by zone folding of the average bulk acoustic branches. The difference between both materials manifests itself at the minizone edge and center, where gaps appear when these folded branches cross (see fig.18). For a given laser wavelength, several peaks appear in the Raman spectrum at the points of the dispersion satisfying eq.(3). This is illustrated in fig.18(c) by a dashed vertical line at this q-value. Symmetry allowing, each intersection of this line with the dispersion relation of the SL (open circles) generates a peak in the Raman spectrum.

Various models can be used to calculate the lattice vibrations of the SL. The most general type consists of building a cubic super-cell (SC) containing several periods of the A_nB_m structure and building up the dynamical matrix of this super-cell by using force constants between the different types of atoms. This dynamical matrix is then diagonalized, yielding eigenvectors and eigenvalues which can then be placed in a minizone scheme such as that of fig.18. The force constants are chosen so as to reproduce the dispersion relations of the bulk material, when the atoms of the supercell are either all A or all B. These calculations yield accurate results, but can be very complex. An alternative for obtaining dispersion relations and eigenmodes for longitudinal vibrations, for SLs grown along the (001)-direction, is to treat each plane as an "atom" of mass m_A or m_B and use inter-planar force constants so as to reproduce the bulk dispersion relations along the growth axis. This linear-chain (LC) models give very good results and are easy to handle. These models are well described in ref. [49]. More details about them shall be given when discussing actual results for Ge/Si SLs.

The description given above of the vibrational modes of SLs is appropriate for systems in which the optic branches of one of the bulk constituents do not overlap with any of

the branches of the other. In the Ge/Si system this is not exactly the case. In fig.19 we reproduce the bulk dispersion relations of Si, Ge and of a $Ge_{0.5}Si_{0.5}$ alloy for longitudinal modes [51]. This figure shows that, although the Si-optic branch is truly isolated, that of Ge has a region of overlap with the longitudinal-acoustic branch of Si. Thus, it is not clear that the concept of confinement, exemplified in eq.(7), applies to all the optic modes of SLs made up of layers of Ge alternating with those of Si or Ge_xSi_{1-x}. We shall examine this question in more detail in the following subsections.

B. Raman Scattering in Bulk Ge_xSi_{1-x} Random Alloys.

Experimental results reported by several authors [52–56], show that the Raman spectrum of a random Ge_xSi_{1-x} alloy is composed of three main peaks, which, for $x \backsim 0.5$, appear at frequency shifts of $\backsim 290cm^{-1}$ $(Ge-Ge)$, $407cm^{-1}$ $(\mathrm{Si}-Ge)$ and $480cm^{-1}$ $(\mathrm{Si}-\mathrm{Si})$. Subsidiary, weaker, structures are seen between the last two main peaks. These spectra obey the same selection rules as those of bulk Si or Ge and the main peaks shift as a function of strain in a manner similar to the peaks of their bulk constituents. In fact, Cerdeira et. al used the shift of the Si–Ge peak to determine quantitatively the biaxial strain in alloy layers deposited by MBE on Si substrates [57]. A representative spectrum of a bulk, 50%, alloy is shown in the lower curve of fig. 20(a).

Several theoretical models have been used to describe the Raman spectrum of random Ge_xSi_{1-x} alloys. [56,58–60]. The most consistent descriptions of the spectra are given by supercell calculations [56,60]. Alonso and Winer use a 216-atom supercell ($a_0 = 1.62813nm$) of Si and randomly place Si or Ge atoms at the different sites with an abundancy ratio dictated by the alloy composition. Their force constants are derived from the Keating model [61]. Diagonalization of the dynamical matrix yields the eigenvalues and eigenvectors of the vibrational modes of this supercell. The latter are used, in conjunction with a bond-polarizability model [62], to generate the Raman spectra numerically. These spectra are compared by Alonso and Winer with experimental ones, obtained from thick $(1-5\mu m)$

alloy layers grown by liquid-phase-epitaxy (LPE) on Si (111) substrates. This comparison is illustrated in the two bottom curves of fig.20(a), taken from another publication of Alonso et al. [63]. The calculation gives a good reproduction of the three main Raman peaks, as well as of the subsidiary structures appearing between the Si-Ge and Ge-Ge peaks. Although these subsidiary structures were taken, by some authors [58], to be signatures of partial ordering in these alloys, Alonso and Winer show that, on the contrary, they are a signature of randomness. In fact, these structures arise from localized vibrations of the Si-Si bond when surrounded by Ge atoms, as the later calculations of de Gironcoli et al. prove conclusively. In the same way, the three main peaks arise from the vibrations of Ge-Ge, Si-Ge and Si-Si bonds [60].

C. Raman Scattering by Optic Modes in Ge_nSi_m QWs and SLs.

The discussion in section III.A would lead us to expect that the contribution of the optic modes to the Raman spectrum would be composed of lines around $300cm^{-1}$ ($500cm^{-1}$) originating in vibrations confined within the Ge (Si) layers with a possible extra peak between these two, due to vibrations localized around the Ge/Si interface. Such spectra were first reported by Menedez et al. [64] in Ge_4Si_4 SLs grown commensurately on Si (001) substrates. These authors observe thee peaks in their spectra at 313, 421 and $509cm^{-1}$, respectively. The first (last) peak is attributed to an optical vibration confined into the Ge(Si) layer with a downward shift, of $9cm^{-1}$ ($12cm^{-1}$) due to confinement [eq. (7)] and an upward shift of $17cm^{-1}$ due to the biaxial strain in the Ge layers. The middle peak, however, bears a remarkable similarity to the Si-Ge peak of a Ge_xSi_{1-x} random alloy. This led the authors to suspect that interdiffusion could produce a thin alloy layer ($\pm 1ML$) around the Ge/Si interface. Other authors [65,66] report similar results. These suggestions were put into firmer grounds by Alonso et al. [63], who measured and calculated the Raman spectra of several strain-symmetrized Ge_nSi_m superlattices. Their measurements were performed in backscattering with light propagating along the (001)-growth axis, so their spectra contain only

longitudinal vibrations. Figure 20(a) sows the experimental spectrum of a Ge_4Si_4 (curve E), and compares it with the spectrum simulated by a supercell model similar to those previously used for calculating the spectra of random alloys [56] (curve D). The eigenvibrations of the modes producing the three theoretically predicted lines are shown in part (b) of this figure. We see that the first (last) peak in curve D of fig.20(a) are produced by optic modes confined in the Ge (Si) layers.. The agreement between the calculated and experimental spectra for these lines is good. This is also true of the spectra of the other samples measured and calculated by Alonso et al. [63]. There is, however, a large disagreement between theory and experiment when it comes to the middle line of the Raman spectrum ($\backsim 410cm^{-1}$ in curve E). Theory predicts a mode at much lower frequency shifts ($\backsim 358cm^{-1}$), in which Si and Ge atoms vibrate in opposition across the interface [fig.20(b)]. The peak in the experimental spectrum coincides, both in shape and position, with that produced by the Si-Ge vibrations of a random alloy (curve A in the same figure), which seems to re-inforce the idea that a region of alloying exists around the interface.. To test this idea Alonso et al. [63] included disorder in the two layers at each side of the Si/Ge interface. This was done by exchanging Si and Ge atoms in these two layers to obtain an average $Ge_{0.5}Si_{0.5}$ composition. The resulting spectrum (obtained by averaging several calculations for different random configurations in the interfacial layers) is shown in curve C of fig.20(a). This calculated spectrum is in much better agreement with the experimental one (curve E) than that calculated for perfect interfaces (curve D). Thus, the idea that roughness at the atomic scale exists at the Ge/Si interface, in the form of disordered alloy layers spreading on both sides of it, was vindicated. This notion was later re-inforced by Schorer et al. [67], who showed that the alloy Raman peak increases pronouncedly its intensity when the interfaces are smeared by annealing.

The most complete proof of the issue discussed above was given by de Gironcoli et al., who compare thorough experimental Raman results with an accurate supercell calculation, which uses first-principles force constants [68]. The Raman microprobe technique is used to obtain spectra of both longitudinal (along the growth axis) and transverse modes (in-plane

vibrations), by performing backscattering experiments both from the sample surface and from one of its cleaved or polished edges. In the calculation, an alloy plane is included at each side of the Si/Ge interface. Their calculation is explained in great detail in a previous publication [69], where they also show that the exact composition of the alloy layers has little effect on the main results. Their results for 50% alloys are very similar to those already shown in fig.20(a). However, two notable differences must be pointed out:(i) the T-polarization is also obtained and, (ii) the contribution of the individual atomic layers to each feature in the Raman spectrum (local density of states) is calculated for a Ge_8Si_8 SL. The latter is shown in fig.21 for both longitudinal (left-hand side) and transverse (right-hand side) modes. The longitudinal Si-Ge mode is seen to be localized in almost one single interfacial alloy layer. In contrast, the TO-mode leaks into both the Ge and Si layers. This happens because in this case, the line is a superposition of an alloy mode with an interfacial mode which occurs for the TO-polarization in a SL with perfect interfaces. This mode for a perfect interface does not exist for the L-polarization. Therefore, the appearance of this line in the experimental spectra can be taken as a signature for the existence of atomic-scale roughness at the Ge/Si interface. Two additional pieces of information can be obtained from fig.20: (i) the Si mode, originating the Raman peak close to $500cm^{-1}$, is strictly confined within the Si-layers and, (ii) the Ge LO-modes are very nearly confined within the Ge layers, so the overlap of the bulk Ge optical and the Si acoustical modes for L-vibrations does not produce a significant leak of this mode into the Si layers (no such overlap exists for the T-polarization, so Ge TO-modes are strictly confined). In a subsequent publication by the same group [51] these points receive confirmation. Here they also study the Si-confined modes in detail in samples with several layer thicknesses and successfully "unfold" these modes according to eq.(7).

Similar results were reported by other authors, interpreted with a much simpler linear-chain model [70,71]. Alloying at the interfaces was introduced by substituting the masses of Si and Ge planes on both sides of the interface by weighted averages of both. Similar averages of the force constants were taken. thus creating an "alloy atom" (or plane) at each side of the interface. Although this procedure reproduces the results of the more complete

SC-model for the Si and Ge mode, the exact symmetries it presupposes makes it inadequate to represent disorder. Consequently it does not reproduce the Si-Ge Raman peak either in position or lineshape [71]. On the other hand, when its limitations are well understood, the LC-model can be a very useful tool for interpreting experimental spectra of features which are not induced by disorder. In particular, Araujo Silva et al. use it to prove confinement, according to eq.(7), in both the Si and the Ge optical vibrations [71]. More shall be said about this in section III.E.

D. Raman Scattering by Acoustical Phonons in Si/Ge Microstructures

As previously explained (sec. III.A), the acoustic branches of a superlattice can be obtained by folding the average bulk dispersion relation into the mini-Brillouin zone (fig.18). Quantitative results can be obtained by an elastic continuum model, originally developed by Ryotov to explain the propagation of sound waves in a layered medium [72]. For a two-component SL made up of alternating layers of A and B layers (of thicknesses d_A and d_B, respectively, and period $L = d_A + d_B$), the dispersion relation, $\omega(q)$, of these superlattice acoustic modes is given by [49]:

$$\cos(qL) = \cos\left(\frac{\omega d_A}{v_A}\right)\cos\left(\frac{\omega d_B}{v_B}\right) - \frac{\gamma^2+1}{2\gamma}\sin\left(\frac{\omega d_A}{v_B}\right)\sin\left(\frac{\omega d_B}{v_B}\right) \quad , \tag{8}$$

where $v_A(\rho_A)$ and $v_B(\rho_B)$ are the sound-velocities (densities) of the bulk materials and

$$\gamma = \frac{\rho_B v_B}{\rho_A v_A} \quad . \tag{9}$$

Raman scattering experiments using different laser wavelengths (λ_L) probe these branches at different q-values (see fig. 18 and eqs(3) and (4)). A large variety of Raman experiments were performed by different authors in Si/Ge_xSi_{1-x} SLs which allowed quantitative mapping of the folded acoustic branches [73–75]. These experiments were well explained by the model of eq(8). One of the most impressive results was the observation of unklapp processes [74], made possible by choosing λ_L and L in such a way as to obtain reduced wave vectors [eq. (4)] $Q > 1$.

The Ryotov model assumes an infinite number ($N \rightarrow \infty$) of superlattice periods and phonon wavelengths much larger than the thickness of the layers. The first condition is not always met in highly strained structures. In addition, the use of bulk sound velocities and densities in eq(9) only gives good results for relatively thick layers. In Ge_nSi_m SLs these quantities must be considered adjustable parameters in order to obtain good agreement between the predictions of eq.(8) and experiment [75,76]. Also, high-resolution Raman spectroscopy shows additional spectral features, appearing in the spectra of thick-layer Si/Ge_xSi_{1-x} SLs, which are not predicted by eq.(8) [76,77,79]. In order to explain these features, Dharma-wardana et al. resorted to a linear-chain model with first-principles interplanar force constants and up to fourth-neighbor interaction [79]. This model contains no adjustable parameters and translational invariance (i.e., $N \rightarrow \infty$) is not assumed. They simply diagonalize a dynamical matrix of dimensionality $N_{tot} = N_{subs} + N_{SL} + N_{cap}$, where N_{SL} is the total number of atomic planes of the superlattice and N_{subs} (N_{cap}) are the number of these planes in the substrate (capping layer). The authors compare the predictions of both the Ryotov and the LC models with their experimental results in the frequency-shift region $\omega \lesssim 50cm^{-1}$ for a $Si/Ge_{0.48}Si_{0.52}$ ($20.5nm/4.9nm$) SL with $N = 15$ repetitions, using several laser lines. This comparison is shown in fig.22(a), where the positions of the main peaks in the Raman spectrum (full circles) and the LC-model calculations (crosses) are plotted on the dispersion relation predicted by the Ryotov model (continuous lines). Both models reproduce well the experimental results for the main Raman peaks, but the latter uses several adjustable parameters while the former uses none. Most importantly, the Ryotov model predicts **only** these main Raman peaks, whereas the LC-model also predicts subsidiary structures which appear in the experimental spectra. This additional peaks result from the finite character of the sample. In fig.22(b) we reproduce the spectra generated by Dharma-wardana et al., with the LC-model, for samples containig different repetitions of its basic period (N). The spectrum evolves towards that of an infinite superlattice (coinciding with the Ryotov model) as N increases. The final folded modes are produced by the accumulation of a high density of states at the Ryotov positions with increasing N.

The lower curve ($N = 15$) corresponds to the sample used in their experiment. This curve shows, besides the main Ryotov peaks, fine structure which appears in the experimental spectra (not shown). Hence, the LC-model gives a better description of the spectra, while maintaining a relatively simple calculation scheme. Recently, a numerical variation of the elastic-continuum model has been proposed, which can account for finite size and capping layer effects by imposing appropriate boundary conditions [80]. Many subsidiary peaks, as well as structure appearing within the forbidden gaps of the dispersion relations, observed in the spectra of Si/Ge_xSi_{1-x} SLs, are explained with this model [81]. However, the model uses several adjustable parameters.

For ultra-thin Ge_nSi_m SLs the elastic continuum model is not adequate, both because of the thinness of the layers and also because they frequently contain a very small numbers of periods. Moreover, the Ge_nSi_m portions of the sample are nested within more complex structures containing buffer, spacer and capping layers. These structures contain Raman peaks in the low frequency side of the spectrum which are unrelated to the folded modes of the Ge_nSi_m SL. The LC-model is able to deal with this complexity, without loosing its simple calculational structure. This is illustrated in the examples reported by Locwood et al. and Araujo et al [82,83]. In the latter, high resolution Raman spectroscopy was used to study the low-frequency part of the spectrum ($\omega \lesssim 100cm^{-1}$) and ordinary Raman spectroscopy was used for the remaining parts of it. The samples, grown by MBE on Si (001) substrates, had a complicated structure , which can be described by: $[(Ge_n\,Si_m)_{N-1}Ge_n\,Si_M] \times p$. Here n, m and M are layer thicknesses in monolayers (ML) and N and p are the numbers of repetitions of a given unit. The samples used in the experiments had $n \backsimeq 5$, $m \backsimeq 5$ or 7, $M \backsimeq 200$ and $p \backsimeq 10 - 20$. Thus, they contained two periodicities: the smallest period $(n + m)$ is that of the Ge_nSi_m unit, while the largest $(D = N \times n + (N-1) \times m + M)$ is that of the unit in square brackets. The lower frequency part of the spectrum ($\omega \lesssim 100cm^{-1}$) contains peaks which arise from this larger period, the structure in the intermediate part of the spectrum ($100cm^{-1} \gtrsim \omega \lesssim 250cm^{-1}$) arises from the smaller periodicity and the high-frequency part of the spectrum originates in the confined optic modes. By applying the LC-model to these

structures Araujo et al. were able to determine in which parts of the sample the vibrational amplitude of a given mode is confined. They find that the vibrations originating the low-frequency part of the spectrum spread throughout the whole structure, while those giving rise to the intermediate-frequency part of the spectrum are concentrated within the Ge_nSi_m strings and are,in fact, the folded acoustic modes of an infinite Ge_nSi_m SL. Finally, for high frequencies optic modes dominate the spectrum. This part of the spectrum is totally insensitive to variations in N or M i.e., these complicated samples yield the same spectra, in the optical phonon region, as that of infinite Ge_nSi_m SLs already discussed in the previous subsection. In fig.23 we sow the calculated, (a), and experimental Raman spectra, (b), of these samples in the low frequency region. This part of the spectrum is very sensitive to variations in N or M, since both alter the greater period, D. The latter controls peak positions, as shown in fig.23(c), thus providing a good way to determine this structural parameter. In fig.24 the same is done for the intermediate-frequency part of the Raman spectrum. In fig.24(a) the calculations produce a Raman peak originating in the folded acoustic modes of the Ge_nSi_m SL. The position of this peak is insensitive to variations of both N or M , but its intensity depends strongly on the former. The same trend is observed in the experimental spectra [fig.24 (b)]. The shift in the lower curve ($N = 100$) is due to the fact that this is a strained symmetrized SL and, therefore, has a different strain profile than the other samples (commensurately grown on Si). The interesting aspect of fig.24 is that the folded acoustic mode is present in the spectrum, although weakly, even when the basic Ge_nSi_m unit appears only three times.

Raman scattering by folded acoustic modes was observed in strain-symmetrized Ge_nSi_m samples containing many periods [63,51]. A representative example of these results is shown in fig.25. The left hand side of this figure shows the dispersion relations for the longitudinal and transverse acoustic modes of a Ge_4Si_4 SL, Calculated with the SC-model [63]. The circles on four of these curves correspond to the modes observed in the Raman spectrum [fig.25 (b)]. The most prominent feature in this spectrum is the peak produced by the $\nu = \pm 1$ folded LA modes. Higher order folded LA-modes are observed in the other SLs [see fig.25(b)]. In

all cases simulated spectra are in good agreement with experimental ones. The asymmetry in the Raman peak of the lowest curve in fig.25(b) is produced by the appearance of the forbidden Raman peak originating in the B_{1u} mode. This peak is forbidden for $q \equiv 0$. The non-zero value of q in the actual experiment[eq. (3)] weakly induce the appearance of this peak [63].

E. Resonant Raman Scattering

1. Introduction

The subject of Resonant Raman scattering in semiconductors is exhaustively reviewed by Cardona [48], who discusses in depth its usefulness and the subtleties of the interpretation of the experimental results. The Raman cross section is also didactically explained in chapter 7 of the textbook by Yu and Cardona [1]. For a good understanding of the subject we refer the reader to these general references. Here we shall briefly sketch the aspects of this technique which are relevant to the analysis of the results reported for Si/Ge microstructures.

The Stokes Raman cross section results from an infinite sum of terms originating in processes which involve the virtual absorption of a photon ($\hbar\omega_L$), creating an electron-hole pair. the emission of a phonon ($\hbar\omega$) via electron-phonon interaction at the initial or final state of this transition, and a recombination of the resulting electron-hole pair with the emission of a photon ($\hbar\omega_S$) in such a way that the conservation laws of eq.(2) are satisfied. One of these processes is shown schematically in fig. 26(a) and its contribution to the Raman cross section is given by:

$$\sigma \propto \left| \sum_{c,c'} \frac{\langle v|H_{e-r}|c'\rangle\langle c'|H_{e-p}|c\rangle\langle c|H_{e-r}|v\rangle}{[\hbar\omega_L - (E_c - E_v)]\,[\hbar\omega_S - (E_{c'} - E_v)]} \quad + \quad ... \right|^2 . \tag{10}$$

In the above equation H_{e-r} and H_{e-p} are the Hamiltonians of the electron-radiation and electron-phonon interactions respectively, while E_c (E_v) is the energy of the electronic conduction (valence) band state. In the cases where the photon energy of either the incoming or outgoing beams coincide with that of an interband transition with a significant joint density

of states (i.e., one of the singular points in the optical spectra discussed in section II), one, or both, of the energy denominators of the above equation vanishes and the contribution from this particular term dominates the Raman cross section. This results in an enhancement in the intensity of the Raman peak. Thus, one might expect that plotting the intensity of the Raman peaks as a function of the photon energy of the incoming beam, spectra similar to those obtained by modulation spectroscopy should be obtained. Here the modulating agent is one of the vibrational modes of the material. Even if this naive interpretation were invariably true, the process of data gathering is cumbersome, as many individual Raman experiments must be performed for different laser wavelengths. Also, the data has to be normalized to correct for changes in alignment or laser intensity between these successive experiments, as well as to account for the fact that both the incoming and scattered beams are partially absorbed as they traverse the material [48]. Returning to eq.(10), we note that each matrix element in this equation represents a selection rule that must be obeyed if the scattering process is to have non-zero probability. In particular, the element $\langle c|H_{e-p}|c'\rangle$ corresponds to electron-phonon interaction involving the electronic states which mediate the scattering event. Hence, the electronic and vibrational states involved must have spacial overlap for this matrix element to be different from zero. This is of crucial importance in an A/B SL, where both the electronic and the vibrational states may be confined in either the A or B layers. In this case, a phonon localized in layer A cannot receive a contribution to its Raman cross section from optical transitions between states localized in layer B, and vice-versa. Hence, no resonance effect will be observed in the cross section for this phonon when $\hbar\omega_L$ is in resonance with such a transition. On the other hand, resonant enhancements will occur when both the electronic states and the phonon are localized in the same layer. In the same way, vibrational modes that extend through both layers will have enhanced cross sections for resonance with any electronic transition and an electronic transition between extended electronic states will provoke enhancement in all Raman lines. These facts were first demonstrated by Zucker et al. in resonant Raman scattering (RRS) experiments performed in GaAs/AlGaAs SLs [84]. This characteristic makes RRS a very useful com-

plementary technique to the forms of differential spectroscopy reviewed in sec.II. While the latter provide very accurate information about the energy of critical points, RRS furnishes information about the localization of the electronic states participating in a given optical transition.

One cautionary note must be made concerning the analogy between RRS and modulated spectroscopies: the photon-energy position of the maxima in The RRS cross section often differs significantly from those of the singular points in the joint density of states that originate them (and, consequently, from the position of the corresponding peaks in the optical spectra), even for scattering processes involving only two bands, as the one illustrated in fig.26(a) [48]. The exact origin of these discrepancies (which could be of as much as $50meV$) are not fully understood, but the Raman cross section depends on the exact nature of the electron-phonon interaction which, in turn, cannot be exactly formulated in most cases of interest. This discrepancy becomes serious when the phonon has a symmetry such that it can couple two bands which lie close in energy. The contribution from these three-band processes can lead to complex lineshapes with maxima and minima (resulting from interferences between two- and three-band terms) which bear no easy relationship to the energy position of the associated critical points. As an example of this, the Resonant Raman cross section of bulk Ge, in the region of the E_1 and $E_1 + \Delta_1$ critical points, is shown in fig.27, from the data of Cerdeira et al [85]. In this figure the full symbols represent experimental data, the dashed line is meant to guide the eye and the arrows represent the positions of these two critical points, as given by measurements of modulated reflectivity. The Raman cross section presents only one, very broad, peak at a photon energy more or less midways between the two ER-peaks. This happens because, in this case, the cross-section is dominated by three-band terms, resulting from the coupling that the phonon introduces between the closely-spaced valence bands of Ge along the Λ-axis of the BZ. The solid curve is a phenomenological estimate of this contribution. The good agreement shown in the figure was obtained by shifting this theoretical curve by 45 meV towards higher energy. The $q \backsimeq 0$ optical phonon of Ge also couples the strain-split valence bands at the zone-center, when

the strain has a symmetry axis along the (001) direction, as is the case of Ge layers grown lattice-matched on Si (001) substrates. In that case E_0 transitions could produce resonant Raman cross-sections very similar to those of fig.27.

The coupling described above results from the Γ_{15} symmetry of the zone-center phonon. A phonon of Γ_1 symmetry, for instance, would not produce this coupling. The cross section of this phonon would show two distinct peaks, one for each critical point. Such a phonon exists in the folded acoustic branches of a Ge/Si SLs or in the totally symmetric part of the two-phonon spectrum of bulk Ge. This is indeed seen in the Resonant cross section of the totally symmetric part of the 2TO(L) spectrum of bulk Ge [86]. But even here the peaks in the Raman cross section are shifted in relation to the positions of the E_1 and $E_1 + \Delta_1$ critical points.

The discussion above should warn us against assigning optical structure on the basis of the positions of peaks in the resonant Raman cross section alone. This is particularly true when several transitions fall in the same photon energy range. In this case the coupling introduced by the phonon between the states participating of these transitions can result in complicated resonant lineshapes with maxima and minima which bear no immediate relationship to the energy position of the individual critical points. On the other hand, RRS has the unique property of giving direct experimental information about the localization of the electronic states participating of a given optical transition (or group of transitions).

2. Resonant Raman scattering in Si/Ge quantum wells and superlattices

The first observation of RRS in this type of structures was made in Si/Ge_xSi_{1-x} SLs of relatively large periods [35]. These results, displayed in fig.9, were already discussed briefly in section II.C. This figure shows broad single peaks in the resonant cross sections, in the general photon energy region where the E_1 and $E_1 + \Delta_1$ critical points of the unstrained alloy should be. Moreover, the general shape of the resonant peaks is similar to that of the E_1 resonance in bulk Ge (fig.27). However, strain and confinement should produce another

doublet in this photon-energy region [$E_0(1)$ and $E_0(2)$], which would also be coupled by the phonon, giving rise to a similar peak in the Raman cross section. On the basis of the dependence of this peak with layer thickness, Cerdeira et al. attributed this resonance to the E_0-doublet [35]. This assignment proved to be controversial and similar structures in the resonant Raman cross section of related Si/Ge materials were attributed alternatively to either one or another of these two doublets [41,35,87–89,91].

In fig.28 we display RRS results for the LO and LA modes of several strain-symmetrized Ge_nSi_m SLs [87]. For the SLs with larger periods, two distinct peaks are observed in the Raman cross sections of these modes, at $\hbar\omega_L \backsim 2.3$ and $2.9eV$ respectively. The lower photon-energy peak is produced by electronic transitions between states confined in the Ge layers. This can be deduced from the fact that, at this photon energy, only the cross-sections of the Ge-optic mode (confined in the Ge layers) and that of the folded LA-mode (extending through the whole SL) show enhancements, while that of the optical mode confined in the Si layers does not. In contrast, at the higher photon energy all modes are enhanced i.e., this transition (or group of transitions) involve electronic states with non-vanishing components in both layers. As the layer thickness decreases both peaks show a tendency to merge. The first group of optical transitions could either be associated with states derived from the bulk Ge E_1 or E_0 doublets. Cerdeira et al. favor the first choice, without totally discarding the second [87].

More recently, Schorer et al. performed very careful RRS experiments, where both longitudinal and transverse modes could be studied by exploiting the micro-Raman technique in order to perform backscattering experiments from the cleaved or polished sample edges [88,89]. Their main results are summarized in fig.29, in which the resonant cross sections of the first Ge and Si confined modes are displayed together with that of the alloy-like Si-Ge mode. In all cases a strong resonance is observed in the cross section of the Ge-modes, which is absent in that of the Si-modes, in the photon energy range around $2.2eV$, signaling the presence of electronic transitions between states confined in the Ge layers. This resonance is more pronounced in the L-modes, involving light polarized in the plane of the layers, than

in the T-modes, involving light polarized perpendicular to the layers. These anisotropies are in agreement with the results of a dielectric function calculation based on a tight binding approach [90]. These authors calculate the dielectric constant for light polarized both in the layer planes, $\varepsilon_{\parallel}(\omega)$, and perpendicular to them, $\varepsilon_{\perp}(\omega)$, separating the contributions from Ge and Si bulk states to this response function. This decomposition is shown in fig.30, where it is clear that in $\varepsilon_{2\parallel}$ the Ge and Si contributions are well separated in energy while this separation is blurred for $\varepsilon_{2\perp}$. The most prominent contribution to the in-plane dielectric constant, in the photon-energy region being discussed, comes from the E_1states of bulk Ge. Thus, there is a striking analogy between the calculations of $\varepsilon_2(\omega)$ and the results of RRS for L- and T-modes. This analogy also favors the interpretation of the RRS results in terms of bulk-Ge E_1 transitions, even if in their first report Schorer et al were inclined to attribute this resonance to E_0-like states [88].

Finally, resonant Raman results, combined with those of modulation spectroscopy, performed on single and multiple Ge_5 QWs reinforce the notion that the most important contributions to the optical response functions in this photon–energy range originate in confined electronic states traceable to the bulk Ge E_1 transitions [41,91]. The origin of these discrepancies in the interpretation of RRS results lies in the fact that the position of the maxima in the broad features of the resonant Raman cross sections (produced by scattering processes involving two- and three-band terms) are insufficient for making an identification of the optical transitions involved in the resonance.

The above discussion was centered mainly on the resonant cross sections of optic modes. Schorer et al. [88] report in detail RRS results from several orders ($\nu = 1, 2, 3$ and 4) of folded LA-modes in a $Ge_{12}Si_{12}$ SL (see fig.31). Since these modes transform according to totally symmetric representations of the SL point-group, three-band terms should not contribute to their resonant cross-sections. Hence, two well-resolved peaks should be observed when the resonance is produced by a doublet. This effect is indeed seen in the cross section of the LA_1-modes displayed in fig.31 as full triangles, which shows two distinct, albeit broad, peaks at $\hbar\omega_L \backsim 2.1$ and $2.4eV$, respectively. The resonant cross sections higher-order TA_ν modes

show one main peak, followed by a shoulder, which shifts towards higher photon-energies as the folding index, ν, increases. Qualitatively this could be explained by assuming that the resonance is produced by a multiplet which results from confined electronic states with different confinement indexes, and that resonances are stronger when both confinement indexes (that of the phonon and that of the electronic states involved in the transition) are equal. In this case, higher order folded phonons resonate preferentially with higher confined electronic transition, thus explaining the energy shift of fig.31. This explanation, attractive as it sounds, has no theoretical underpinning, since both the nature of the electronic transition, as well as the details of the electron-phonon interaction are not known.

All the discussion above was centered on interpretations based on perfect superlattices. As we shall see in the following subsection, this technique is also useful in establishing the presence of certain types of interface roughness.

3. Detecting long-range interface roughness by resonant Raman scattering

In section III.C we discussed the role of Raman scattering in determining atomic scale roughness in the Si/Ge interfaces of Ge_nSi_m SLs, in the form of random-alloy layers, existing in a region of $\backsim \pm 1ML$ about each interface. There is another type of roughness (terracing) which has been observed at the interfaces of some SLs composed of III-V materials [92,93]. These terraces, having lateral dimensions of the order of 10nm or more, produce splittings in the luminescence line produced by exciton recombination at the direct gap of these materials. It would be difficult to use luminescence to detect such terraces in Si/Ge systems, due to their indirect gaps and the resulting complexity of the luminescence spectra (see section IV). However, resonant Raman measurements have recently provided evidence of terracing in Ge_nSi_m SLs [94]. The samples used in the experiments of Brafman et al. were already discussed in sections IIIC and D. They consists of N-Ge_5 quantum-wells separated from one another by $5MLs$ of Si. Each sample contains up to twenty repetitions of a basic unit (with thick Si-spacer layers between them) which has $N = 1, 2$ or 6 and are designated by

NQW. The Raman spectra of these samples are studied, both for L- and T-modes, using several discrete lines of argon- and krypton-ion lasers. In fig.32 we show their results for the longitudinal Ge-confined optic mode. The upper part of the figure [fig.32(a)], displays the off-resonance spectra of the three samples, while part (b) of the figure shows the same part of the spectrum of the sextuple QW taken with laser lines of different photon-energies. We see that in the off-resonance spectra, the position and lineshape of this mode is different for each sample. This is surprising, since this line originates in a mode entirely confined within the Ge layers (see sec.IIII.C) and, therefore, insensitive to the number of layers i.e., all three lines should be identical. Moreover, fig.32(b) shows that this line, **for the same sample**, changes in position and lineshape as the wavelength of the incoming laser is changed. This means that we are in the presence of a resonant effect. These changes occur because the observed line is a superposition of Raman lines produced by phonons confined in Ge quantum wells of different thicknesses. These QWs are produced by terraces within a given Ge layer. In order to produce the effect of fig.32(b), the lateral dimensions of these terraces must be at least of the same order as the radius of the exciton involved in the resonance i.e.: $d \gtrsim 10nm$. Thus, the laser beam ($D \gtrsim 1\mu m$) samples a large number of these terraces i.e.: a large number of QWs of different widths. Each one of these QWs contributes to the Raman spectrum with a line centered around a different frequency [eq.(7)], in such a way that wider wells contribute to the higher-frequency part of the composite line and vice versa. For low values of $\hbar\omega_L$, resonant conditions are met for the wider wells, increasing the intensity of the high frequency side of the composite Raman line, which causes an apparent shift towards higher energy. As the laser photon-energy increases narrower wells meet the resonance condition, causing the low frequency part of the composite line to increase its intensity, which produces the asymmetric broadening and shift of its maximum towards lower frequencies seen in fig.32(b). Why does this happen in the 6QW sample and not on the others? Because terracing becomes more pronounced as the number of quantum wells increases. This explains the differences observed in the off-resonance spectra of the different samples [fig.32(a)].

The above conclusions were put on a more quantitative basis by comparing the experimental spectra with those generated by a linear-chain model, in which terracing was simulated by superimposing the Raman lines of QWs with different widths [71]. In fig.33(a) we show the result of fitting the experimental Raman line, for a given laser line, of the 6QW sample with a simulation using terraces with three different Ge thicknesses (3, 4 and 5 MLs). By performing such a fit for each laser line, the resonant cross section of each terrace, $\alpha_n(\omega_L)$, is obtained. This is shown in fig.33(b), where the dots, squares and diamonds represent the Raman cross-sections of the phonons confined within the QWs of 3, 4 and 5 MLs respectively, and the curves (dashed, dotted and solid) are least-square fits to these points with Lorentzian lineshapes. The results are consistent with the previous analysis, since they predict optical transitions which decrease in photon energy and linewidth as the QW becomes wider. This is consistent with the confinement of the electronic states involved in the transition (higher transition energies for narrower wells) and with the fact that microroughness is more important in broadening the line as the well becomes narrower. Finally, the change in the transition energy is plotted (full circles) as a function of QW-width in the inset of fig.33(b) and compared with the predictions of an envelope-function calculation (solid line) for an E_0 optical transition (section II.D). The experimental confinement shifts are much smaller than those predicted by theory, which lends support to the E_1 (rather than E_0) assignment for the optical transitions responsible for this resonance.

The method outlined above was recently used to study the evolution of short and long range roughness in Ge_n single quantum-wells of different thicknesses ($n = 3, 4, 5$ and 6), separated by 70MLS of Si [95]. These authors find that alloying at the Si/Ge interface occurs always, regardless of the Ge layer thickness. For $n \lesssim 5$ the alloy layer has an average Ge molar fraction which grows steadily as n increases until it stabilizes at $x \backsim 0.5$ for $n \gtrsim 5$. This is probably due to Ge segregation occurring at low values of n , which results in terrace formation. This terracing is visible in the dependence of the confined Ge Raman line on the wavelength of the exciting laser for the samples with $n = 3$ and 4, but absent in the samples with $n = 5$ and 6.Thus, a transition from terracing to layers of uniform average thickness

seems to occur in these samples at some value between 4 and 5 MLs.

The above discussion shows yet another application of Raman scattering to the structural characterization of quantum-wells and superlattices.

F. Summary

The preceding discussion shows that, when the results of experiments are complemented by lattice dynamical calculations, Raman scattering can provide important information about vibrational and electronic states. It also gives quantitative estimates for several structural parameters (such as strain, period length, layer thicknesses etc.) as well as detecting short- and long-range interface roughness. While the best picture of what goes on in a given microstructure is always given by the rather complex supercell calculations, simpler models, like the linear-chain or the elastic continuum ones, are often sufficient to give an enlightening interpretation of the experimental data. Resonant Raman scattering has the unique property of giving direct experimental information about the localization of the electronic wavefunction at critical points in the Brillouin zone. This aspect makes RRS a supplementary technique to those discussed in section II. However, its limitations must be understood in order not to incur in misinterpretations. One of these limitations is that the peaks in the Raman cross sections not always coincide with the energy of the critical point that originates it. The mechanism by which the phonon interacts with the electronic states involved in the transition must be known before conclusions are drawn on the basis of the photon-energy position of peaks in the Raman cross section.

IV. PHOTOLUMINESCENCE

A. Introduction

In a photoluminescence (PL) experiment an electron-hole pair is created by the absorption of an incoming photon, the created electron and hole thermalize rapidly to energy

minima and recombine from there by emitting a photon of lower energy. Because the emission occurs after a multiple scattering process, there is usually no correlation between the polarizations of the incoming and emitted photons. The idealized process of PL by band-to-band recombination is shown schematically in fig.26(b), for a direct band gap semiconductor. This process bears a certain superficial resemblance to that of resonant Raman scattering, shown schematically in part (a) of this figure.In the latter, however, both the photon absorption and emission are virtual processes and no loss of correlation between them occurs. Also, in the Raman process the frequencies of the incoming and outgoing photons are related to one another through eq.(2), while in the PL process of fig.26(b) the outgoing photon has always the energy of the band gap, regardless of the energy of the incoming photon (as long as it is greater than the band gap). In an indirect band-gap semiconductor, such as Si and Ge, recombination must be assisted by large wavenumber phonons in order to conserve crystal momentum. Hence, the intensity of the emission lines in indirect gap semiconductors is always much smaller than those in direct gap ones. In real semiconductors, specially at low temperatures, the recombination energy may not coincide with the band-gap. First, electron-hole interaction (excitons) modifies this. Second, excitons can be localized by impurities and defects and recombine from there, producing a rather complex PL-spectrum. This complexity is increased by the fact that the intensity of a given PL line depends much more on the efficiency of the recombination channel than on the contribution of the recombination centers to the overall density of states. Thus, emission lines from electronic states with a very small density of states can, in certain cases, be the dominant features of the PL-spectrum..

A technique related to PL is that of photoluminescence excitation spectroscopy (PLE). Here, the spectrometer is set at the maximum of a given PL-line while the photon energy of the incoming radiation is varied in a continuous manner around the region of the absorption edge. Since the number of electron-hole pairs created at a given incident photon-energy $(\hbar\omega_L)$ is proportional to the number of absorbed photons, the intensity of the resulting PL line will be roughly proportional to the absorption coefficient, $\alpha(\omega_L)$. In microstructures

composed of direct band-gap semiconductors PLE spectra show very sharp structure related to transitions between quantum-confined levels associated with the direct band-gap [96]. For indirect band gap systems, such as the ones we are interested in, the PLE spectrum does not show peaks, but rather an absorption edge below which the response is zero and above which it increases monotonically [97].

In the following subsections we discuss the application of this techniques to bulk Ge_xSi_{1-x} alloys and to QWs and SLs obtained by alternating layers of Si, Ge or alloy with one another.

B. PL from Bulk Ge_xSi_{1-x} Alloys

Well-resolved free-exciton (FE) and bound-exciton (BE) PL has been observed in bulk Ge_xSi_{1-x} alloys by several groups [98–103], culminating in the comprehensive work of Weber and Alonso [104]. In fig.34 we display their low temperature ($4.2K$) PL-spectra of bulk alloys with different compositions. The spectra exhibit several lines assigned to recombination of excitons bound to shallow donors and acceptors. The lines are labelled X_i^j , where j indicates whether the recombination is phonon assisted or not (NP) and i specifies the nature of the phonon when it is. The phonons of the alloy are labelled as Ge-Ge , Si-Ge or Si-Si , according to the classification explained in section III.B. They also observe free exciton lines in the PL-spectra taken at higher temperatures. The most prominent feature of the spectra in fig.34 is the no-phonon recombination line (X^{NP}), which appears as a consequence of a disorder-induced process which does not conserve crystal momentum. The ratio of the intensities of the no-phonon line to that of the phonon-assisted ones scales approximately as the number of Si-Ge pairs in the alloy [104]:

$$\frac{I^{NP}}{I^{PA}} \backsim x(1-x) \quad , \tag{11}$$

and the relative intensities of the phonon-assisted lines are given by:

$$\frac{2I^{TO}_{Ge-Ge}}{I^{TO}_{\mathrm{Si}-Ge}} \backsim \frac{1-x}{x} \backsim \frac{I^{TO}_{\mathrm{Si}-Ge}}{2I^{TO}_{\mathrm{Si}-\mathrm{Si}}} \quad . \tag{12}$$

The full-width at half-maximum (FWHM) of the X^{NP} lines also depends on x, varying from 4 to 8 meV (in the best samples), as opposed to $\backsim$ 0.3 meV for the same line in bulk Si. Finally, the position of this line as a function of x allow Weber and Alonso to obtain an accurate expression for the dependence of the indirect energy gap as a function of Ge molar fraction and to determine the cross-over (from Δ to L) of the conduction-band edge at $x = 0.85$.

Another interesting feature is observed in the PL spectra of some lower-quality samples: a broad feature on the low-energy side of the X^{NP} line [104]. This line had been previously labelled as the "L-line" by other authors [101], who interpreted it as a bound-exciton recombination at an In-acceptor. This interpretation is revised by Weber and Alonso, who attribute this broad PL-line to recombination occurring in a dense electron-hole plasma gathering in potential wells formed by large compositional fluctuations (probably in the vicinity of dislocations or other defects). A similar line is observed in the PL-spectra of some MBE-grown Si/Ge_xSi_{1-x} QWs. We shall discuss this in the following subsection.

C. PL from Si/Ge_xSi_{1-x} Microstructures

First reports of PL measurements in MBE-grown Si/Ge_xSi_{1-x} structures show spectra which are significantly different from those of bulk alloys [24]. The low temperature spectra of these samples show a broad PL structure near the alloy band-gap, rather than the sharp phonon-resolved structures of fig.34. By comparing PL and PLE measurements for their samples, Noël et al. determined that the center of this broad PL structure lies slightly below the indirect absorption edge of the alloy and tracks this gap as x varies [24]. This is illustrated in fig.35, where the low temperature (4.2 K) PL-spectra of three samples with different compositions and layer thicknesses are displayed.

Observation of phonon-resolved near-band-edge PL from strained Si/Ge_xSi_{1-x} layers were later reported both in MBE-grown samples [105] and in samples grown by rapid-thermal-chemical deposition (RTCVD) [97]. The spectra of Sturm et al. [97] are dominated by no-

phonon recombination, attributed to the annihilation of excitons bound to shallow impurities at $T \backsimeq 2K$, and to free exciton recombination at higher temperatures. As in the bulk case, peaks due to phonon assisted recombinations are also observed. In fact, their spectra are almost identical to those of bulk alloys (fig.34), except for photon-energy shifts which can be quantitatively related to strain and quantum-confinement. They also perform PLE-measurements to determine the absorption edge of the alloy QWs and use the difference in position between this and the PL line to determine the binding energy of the excitons. Both these measurements and those of the decay times ($\backsim 0.4ps$) of the main PL peak at $2K$ are consistent with the assignment of this line (recombination of excitons bound to shallow impurities). These authors also use the relative intensities of the phonon-assisted lines [eqs. (11) and (12)] to draw conclusions as to the actual confinement of these excitons.. They determine that, when the width of the QW (d) is larger than the exciton radius ($a_{exc} \backsim 4nm$), the wavefunction is entirely contained within the alloy layer while, when $d \lesssim a_{exc}$, the exciton wave function penetrates into the Si-barrier region.

Similar results were reported later by other authors in samples grown by MBE or CVD [106–108]. The clearest demonstration of quantum confinement in these QWs was given by Xiao et al. [108], whose results we reproduce in fig.36. The left-hand side of this picture shows their PL spectra at $4K$ for QWs of different well-widths (d), while part (b) of this figure shows a plot of the position of the no-phonon PL-line for two different temperatures (full triangles and squares) compared to the predictions of an envelope-function-type model (solid lines) which includes the effects of strain and confinement in the valence band states of the alloy and assumes negligible confinement for the conduction band electrons [38,109]). The excellent agreement between theory and experiment confirms the assignment of this PL-line.

The discussion above shows that two distinct types of behavior are seen in the PL spectra of Si/Ge_xSi_{1-x} QWs and SLs: well resolved luminescence of the same type observed in bulk alloys (fig,.36) and a broad PL-line, also associated with the indirect band-gap of the alloy-layer(fig.35). The broad PL-line seems to be present only in some (but not all) of the samples

grown by MBE [107,110–115], but not in those grown by CVD [97,116,117]. Several authors tried to correlate the appearance of this line with growth parameters such as layer-thickness, Ge-molar fraction, number of repetitions of the QWs and growth temperature. This gave a rather confusing picture, where contradictions abound. Rowell et.al. give a good review of these attempts [118]. The main findings about the appearance of this broad PL-feature can be summarized as follows (we discuss low-temperature PL measurements, $T \lesssim 4K$, unless otherwise specified):

- The maximum of this broad ($\sim 80meV$ FWHM) PL peak lies at lower energy than the NP-line in the sharp, phonon -resolved, spectrum, but it tracks the indirect gap of the alloy (always $\backsim 10meV$ below) as alloy composition or QW-widths change. This sows that this feature is also related to a no-phonon emission process across the fundamental gap [24].

- Terashima et al. [110] studied the evolution of the PL-spectrum of QWs grown by MBE at low growth temperature ($T_G \simeq 400\ ^0C$) as a function of annealing temperature. Initially their samples exhibit the broad PL-feature we have been discussing. Upon annealing in a N_2 atmosphere at temperatures $T_A \backsim 600-700\ ^0C$, this line increases its intensity by factors between 5 and 10. Annealing at higher temperatures ($T_A = 800\ ^0C$) transforms the PL-spectrum into a sharp phonon-resolved one similar to those observed in bulk alloys or in CVD-grown QWs (although greatly reducing the overall PL-intensity). The NP-line of this new spectrum lies at slightly higher photon-energies than that of the maximum of the broad PL-line.

- Spitzer et al. [111] report PL measurements in samples of different alloy compositions grown by MBE at low temperatures ($T_G = 325 - 450\ ^0C$). The thicknesses of these coherently-strained Ge_xSi_{1-x} layers (up to 500nm) greatly exceeded their equilibrium values (see chapter by R. Hull in this volume). While some as-grown samples present the broad PL line, others exhibit sharp phonon-resolved spectra. No correlation was found between layer thickness and the type of PL-presented by the as-grown samples.

The broad PL-line disappears upon annealing at $T_A \gtrsim 600^0$, when strain-relaxation sets in. After annealing both types of samples show narrow phonon-resolved PL-spectra.

- Noël et. al [112] and Rowell et al. [118] present some results that conflict with those of the previous item. They grew, by MBE, Si/Ge_xSi_{1-x} MQWs designed to be metastable at the growth temperature ($T_G = 600^0C$) . Their samples had three different QW-thicknesses ($d = 2.7, 5.2$ and 6.8 nm, respectively) and two different molar fractions ($x = 0.15$ for the first two and $x = 0.19$ for the last one). Their results are displayed in fig.37, which shows a steady increase of the broad PL-line over the phonon-resolved PL as the QW-thickness and Ge molar fraction increase. Observation of images by transmission electron (TEM) and Normansky phase-contrast microscopies suggest that the broad PL-feature is associated with the formation of platelets within the alloy layer, having lateral dimensions of $l \lesssim 1.5nm$ and a few MLs in thickness, oriented with their normal along the growth direction. These platelets seem to grow in number (up to $\backsim 7 \times 10^8 cm^{-2}$) as x or d increase and are envisaged as Ge-rich regions within the alloy layers. Because they constitute regions of lower energy-gap, excitons would drift towards these platelets and recombine there. This explains the lower photon-energy of the broad PL-line when compared with the NP-recombination from the regions of average alloy composition. The width of the PL feature is explained in terms of the wide size-distribution of these platelets, with their accompanying different confinement shifts. This interpretation is reinforced by their time-resolved PL measurements, which show that the decay time of the phonon-resolved PL is about 100 times faster than that of the broad PL feature. Notice that this explanation is very similar to the one given by Weber and Alonso [104] for the "L-peak" of bad quality bulk-alloy samples (sec. IV.B). The transition from sharp to broad PL as x or d increase is explained by Rowell et al. in terms of a strain energy model which predicts the existence of a "transition thickness" (d_c), which decreases as x increases. For $d \gtrsim d_c$, excess strain energy is relieved by the formation of platelets. This explains the fact that in samples

with many QWs the platelets seem to appear only in the outermost QWs. This was established by Rowell et. al by using selective etching in a MQW sample which exhibited broad PL before treatment. As successive QWs were etched away, the PL evolved towards sharp phonon-resolved luminescence. The mechanism proposed by these authors also explains the change-over from broad to sharp PL upon annealing [118].

- An alternative interpretation of the broad PL-feature is offered by Glaser et al. [113], on the basis of experiments which combine PL with optically detected magnetic resonance. They associate it with donor-acceptor pair recombination, which would explain the lower peak position as well as the larger width of this peak. The latter would result from the variations in the binding energy of the donor-acceptor pair depending on their position within the alloy-QW.

- Another piece of this puzzle is provided by Wachter et.al, who grew Si/Ge_xSi_{1-x} ($x \backsim 0.19 - 0.24$) QWs of different widths ($d \backsim 2 - 30nm$) by MBE using different growth temperatures ($T_G \backsim 350 - 600^0C$). Only sharp phonon-resolved PL was observed by these authors in as-grown samples, which seems to indicate that the formation of the type of defects that lead to the broad PL-line depends on how the MBE machine is run, rather than being a predictable characteristic of MBE-growth.

- In an attempt to clarify the relationship between the method of growth and the appearance of broad-band PL, Sturm et al. performed a series of experiments on RTCVD-grown Si/Ge_xSi_{1-x} QWs subjected to ion implantation and posterior thermal annealing [119]. Their results for one of their samples ($x = 0.20$ and $d = 6nm$) are displayed in fig.38. The top-most curve shows the low temperature (2K) spectrum of the as-grown sample, showing the sharp phonon-resolved spectra characteristic of CVD samples. This spectrum is preserved when a piece of this sample is annealed ($T_A = 600^0C$), as shown in fig.38(c). The luminescence disappears when the as-grown

sample is subjected to ion implantation with Si^{29+} ions at dosages between 10^{10} and 10^{12} cm^{-2} [fig.38(b)]. Annealing of the ion-implanted sample at 600^0C brings back the luminescence, but in the form of the broad-band PL which was thought to be characteristic of MBE-grown samples [figs.38 (d)-(f)]. Finally, annealing another piece of the ion-implanted sample at a higher temperature recovers the sharp phonon-resolved PL of the as-grown sample, although with weaker intensity [fig. 38(g)]. It is also to be noted that the broad-band PL is **not** observed in similarly treated Si-substrates or Si layers deposited on Si substrates i.e., this PL is definitely associated with the Ge_xSi_{1-x} layers. The properties of the broad PL in this CVD samples are identical to those previously observed in some of the MBE-grown samples. This is illustrated in fig.39 ,where the spectra of as grown and treated samples are displayed together for different sample parameters. The broad PL band follows the sharp PL, remaining always at slightly lower photon-energy. The appearance of broad-band PL in samples with very small implant doses, equivalent to a concentration of unwanted impurities of only $\backsim 10^{15}cm^{-3}$, rules out the mechanism of donor-acceptor pairs previously discussed [113].

The different, and often contradictory, results outlined above can be summarized as follows: broad-band PL is associated to no-phonon recombination across the indirect band gap of the alloy layer. This type of PL appears in samples containing a relatively high density of point defects or defect clusters. The formation of platelets, richer in Ge than the average alloy composition, could be associated with these point defects. The broad PL-line would result from the superposition of emission from platelets of different sizes. It is not clear why these defects appear in some of the MBE-growths, but it seems unlikely that there is a mechanism inherent to the growth process itself that would result automatically in the formation of these defects or defect clusters.

D. PL from Ultra-thin Ge_nSi_m QWs and SLs

The first observations of PL in Ge_nSi_m SLs reported a broad emission line, which was attributed to recombination from the folded pseudo-direct gap [22,25]. These results were already discussed in sec.II.A and are displayed in figs.5 and 6. These spectra bear an uncanny resemblance to the broad-band PL ones from Si/Ge_xSi_{1-x} structures shown in fig.35. In view of the discussion in the preceding sections of this chapter, it is probable that the PL features of the Ge_nSi_m SLs are greatly influenced by recombination in alloy layers inevitably present at the Si/Ge interfaces of these samples, regardless of whether they were grown strain-symmetrized on a partially relaxed Ge_xSi_{1-x} buffer layer or directly on Si. Since these interfacial alloy forms spontaneously as a result of interdiffusion, it must be inhomogeneous both in strain profile and composition, resulting in the type of defects that are seen to produce broad-band PL in the Si/Ge_xSi_{1-x} structures. This would explain the lineshape and intensity of the observed PL-line.

The more recent work of Sunamura et al. on Ge_nSi_m QWs focuses on using low temperature PL spectra to diagnose Ge segregation at the Si/Ge interface [120]. Their samples were grown on Si (001) substrates, at 700^0C, by gas-source molecular beam epitaxy and consisted in Ge_n QWs embedded between thick Si layers. Samples were grown with different average thicknesses of the Ge layers ($n \sim 1-12 MLs$). They studied the PL spectra of these samples at 22K. For small values of n they observe sharp phonon-resolved luminescence, which they attribute to recombination in the Ge QWs. The peak of the no-phonon line shifts towards lower energy as n increases. This is attributed to the diminishing of the confinement shift with increasing n. At $n \sim 4$ an abrupt change occurs.. The now familiar broad PL appears and gains in intensity with increasing n, while the sharp PL gradually fades away. Beyond this point peak positions in both the broad and sharp PL lines remain insensitive to further changes in n. Sunamura et al. interpret this as a transition between $2D$ and $3D$ growth occurring at $n \sim 4$. The sharp PL lines would originate in $2D$ regions while the broad PL is attributed to recombination in $3D$ islands created by Ge segregation for larger values of n.

The number of these islands would increase as n increases at the expense of the $2D$ regions, while the average size of both regions would remain constant. This would explain both the increasing (decreasing) intensity of the broad (sharp) PL line as n increases beyond $4MLs$ and the fact that PL lines do not suffer any further shifts in their peak position. Their analysis does not include the formation of alloy interfacial layers, such as those observed in similar (MBE-grown) samples by Narvaez et al. (see sec.III.E.3) [95]. The latter observe smoother 2D layers for $n = 5$ and 6 than for lower values of n. The difference in these result may be a consequence of the different growth method. On the other hand, in view of the discussion of sec.IV.B, it is also possible that the alloy layers are present in the samples of Sunamura et al. and that the PL-lines they observe in their samples are strongly influenced by those layers. This is in line with the theoretical results of Turton and Jaros (see chapter 5 in this volume), which predict that alloy scattering is the predominant mechanism for recombination in these materials [26]. In this case, the results of Sunamura et al. and those of Narvaez et al. might be brought into closer accord, since the composition of this alloy layer seems to vary with n in the MBE samples of the latter [95]. For low QW-thicknesses the interfacial alloy layers of the MBE samples have a low average Ge molar fraction. Because of this they should not be very strained or have a large density of defects. As n increases the molar fraction does so too, stabilizing at $x \sim 0.5$ for $n \sim 6$. This change in alloy composition and strain of the alloy layer could be partly responsible for the evolution of the PL spectra as a function of n reported on the gas source samples. On the other hand it is also possible that the two different growth methods produce a different evolution of the Ge/Si interface as the Ge coverage increases. Further experimental and theoretical work is needed in order to clarify this issue.

The discussion in this section shows that, in good quality Si/Ge_xSi_{1-x} structures, well-resolved near band-edge PL is observed. The PL spectra from these samples is similar to those of bulk alloys when appropriately modified by strain and confinement. Defects, whether spontaneously arising during growth or deliberately induced by posterior treatment, produce a broad PL line also associated to the alloy ban-gap. In fact, this line is rather

ubiquitous, since it appears in bulk alloys as well as in Ge_nSi_m SLs and QWs. Hence, care must be taken when interpreting PL data from these thin-layer systems in order not to attribute to SL effects (such as zone-folding) features that may arise from the inevitable roughness of the Si/Ge interface.

V. CONCLUDING REMARKS

In this chapter we have reviewed the optical properties of Si/Ge QWs and SLs. We have seen that the techniques based on absorption or reflection of light produced spectra with peaks at critical points in the joined density of states for interband transitions. Many experimental results can be explained in terms of the electronic band structure of the constituent materials, suitably modified by the effects of strain and confinement. For samples with relatively thick layers these effects can be calculated using elastic theory for strain and simple Kronig-Penney type models for confinement. As the layers become thinner (on the monolayer scale), more complex band calculations are needed in order to interpret optical spectra. One common feature of all these spectroscopies is that, since the dieclectric constant depends on the joint density of states, they are less sensitive to interface quality or end effects than those of other forms of spectroscopy such as Raman or PL. Because of this, calculations based on perfect interfaces often give a good description of the major spectral features. On the other hand, PL spectra are very sensitive to interface effects (see section IV). Here, model calculations for real interfaces are needed to give a correct interpretation of the spectra This is discussed in detail in chapter 5 of this volume. The Raman spectrum is also sensitive to interface effects. Fortunately these effects can be simulated using relatively simple models. This makes it possible to use Raman scattering as a tool to characterize interface roughness

Finally, some of the above results may be applicable to the rapidly developing field of Ge or Si quantum dots (QDs). For example, optical absorption spectra of Ge nanocrystals embedded in an Al_2O_3 matrix [121] are well described by the calculation, based on per-

fect crystallites, of Wang and Zunger [122]. On the other hand, the Raman spectra of Si nanocrystals in porous Si is strongly dependent the boundary conditions at the interface between them and the matrix in which they are embedded , as the analysis based on a linear-chain model of Ribeiro et al. shows [123]. While it is beyond the scope of this chapter to present a discussion of the results obtained in this rapidly expanding field, it is safe to assume that a combination of optical spectra and model calculations will be decisive in unveiling the optical properties of this new generation of Si/Ge microstructures.

REFERENCES

[1] P.Y. Yu and M.Cardona in "Fundamentals of Semiconductors," Chapters 6 and 7.Springer, Berlin,1995.

[2] H. Haug and S.W. Koch in "Quantum Theory of Optical and Electronic Properties of Semiconductors." World Scientific,Singapore1990.

[3] M.L. Cohen and J.R. Chelinkowsky in "Electronic Structure and Optical Properties of Solids," Springer solid State Science Vol. 75. Springer. Berlin 1989.

[4] F. Bassani in "Electronic States and Optical Transitions in Solids," Pergamon, London 1975.

[5] M. Cardona in "Modulation Spectroscopy," Solid State Physics (F. Seitz and D. Turnbull eds.)Supl.11, Academic Press, New York 1969.

[6] D.E. Aspnes, *Surf. Sci.* B **10**. 4228 (1973).

[7] D.E. Aspnes in "Handbook on Semiconductors," (T.S. Moss ed.),p.109. North Holland. Amsterdam 1980.

[8] F.H. Pollak, *Superlattices and Microstructures* **6**, 203 (1989) and *ibid* **10**, 333 (1991).

[9] F.H. Pollak and H. Shen, *Mater. Sci. Eng.* R **10**, 275 - 374 (1993).

[10] F. Cerdeira. *Brazilian J. of Phys.* **23**, 3 (1993).

[11] D.E. Aspnes and A.A. Studna. *Phys. Rev.* **27**, 985 (1983).

[12] T.P. Pearsall, J. Bevk, L.C. Feldman, J.M. Bonar, J.P. Mannaerts and A. Ourmazd, *Phys. Rev. Letters* **58,** 729 (1987).

[13] L. Brey and C. Tejedor, *Phys. Rev. Letters* **59**, 1022 (1987).

[14] K.B. Wong, M. Jaros, I. Morrison and J.P. Hagon, *Phys. Rev. Letters* **60,** 221 (1988), and references therein.

[15] M.S. Hybertsen, M. Schlüter, R. People, S.A. Jackson, D.V. Lang, T.P. Pearsall, J.C. Bean, J.M. Vandenberg and J. Bevk, *Phys. Rev.*B **37**, 1095 (1988).

[16] T.P. Pearsall, J. Bevk, J.C. Bean, J. Bonar and J.P. Mannaerts,*Phys. Rev.*B **39**, 3741 (1989).

[17] T.P. Pearsall, J.M. Vandenberg, R. Hull and J.M. Bonar, *Phys. Rev. Letters* **63**, 2104 (1989).

[18] U. Schmidt, N.E. Christensen, M. Alouani and M. Cardona,*Phys. Rev.*B **43**, 14597 (1991).

[19] Y. Yin. D. Yan and F.H. Pollak.*Phys. Rev.*B **44**, 5955 (1991).

[20] T.P. Pearsall, *Appl. Phys. Letters* **60**, 1712 (1992).

[21] T.P. Pearsall, H. Polatglou, H. Prestig and E. Kasper in "Proceedings of the 22nd International Conference on the Physics of Semiconductors", (D.J. Lockwood editor), p. 715. World Scientific, Singapore 1995.

[22] R. Zachai, K. Eberl, G. Abstreiter and H. Kibbel, *Phys. Rev. Letters* **64**, 1055 (1990).

[23] U. Schmidt, N.E. Christensen and M. Cardona. *Phys. Rev. Letters* **65**, 2610 (1990).

[24] J.-P. Noël, N.L. Rowell, D.C. Houghton and D.D. Perovic, *Appl. Phys. Letters* **57**, 1037 (1990).

[25] U. Meczingar, G. Abstreiter, J. Olajos, H. Grimmeis, H. Kibbel, H. Prestig and E. Kasper, *Phys. Rev.*B **47**, 4099 (1993).

[26] R. Turton and M. Jaros, *Appl. Phys. Letters* **69**, 2891 (1996).

[27] J.C. Bean, T.T. Sheng, A.T. Fiory, S. Nakamura and J. K. Robinson, *J. Vac. Sci. Technol.* A **2**, 436 (1984).

[28] G. Therodorou, P.C. Kelires and C. Tserbak, *Phys. Rev.*B **50**, 18355 (1994).

[29] G. Abstreiter, H. Brugger, T. Wolf, H. Jorke and H.J. Herzog, *Phys. Rev. Letters* **54**, 2441 (1985).

[30] Ch. Zeller and G. Abstreiter, Z. *Phys.* B **64**, 137 (1986).

[31] R. People, *Phys. Rev.*B **32**, 1405 (1985).

[32] D.V. Lang, R. People, J.C. Bean and M. Sergent, *Appl. Phys. Letters* **47**, 1333 (1985).

[33] T.P. Pearsall, J. Bevk, J.C. Bean, J. Bonar, J.P. Manaerts and A. Ormazd. *Phys. Rev.*B **39**, 3741 (1989).

[34] J.S. Kline, F.H. Pollak and M. Cardona, *Helv. Phys. Acta* **41**, 968 (1968).

[35] F. Cerdeira, A. Pinczuk and J.C. Bean. *Phys. Rev.*B **31**, 1202 (1985).

[36] T.P. Pearsall, F.H. Pollak, J.C. Bean and R. Hull, *Phys. Rev.*B **33**, 6821 (1986).

[37] G. Bastard, *Phys. Rev.*B **24**, 5693 (1981).

[38] C.G. Van de Walle and R.M. Martin, *Phys. Rev.*B **34**, 5621 (1986).

[39] P.A.M. Rodrigues, F. Cerdeira and J.C. Bean, *Phys. Rev.*B **46**, 15263 (1992).

[40] E.O. Kane in "Semiconductors and Semimetals" (K. Williardson and A.C. Beer editors) voll, p.75. Academic Press, New York 1966.

[41] P.A.M. Rodrigues,M.A. Araujo Silva, F. Cerdeira and J.C. Bean, *Phys. Rev.*B **48**, 1804 (1993).

[42] P.A. Dafesh, V. Arbet and K.L Wang, *Appl. Phys. Letters* **56**, 1498 (1990).

[43] P.A. Dafesh and K.L Wang, *Phys. Rev.*B **45**, 1712 (1992).

[44] U. Schmidt, F. Lukes, N.E. Christensen, M. Alouani and M. Cardona, *Phys. Rev. Letters* **65**, 1933 (1990).

[45] U. Schmidt,J. Humlicek, F. Lukes, M. Cardona, H. Prestig, H. Kibbel, E. Kasper, K.

Eberl, W. Wegscheider and G. Abstreiter, *Phys. Rev.*B **45**, 6793 (1992).

[46] P.A.M. Rodrigues, F. Cerdeira, M. Cardona, E. Kasper and H. Kibbel, *Solid State Commun.* **86**, 637 (1993).

[47] J.L. Freeouf, J.C. Tsang, F.K. LeGoues and S.S. Iyer, *Phys. Rev. Letters* **64**, 315 (1990).

[48] M .Cardona in" Light Scattering in Solids II ", Topics in Applied Physics vol.50, p.19. Springer, Heidelberg 1982.

[49] B.Jusserand and M.Cardona in "Light Scattering in Solids V", Topics in Applied Physics (M. Cardona and G. Güntherodt editors) Vol. 66,p.49. Springer, Heidelberg (1989).

[50] J.E. Zucker, A. Pinczuk, D.S. Chemla, A. Gossard and W. Wiegman, *Phys. Rev. Letters* **53**, 1280 (1984).

[51] R. Schorer, G. Abstreiter, S. de Gironcoli, E. Molinari, H. Kibbel and H. Prestig, *Phys. Rev.*B **49**, 5406 (1994).

[52] D.W. Feldman, M. Ashkin and J.H. Parker, *Phys. Rev. Letters* **17**, 1209 (1966).

[53] M.A. Renucci, J.B. Renucci and M. Cardona in "Proceedings of the Conference on Light Scattering in Solids" (M. Balkanski editor) p.326. Flammarion, Paris 1971.

[54] W.J. Brya, *Solid State Commun.* **12**, 253 (1973).

[55] J.S Lannin, *Phys. Rev.*B **16**, 1510 (1977).

[56] M.I. Alonso and K. Winer, *Phys. Rev.*B **39**, 10056 (1989).

[57] F. Cerdeira, A. Pinczuk, J.C. Bean, B. Batlogg and B. Wilson, *Appl. Phys. Letters* **45**, 1138 (1984).

[58] D.J. Lockwood, K. Rajan, E.W. fenton, J.-M. Baribeau and M.W. Denhoff, *Solid State*

Commun. **61**, 465 (1987).

[59] S. Wilke, J. Mašek and V. Velicky, *Phys. Rev.*B **41**, 3769 (1990).

[60] S. de Gironcoli and S. Baroni, *Phys. Rev. Letters* **69**, 1959 (1992).

[61] P.N. Keating, *Phys. Rev.* **145**, 637 (1966).

[62] R. Alben, D. Wearie, J.E. Smith Jr and M.H. Brodsky, *Phys. Rev.*B **11**, 2271 (1975).

[63] M.I. Alonso, F. Cerdeira, D. Niles, M. Cardona, E. Kasper and H. Kibbel, J. *Appl. Phys.* **66**, 5645 (1989).

[64] J. Menendez, A. Pinczuk, J. Bevk and J.P. Mannaerts, *J. Vac. Sci. Technol.* B **6,** 1306 (1988).

[65] E. Friess, H. Brugger, K. Eberl, G. Krötz and G. Abstreiter, *Solid State Commun.* **69**, 899 (1989).

[66] H. Brugger, E. Friess, G. Abstreiter. E. Kasper and H. Kibbel, *Semic. Sci. Technol.*, **3**, 1166 (1988).

[67] R. Schorer, E. Friess, K. Eberl and G. Abstreiter, *Phys. Rev.*B **44**, 1772 (1991).

[68] S. de Gironcoli, E. Molinari, R. Schorer and G. Abstreiter, *Phys. Rev.*B **48**, 8959 (1993).

[69] S. de Gironcoli, *Phys. Rev.*B **46**, 2412 (1992).

[70] M.W. Dahrma-wardana, G. Aers, D.J. Lockwood, and J.-M. Baribeau, *Phys. Rev.*B **41**, 5319 (1990).

[71] M.A. Araujo Silva, E. Ribeiro, P.A. Schulz, F. Cerdeira and J.C. Bean, *Phys. Rev.*B **53**,15871(1196).

[72] S.M. Ryotov, *Akoust. Zh.* **2**, 71 (1956) [*Soviet Phys. Acoust.* **2**,68 (1956)].

[73] H. Brugger, H. Reiner, G. Abstreiter, H. Jorke, H.J. Herzog and E. Kasper, *Superlattices and Microstructures* **2**, 451 (1986).

[74] M.C.W. Dahrma-wardana, D.J. Lockwood, J.-M. Baribeau and D.C. Houghton, *Phys. Rev.*B **34**, 3034 (1986).

[75] P.X. Zhang, D.J. Lockwood, H.J. Labbé and J.-M. Baribeau, *Phys. Rev.*B **46**, 9881 (1992).

[76] P.X. Zhang, D.J. Lockwood,and J.-M. Baribeau, *Can. J. Phys.* **70**, 843 (1992).

[77] D.J. Lockwood, *Surface Sci.* **267**, 438 (1992).

[78] P.X. Zhang, D.J. Lockwood and J.-M. Baribeau, *Appl. Phys. Letters*, **62**, 267 (1993).

[79] M.W.C. Dahrma-wardana, P.X. Zhang and D.J. Lockwood, *Phys. Rev.*B **48**, 11960 (1993).

[80] O. Pilla, V. Lemos and M. Montagna, *Phys. Rev.*B **50**, 11845 (1994).

[81] V. Lemos, O. Pilla, M. Montagna and C.F. de Souza, *Superlattices and Microstructures* **17**, 51 (1995).

[82] D.J. Lockwood, M.W. Dharma-Wardana, G. C. Aers and J.-M Baribeau, *Appl. Phys. Letters*, **52**, 2040 (1988).

[83] M.A. Araujo Silva, E. Ribeiro, P.A. Schulz, F. Cerdeira and J.C. Bean, *J. Raman. Spectrosc.* **27**, 257 (1996).

[84] J.E. Zucker, A. pinczuk, D. Chemla, A. Gossard and W. Wiegman, *Phys. Rev.*B **29**, 7065 (1984).

[85] F. Cerdeira, W. Dreybrodt and M. Cardona, *Solid State Commun* **10,** 591 (1972).

[86] M.A. Renucci, J.B. Renucci, R. Zehyer and M. Cardona, *Phys. Rev.*B **10**, 4309 (1974).

[87] F. Cerdeira, M.I. Alonso, D. Niles, M. Garriga, M. Cardona, E. Kasper and H. Kibbel,

*Phys. Rev.*B **40**, 1361 (1989).

[88] R. Schorer, G. Abstreiter, H. Kibbel and H. Prestig ,*Phys. Rev.*B **50**, 18211 (1994).

[89] R. Schorer, G. Abstreiter, H. Kibbel, H. Prestig, C. Tserbak and G. Theodorou, *Solid State Commun* **93,** 1025 (1995).

[90] C. Tserbak, H.M. Polatoglou and G. Theodorou, *Phys. Rev.*B **44**, 3467 (1991).

[91] M.A. Araujo Silva, P.A.M. rodrigues, F. Cerdeira and J.C. Bean in "Proceedings of the 22nd International Conference on the Physics of Semiconductors", (D.J. Lockwood editor), p.1540. World Scientific, Singapore 1995.

[92] D. Gammon, B.V. Shanabrook and D. Katzer, *Phys. Rev. Letters* **67**, 1547 (1991).

[93] M.J.S.P. Brasil, R.E. Nahory, M.C. Tamargo and S.A. Schwartz, *Appl. Phys. Letters* **63**. 2688 (1993).

[94] O. Brafman, M.A. Araujo Silva, F. Cerdeira, R. Manor and J.C. Bean. *Phys. Rev.*B **51**. 17800 (1995).

[95] G. Narvaez. I.L. Torriani, F. Cerdeira and J.C. Bean. *Brazilian Journal of Physics* (Dezember 1997).

[96] H.W. Liu, R. Ferreira, G. Bastard, C. Deldane, J. Palmier, B. Etienne, *Appl. Phys. Letters*, **54**, 2082 (1989).

[97] J.C. Sturm, H. Manoharan, L.C. Lenchyshyn, M.L.W. Thewalt, N.L. Rowell, J.-P. Noël and D.C. Houghton, *Phys. Rev. Letters* **66**, 1362 (1991).

[98] C. Benoit à la Guillame, M. Voos and Y. Petroff, *Phys. Rev.*B **10**, 4995 (1974).

[99] E.F. Gross, S.S. Sokolov and A.N. Titkov, *Fiz. Tverd. Tela* **14**, 2004 (1972) [*Sov. Phys. Solid State.* **14**, 1732(1973)].

[100] R. Rentz and I.S. Shlimak, *Fiz. Tekh. Poloprovodn* **13**, 719 (1978)

[*Sov. Phys. Semicond.* **12**, 416(1978)].

[101] G.S. Mitchard and T.C. McGill, *Phys. Rev.*B **25**, 5351 (1982).

[102] A.S. Lyutovich, K.L. Lyutovich, V.P. Popov and L.N. Safronov, *Phys. Status Solidi* B **129**, 313(1985).

[103] J.P. Dismukes, L. Ekstrum and R.P. Paff, *J. Phys. Chem.* **68**, 3201 (1964).

[104] J. Weber and M.I. Alonso, *Phys. Rev.*B **40**, 5683 (1989).

[105] K. Terashima, M. Tajima and T. Tatsumi, *Appl. Phys. Letters*, **57**, 1925 (1990).

[106] S. Fukatsu, H. Yoshida, A. Fujiwara, Y. Takahashi and Y. Shiraki, *Appl. Phys. Letters*, **61**, 804 (1992).

[107] N. Usami, S. Fukatsu, and Y. Shiraki, *Appl. Phys. Letters*, **61**, 1706 (1992).

[108] X. Xiao, C.W. Liu, J.C. Sturm, L.C. Lenchyshyn, M.L. Tewalt, R.B. Gregory and P. Fejes, *Appl. Phys. Letters*, **60**,2135 (1992).

[109] R. People and J.C. Bean, *Appl. Phys. Letters*, **48**, 538 (1986).

[110] K. Terashima, M. Tajima, N. Ikarashi, T. Niino and T. Tatsumi, *Jap. J. od Appl. Phys.* **30**, 3601 (1991).

[111] J.Spitzer, K. Thonke, R. Sauer, H. Kibbel, H.-J. Herzog and E. Kasper, *Appl. Phys. Letters* **60**, 1729(1992).

[112] J.-P. Noël, N.L. Rowell, D.C. Houghton, A. Wang and D.D. Perovic, *Appl. Phys. Letters* **61**, 690(1992).

[113] E.R. Glaser, T.A. Kennedy, D.J. Godbey, P.E. Thompson, K.L. Wang and C.H. Chern, *Phys. Rev.*B **47**, 1305(1993).

[114] M. Wachter, F. Schäffler, H.-J. Herzog, T. Thonke and R. Sauer, *Appl. Phys. Letters* **63**, 376(1993).

[115] J. Brunner, U. Menczingar, M. Gail, E. Friess and G. Abstreiter, *Thin Solid Films* **222**, 27 (1992).

[116] D. Dutrarte, G. Brémond, A. Soufi and T. Benyatton, *Phys. Rev.*B **44**, 11525 (1991).

[117] D.J. Robbins, L.T. Canaham, S.J. Barnett, A.D. Pitt and D. Calcott, J. *Appl. Phys.* **71**, 1407 (1992).

[118] N.L. Rowell, J.-P. Noël, D.C. Houghton, A. Wang, L.C. Lechyshyn, M.L.W. Thewalt and D.D. Perovic, J. *Appl. Phys.* **74**, 2790 (1993).

[119] J.C. Sturm, A. St. Amour, Y. Lacroix and M.L.W. Thewalt, *Appl. Phys. Letters* **64**, 2291(1994).

[120] H. Sunamura, N. Usami and Y. Shiraki, *Appl. Phys. Letters* **66**, 3024(1995).

[121] P. Tognini, L.C. Andreani, M. Geddo, A. Stella, P. Cheyssac, R. Kofman and A. Migliory, *Phys. Rev.*B **53**, 6992(1996).

[122] L.W. Wang and A. Zunger, *Phys. Rev. Letters* **73**, 1039 (1994).

[123] E. Ribeiro, F. Cerdeira and O. Teschke. *Solid State Commun* **101,** 327 (1997).

VI.

VII. FIGURES

Fig.1. The band structure of bulk Ge showing the various direct transitions responsible for the structure in the optical spectra of fig.2. Adapted form ref. [1].

Fig.2. (a)Reflectivity (adapted from ref [1])and (b)electroreflectance (adapted from ref. [33].)of bulk Ge. Peaks in the latter are identified according to the optical transitions of fig.1.

Fig.3.(a) Real and imaginary parts of the dielectric constant for bulk Ge, (b) $E^{-2}\frac{d^3}{dE^3}\left[E^2\varepsilon\right]$,from numerical differentiation of the curve in (a), and (c) $\Delta\varepsilon$ from ER measurements. Adapted from ref [7].

Fig.4. (a) ER spectrum of a Ge_4Si_4 SL with fitted critical point energies indicated by arrows. (b) Photocurrent signal for the same sample; the dashed lines show a fit with two indirect absorption edges and background. Adapted from ref. [15].

Fig.5. PL spectra of several strain-symmetrized Ge_nSi_m SLs with $n+m=5,10$ and 20. All have a common thickness ratio $m/n=1.5$ and biaxial strain $\epsilon_{\|}\backsimeq 1.4\%$ $\left(\epsilon_{\|}\backsimeq 2.7\%\right)$ in the Si (Ge) layers. The Ge_2Si_3 structure has a more alloy-like behavior. Adapted from ref. [22].

Fig.6. PL and absorption spectra of a Ge_4Si_6 SL and a $Ge_{0.4}Si_{0.6}$ alloy. Adapted from ref. [25].

Fig.7. Schematic band structure of a $Ge_{0.5}Si_{0.5}$ alloy subjected to uniaxial tension along the (001) axis. The two nonequivlent $\langle 100\rangle$ directions are shown. Adapted from ref [33].

Fig.8. Evolution of the critical point energies for the main optical transitions in Ge_xSi_{1-x} alloys. From the ER-spectra of ref. [34].

Fig.9. Raman cross section of the Si-Ge peak vs $\hbar\omega_L$ for Si/Ge_xSi_{1-x} SLs with different QW-withs and molar compositions. From ref. [35].

Fig.10. ER spectrum (77K) of a 7.5nm $Si/Ge_{0.45}Si_{0.55}$ QW. From ref. [36].

Fig.11. PR spectrum of a $Ge/Ge_{0.3}Si_{0.7}$ SL (upper curve) and ER spectrum of bulk Ge (lower curve).

Fig.12. Comparison between the calculated transition energies of the E_0 multiplet of a $(11.1/3.2nm)$ $Ge/Ge_{0.3}Si_{0.7}$ SL and those obtained from the PR spectrum (see ref. [39]). (a) Full (dashed) lines show calculations, using constant effective masses, for zone-center (zone -edge) transitions as a function of the valence band discontinuity. (c) Same as (b) but using energy dependent effective masses. (b) Experimental PR spectrum; arrows indicate critical points; horizontal dashed lines are the prolongation of these arrows into the (a) and (b) panels..

Fig.13. PR spectrum of a strain-symmetrized $Ge_{32}Si_8$ SL . The inset shows an enlargement of the structures labelled B and C. The label A designates a photon energy region where indirect transitions could, in principle, be observed. Adapted from ref. [42].

Fig.14. Experimental and theoretical results for a strain-symmetrized Ge_4Si_6 SL.(a) Second derivative of the imaginary part of the dielectric constant [numerically obtained from ellipsometric measurements of $\varepsilon_2(\omega)$]:lowest (second lowest) curve for T=10K (300K). Theoretical simulations with different broadenings: top and second-from top curves.(b) Calculated electronic structure. Adapted from ref. [44].

Fig.15. ER spectra of strain-symmetrized Ge_nSi_m SLs. Circles represent experimental data while the continuous line is the best fit with eq.(1) for seven critical points (A through G). Component lines of a given fit are shown below each spectrum. Critical energies from the LMTO calculation of ref. [44], for n=m=5, are shown with arrows on top. Also indicated are the E_0 critical points given by an envelope-function calculation. From ref. [46].

Fig.16. Dependence of the critical point energies of the E_1 multiplet with the thickness of the Ge layer. Arrows indicate positions of critical points for strained bulk Si and Ge. The continuous lines are guides for the eye. The inset shows the evolution of the E_0 critical point. From ref. [46].

Fig.17. (a) ER spectra (open circles) of the NQW-samples fitted with the lineshapes of eq.(1),continuous line. Arrows indicate critical-point energies from the fit.(b). Critical energies for E_1-like transitions vs N. Arrows indicate the value for this critical points in strained (unstrained) Ge (Si). From ref. [41].

Fig.18. Schematic representation of the folding of the phonon branches in the mini-BZ for a hypothetical A_2B_2 SL grown along the (001) direction.

Fig.19. Dispersion relations, along the $\Gamma - X$ axis, for longitudinal modes in bulk Ge (right), Ge_xSi_{1-x} (center) and Si (left). Adapted from ref. [51].

Fig.20.(a) Raman spectra of bulk $Ge_{0.5}Si_{0.5}$ (A) experimental and (B) calculated. Curves C and D are calculated spectra of a Ge_4Si_4 SL with rough and perfect interfaces respectively, while curve E shows the experimental spectrum of a strain-symmetrized Ge_4Si_4 SL. (b) Calculated eigenvibrations for this SL. From ref. [63].

Fig.21. Local density of states (LDOS) for L and T modes on the atomic planes along the (001) axis of a Ge_8Si_8 SL with two intermixed $Ge_{0.5}Si_{0.5}$ atomic layers at the interfaces. From ref [68].

Fig.22. (a) Comparison of experiment and theory for the positions of the major Raman peaks, for different λ_Ls, in the folded acoustic modes of a $Si/Ge_{0.48}Si_{0.52}$ SL: Full circles are experiment, crosses are results of the LC-model while the solid curves are calculated with the Ryotov model. (b) Raman spectra, simulated with the LC-model, of the same SL for a finite number of periods (N). From ref. [79].

Fig.23. (a) Calculated and (b) experimental spectra for NQW-samples; (c) calculated dispersion relations (lines) compared to experimental peak positions (circles) for the 1QW sample and $\lambda_L = 496.5nm$ and $\lambda_L = 514.5nm$. From ref. [83].

Fig.24. Intermediate frequency region of the Raman spectrum: (a) calculated, (b) experimental. From ref. [83].

Fig.25. (a) Dispersion relations of a Ge_4Si_4 SL for L (solid lines) and T-acoustic modes (dotted lines). Circles are peak positions in the Raman spectrum. (b) Experimental (upper curve) and calculated spectra for several Ge_nSi_m SLs (T=300K and $\lambda_L = 568.2nm$). from ref. [63].

Fig.26. Schematic representation of: (a) a two-band term in the resonant Raman cross section and (b) a PL process involving band to band recombination in a direct gap semiconductor.

Fig.27. Resonance in the room temperature Raman cross section for bulk Ge (full circles and triangles). The dashed curve is a guide for the eye while the solid one is a phenomenological representation of the contribution of three band terms. From ref. [85].

Fig.28. Raman cross section for LO and LA modes of several Ge_nSi_m as a function of laser photon energy. From ref. [87].

Fig.29. Raman efficiency of Ge_1 (squares), Si_1 (circles) and Si-Ge modes (triangles) of several Ge_nSi_m SLs and one Ge_7Si_3 SL for in-plane backscattering geometry from polished (110)-sample edges. Full symbols denote $y'(x'x')y'$ (light polarized $\perp$ to the layers). From ref. [89].

Fig.30. Calculated $\varepsilon_2(\omega)$ for a strain-symmetrized Ge_6Si_6 SL, decomposed into contributions from Ge (Ge-Ge) and Si (Si-Si) atoms. Solid lines are $\varepsilon_{2\parallel}(\omega)$ and dashed ones $\varepsilon_{2\perp}(\omega)$. from ref. [89].

Fig.31. Resonant cross sections of LA-modes in a $Ge_{12}Si_{12}$ SL (300K). From ref. [88].

Fig.32. (a) Off-resonance spectra of the Ge_1 LO-mode of the three NQW samples and (b) the same spectrum for the 6QW sample taken with different laser lines. From ref. [94].

Fig.33. (a) Raman spectrum of the Ge_1 TO-mode in the 6QW sample fitted with contributions from wells of different thicknesses (3, 4 and 5 MLs) and (b) the resonant cross section, $\alpha_n(\omega_L)$, for each of these contributions (circles, squares and diamonds) fitted to Lorentzian lineshapes (lines). The inset shows the position of these Lorentzian lines vs Ge layer thickness (circles) compared to and envelope-function calculation (line) for E_0-like states. From ref. [71].

Fig.34. Near-band-gap PL spectra for bulk Ge_xSi_{1-x} alloys. The optical transitions are labelled X_i^j where $j = NP$ when the transition is not phonon-assisted and nothing when it is and i specifies the type of phonon. From ref. [104].

Fig.35. PL spectra at 4.2K, after rapid thermal annealing, of Si/Ge_xSi_{1-x} QWs of different widths (d) and compositions (x). adapted from ref. [24].

Fig.36. (a) PL spectra, at 4K, of four $Si/Ge_{0.8}Si_{0.2}$ QWs of different widths (d) and, (b) band-gap vs d at 4K (triangles) and 77K (squares). The solid line is an envelope function

calculation for each case. from ref. [108].

Fig.37. PL spectra, at 2K, of several Si/Ge_xSi_{1-x} QWs grown by MBE at 600^0C : (a) $d = 2.7nm$ and $x = 0.15$, (b) $d = 5.2nm$ and $x = 0.15$ and (c) $d = 6.8nm$ and $x = 0.19$. The broad minimum near 890 meV is instrumental. From ref. [112].

Fig.38. PL spectra, at 2K, of one Si/Ge_xSi_{1-x} QW ($d \backsim 6nm$, $x = 0.20$) (a) as-grown, (b) after $!0^{10}cm^{-2}$ 50 Kev Si^{+29} implant, (c) after 10 min annealing at 600^0C (no implant), (d) after same anneal of the implanted sample, (e) after $10^{11}cm^{-2}$ implant followed by 600^0C anneal, (f) after $10^{12}cm^{-2}$ implant followed by 600^0C anneal, and (g) after $!0^{10}cm^{-2}$ implant followed by anneal at 800^0C. In (g) the Si PL was suppressed by a filter. From ref. [119].

Fig.39. PL, at 2K, of Si/Ge_xSi_{1-x} QWs with 600^0C anneals both directly after growth (dashed lines) and after implant (solid lines). From ref. [119].

Table I. Measured energies (eV) of prominent structures in the optical spectra of bulk Si and Ge. All data refer to low temperature measurements, except for the E_0 transition of Si which has been taken at room temperature, compiled from data listed in ref [1].

Transition	Si, $\hbar\omega$(eV)	Ge, $\hbar\omega$(eV)
E_0	4.185	0.898
$E_0 + \Delta_0$	4.229	1.184
E_1	3.45	2.222
$E_1 + \Delta_1$	—	2.41
E_0'	3.378	3.206
$E_0' + \Delta_0'$	—	3.39
E_2	4.330	4.49
E_1'	5.50	5.65

Table II. Transition energies obtained both for experimental ER data and from an envelope-function calculation (including non-parabolicities in the conduction band) for the Ge/Ge_xSi_{1-x} SL of Fig. 12, with $\Delta E_a \simeq 0.14eV$. Here $nh(nl)$ denotes the transition between the n^{th} confined level of the heavy (light) hole band to the corresponding level at the conduction band. The label $\Gamma(\Pi)$ corresponds to transitions at the mini-zone center(edge). From ref. [39].

Line	Transition Energy (eV)		Assignment
	Experimental	Theory	
		0.953	1hΓ
A	0.948		
		0.957	1hΠ
		0.962	1lΓ
B	0.963		
		0.978	1hΓ
		1.099	1hΠ
C	1.102		
		1.111	2hΓ
D	1.136	1.136	2lΠ
E	1.176	1.177	2lΓ
		1.308	3hΓ
F	1.324		
		1.330	3hΓ
G	1.547	1.548	4hΠ
H	1.595	1.595	4hΓ

Table III. Critical point energies of Ge_nSi_m strain-symmetrized SLs from the fittings of the ER spectra(77K) with Eq.(1). Also listed are the assignements of th LMTO calculation of ref. [44] and the envelope calculations for the E_0 optical gap. E_{abs} is the onset of strong absorption in these samples determined from the interface pattern. From ref [46].

Sample	Experimental		Assignment	Theoretical	
	C_j Γ_j $E_j(eV)$			LMTO	EF
		E_{abs}(eV)		$E_j(eV)$	$E_0(eV)$
Ge_4Si_4	0.49 0.10 2.31	2.30	E_1^a	2.31	2.31
	0.59 0.12 2.42		E_0	2.35	
	0.59 0.15 2.58		E_1^b	2.48	
	0.69 0.14 2.80		E_1^c	2.68	
	1.00 0.16 3.03		E_1^d	3.01	
			E_1^e,E_0'	3.26	
Ge_5Si_5	0.50 0.20 2.30A	2.43	E_1^a	2.23	2.25
	0.69 0.10 2.50B		$E_0(hh)$	2.25	
	0.69 0.10 2.55C		$E_0(lh)$	2.31	
	1.13 0.17 2.64D		E_1^b	2.72	
	0.81 0.12 2.82E		E_1^c	2.79	
	1.00 0.15 3.05F		E_1^d	2.93	
	0.64 0.16 3.36G		E_0'		
Ge_6Si_6	0.27 0.20 2.30	2.59	E_1^a	2.30	2.56
	1.13 0.10 2.60		$E_0(hh)$	2.55	
	0.93 0.10 2.66		$E_0(lh)$	2.60	
	1.43 0.17 2.73		E_1^b	2.75	
	1.20 0.12 2.94		E_1^c	3.00	
	1.00 0.15 3.07		E_1^d	3.11	
	0.53 0.14 3.37		E_0'		

Table IV. Transition energies (E_j) and broadenings (Γ_j) of the lines in the ER spectra of NQW samples. Assignments are shown in the third column while the last column lists the degree of confinement of the electronic states participating in the transition from RRS data. From ref [41].

Sample	ER(77K)	Assignment	Confinement
	E_j (Γ_j) (in eV)		
1QW	2.83(0.11) A	E_1	Ge
2QW	2.72(0.17) A	E_1^+	Mostly Ge
	2.98(0.18) B	E_1^-	Mostly Si
6QW	2.43(0.12) A	E_1^a	Mostly Ge
	2.59(0.10) B	E_1^b	Mostly Ge
	2.74(0.15) C	E_1^c	Mostly Si
	2.97(0.12) D	E_1^d	Mostly Si

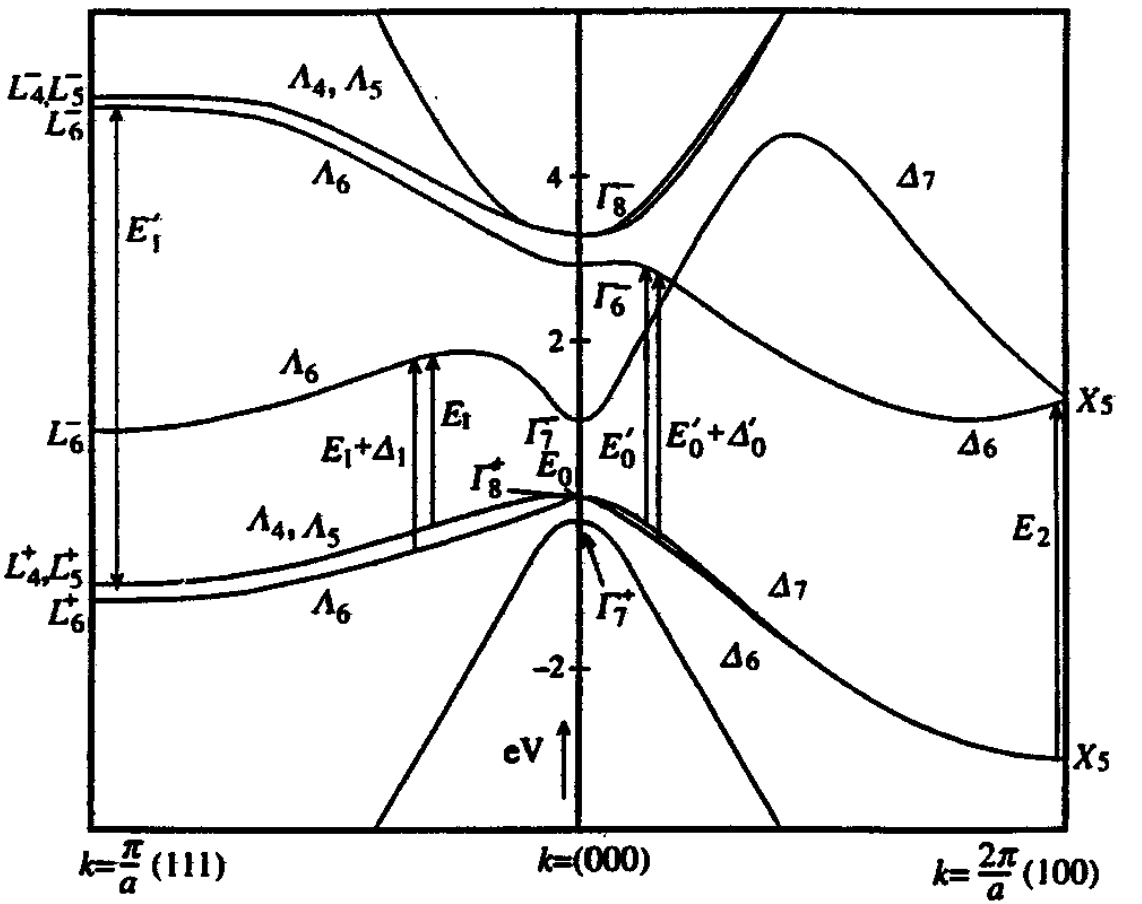
L_4^-, L_5^-
L_6^-
Λ_4, Λ_5
Λ_6
E_1'
4
Γ_8^-
Δ_7
Γ_6^-
2
Λ_6
X_5
L_6^-
E_1
$E_1+\Delta_1$
Γ_7^-
E_0'
$E_0'+\Delta_0'$
Δ_6
Γ_8^+
E_0
Λ_4, Λ_5
E_2
L_4^+, L_5^+
L_6^+
Λ_6
Γ_7^+
Δ_7
Δ_6
-2
eV
X_5
$k=\frac{\pi}{a}$ (111)
k=(000)
$k=\frac{2\pi}{a}$ (100)

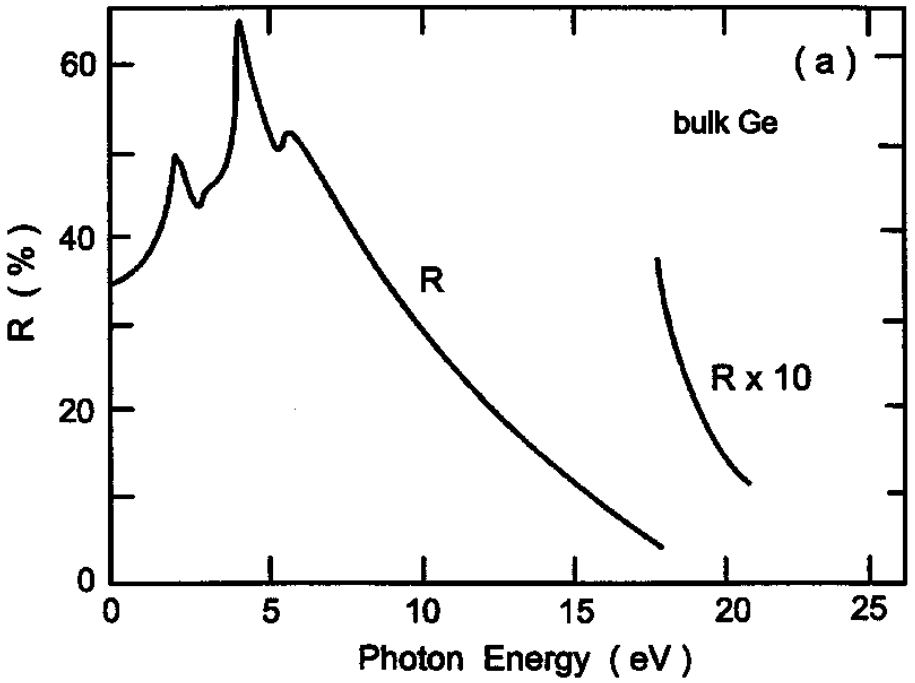
(a)
bulk Ge
R
R x 10
R (%)
60
40
20
0
0
5
10
15
20
25
Photon Energy (eV)

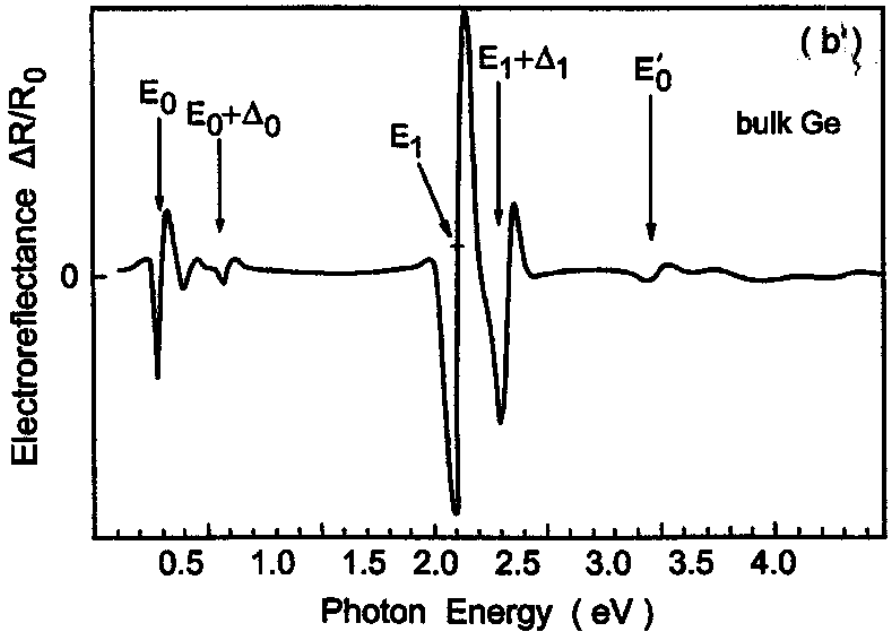
(b)
bulk Ge
E0
E0+Δ0
E1
E1+Δ1
E'0
Electroreflectance ΔR/R0
0
0.5
1.0
1.5
2.0
2.5
3.0
3.5
4.0
Photon Energy (eV)

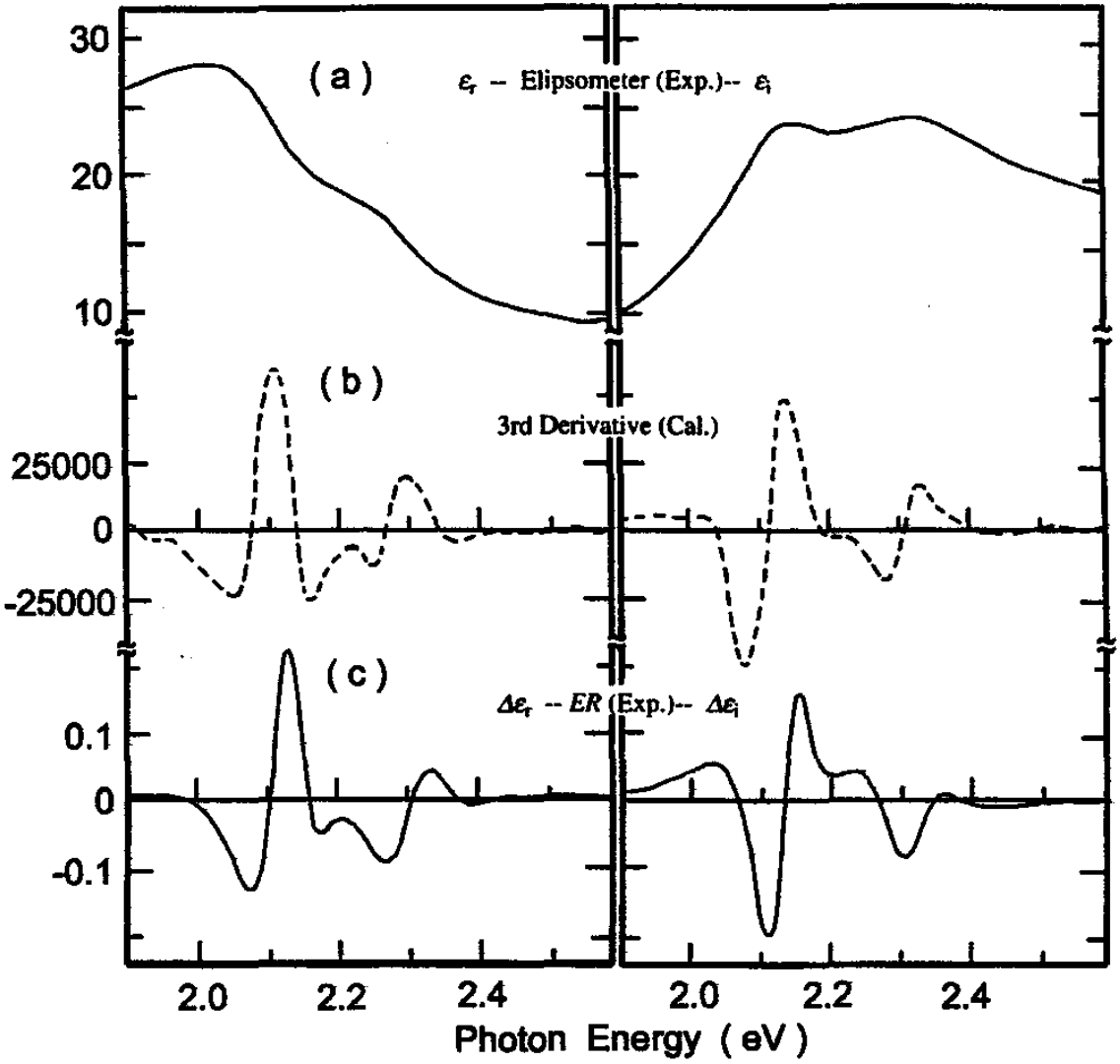
30
20
10
(a)
ε_r -- Elipsometer (Exp.)-- ε_i
(b)
3rd Derivative (Cal.)
25000
0
-25000
(c)
$\Delta\varepsilon_r$ -- ER (Exp.)-- $\Delta\varepsilon_i$
0.1
0
-0.1
2.0
2.2
2.4
2.0
2.2
2.4
Photon Energy (eV)

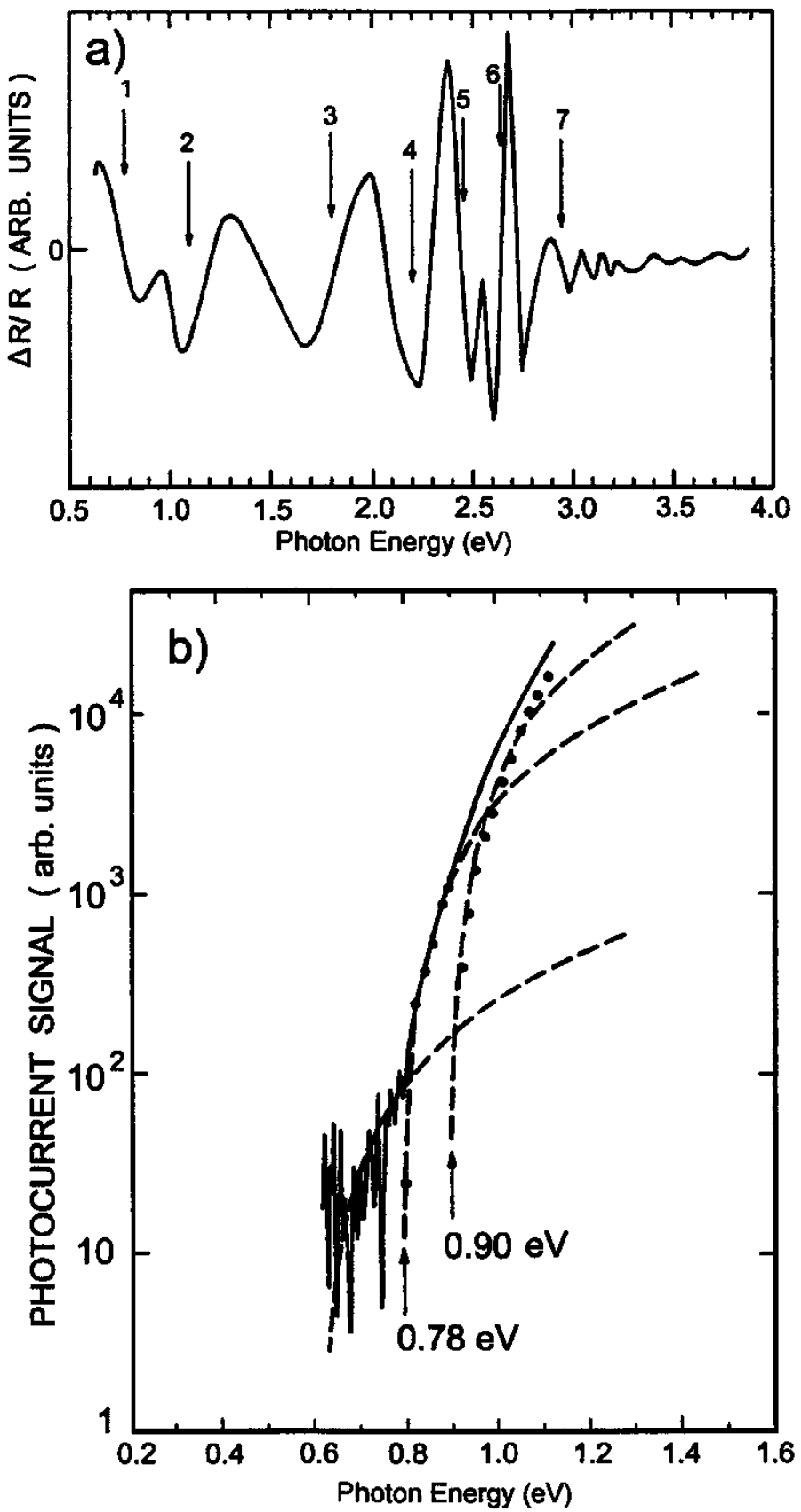
a)
1
2
3
4
5
6
7
ΔR/R (ARB. UNITS)
0
0.5
1.0
1.5
2.0
2.5
3.0
3.5
4.0
Photon Energy (eV)
b)
PHOTOCURRENT SIGNAL (arb. units)
10^4
10^3
10^2
10
1
0.90 eV
0.78 eV
0.2
0.4
0.6
0.8
1.0
1.2
1.4
1.6
Photon Energy (eV)

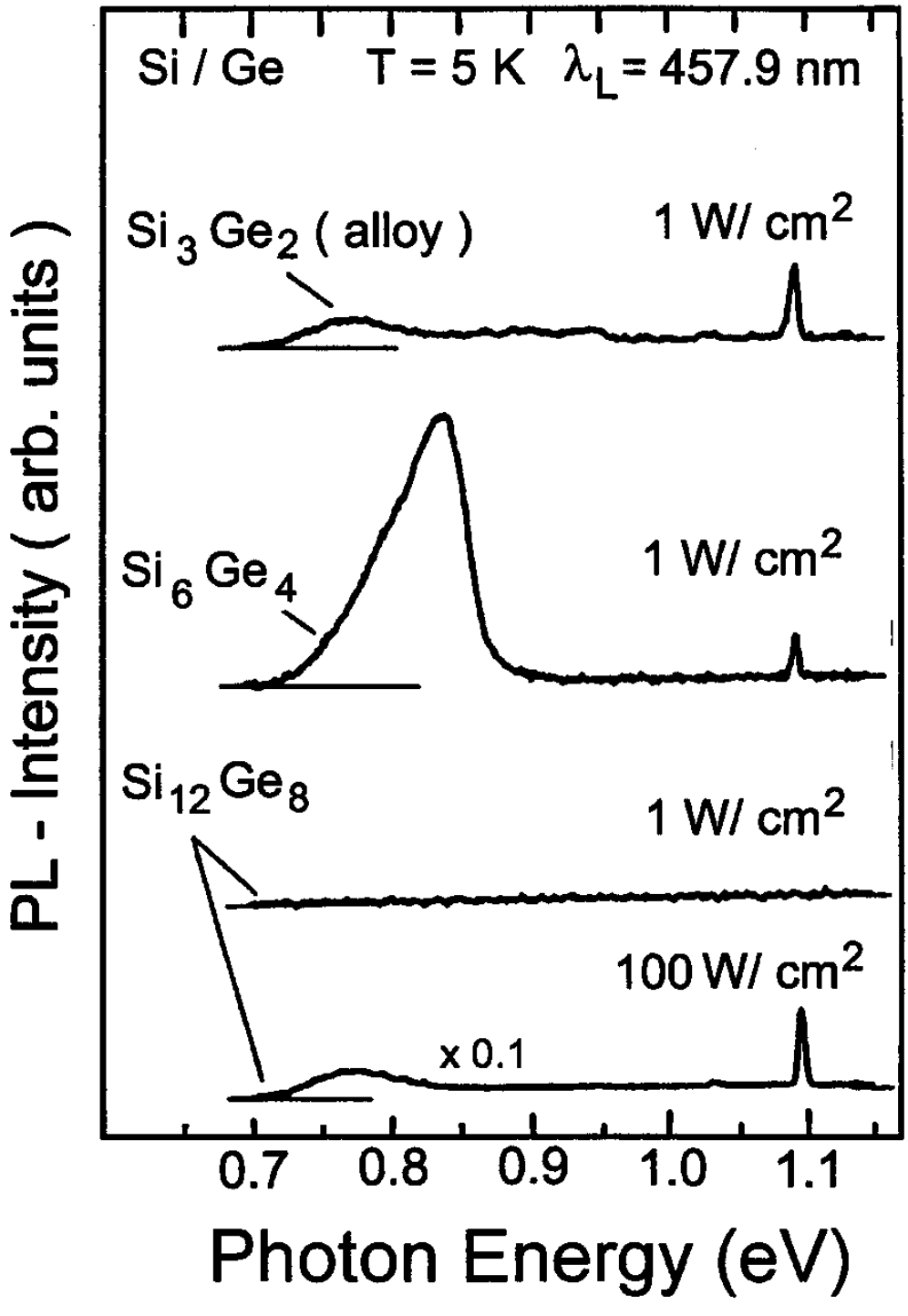
Si / Ge T = 5 K λL = 457.9 nm
Si3 Ge2 (alloy)
1 W/ cm2
Si6 Ge4
1 W/ cm2
Si12 Ge8
1 W/ cm2
100 W/ cm2
x 0.1
PL - Intensity (arb. units)
0.7
0.8
0.9
1.0
1.1
Photon Energy (eV)

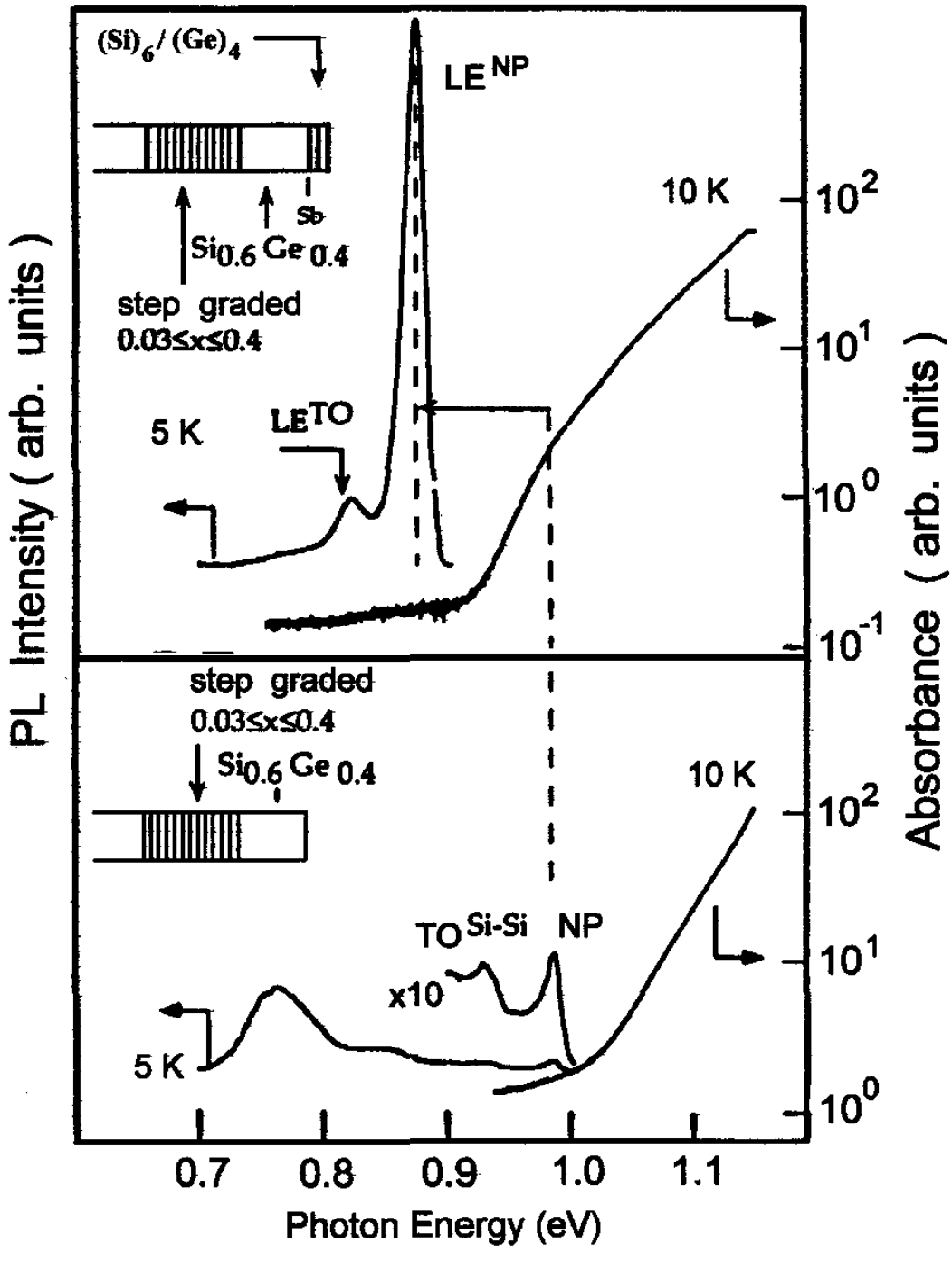
(Si)6/ (Ge)4
LE NP
10 K
Sb
Si0.6 Ge 0.4
step graded
0.03≤x≤0.4
5 K
LETO
step graded
0.03≤x≤0.4
Si0.6 Ge 0.4
10 K
TO Si-Si NP
x10
5 K
PL Intensity (arb. units)
Absorbance (arb. units)
10^2
10^1
10^0
10^-1
0.7
0.8
0.9
1.0
1.1
Photon Energy (eV)

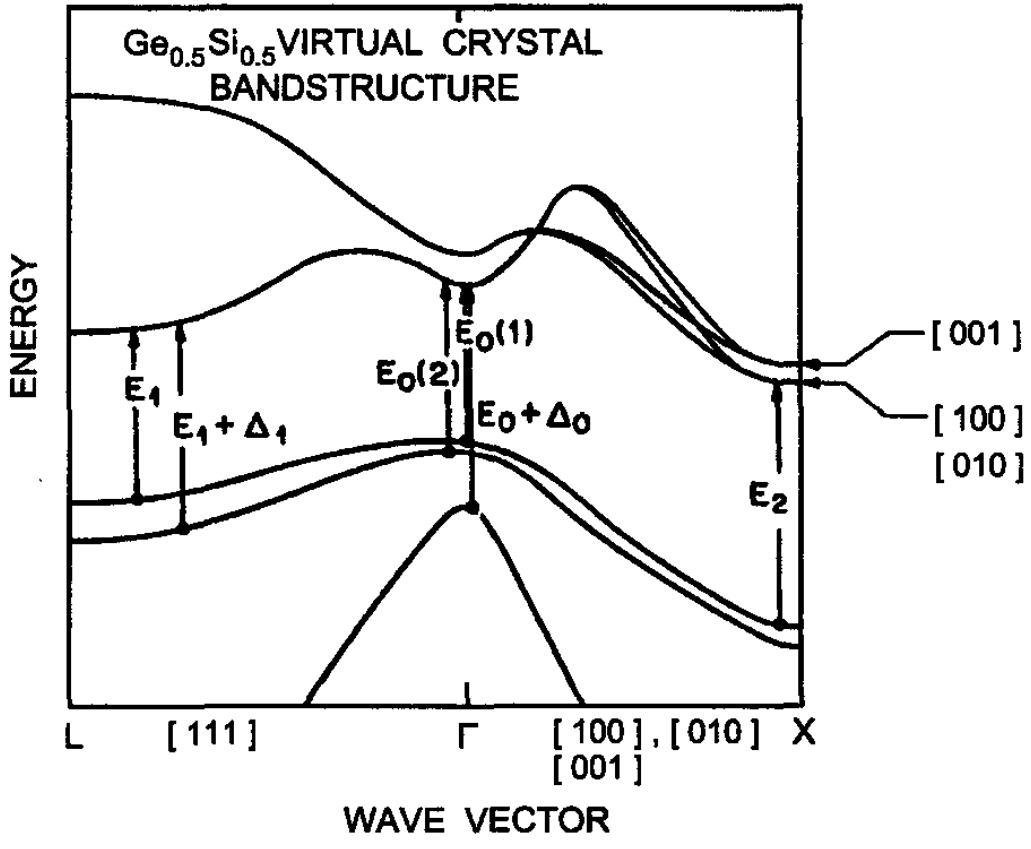
$Ge_{0.5}Si_{0.5}$ VIRTUAL CRYSTAL BANDSTRUCTURE
ENERGY
E_1
$E_1 + \Delta_1$
$E_0(2)$
$E_0(1)$
$E_0 + \Delta_0$
E_2
[001]
[100]
[010]
L
[111]
Γ
[100], [010]
[001]
X
WAVE VECTOR

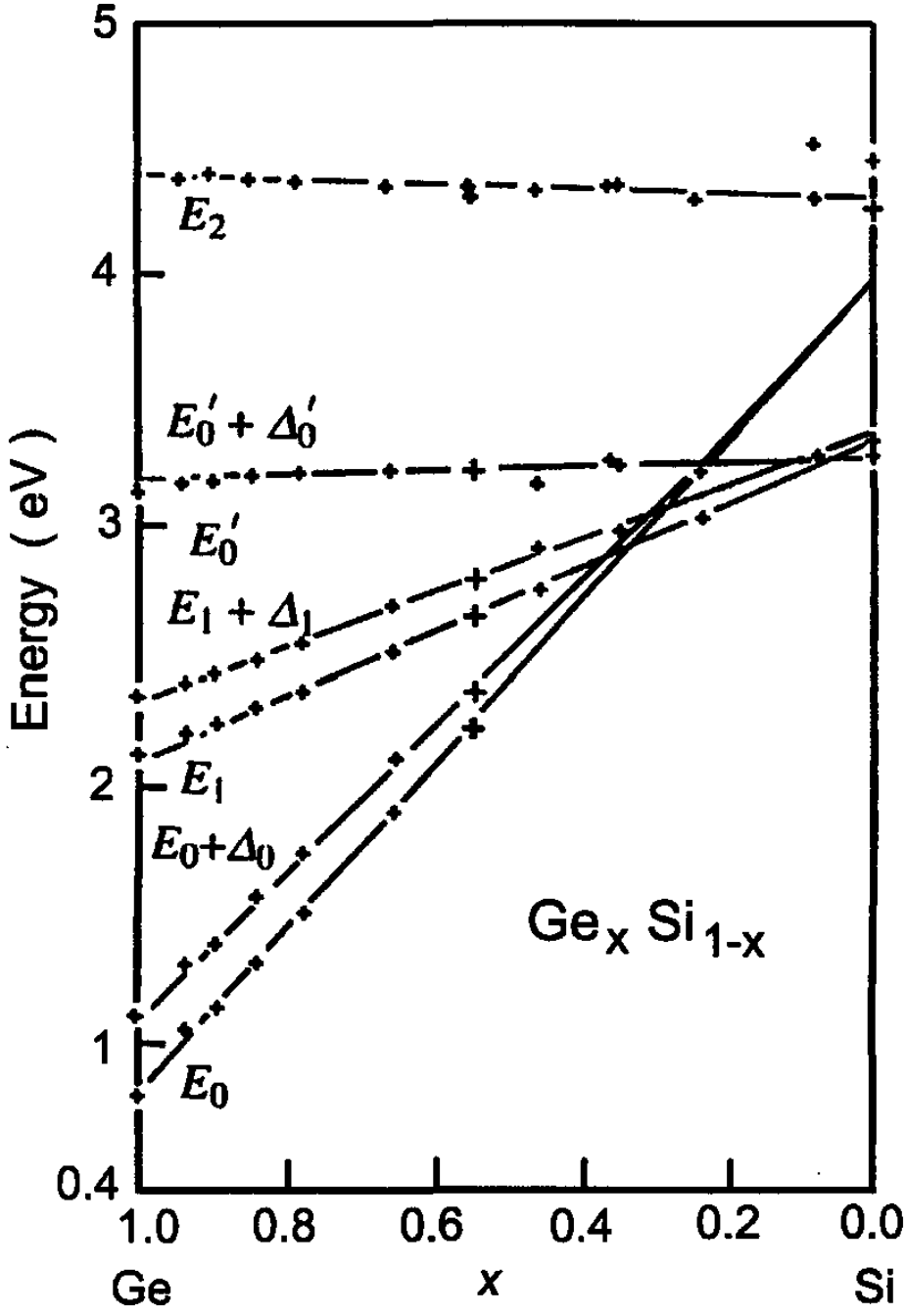
5
4
3
2
1
0.4
Energy (eV)
E_2
$E_0' + \Delta_0'$
E_0'
$E_1 + \Delta_1$
E_1
$E_0+\Delta_0$
E_0
$Ge_x Si_{1-x}$
1.0
0.8
0.6
0.4
0.2
0.0
Ge
x
Si

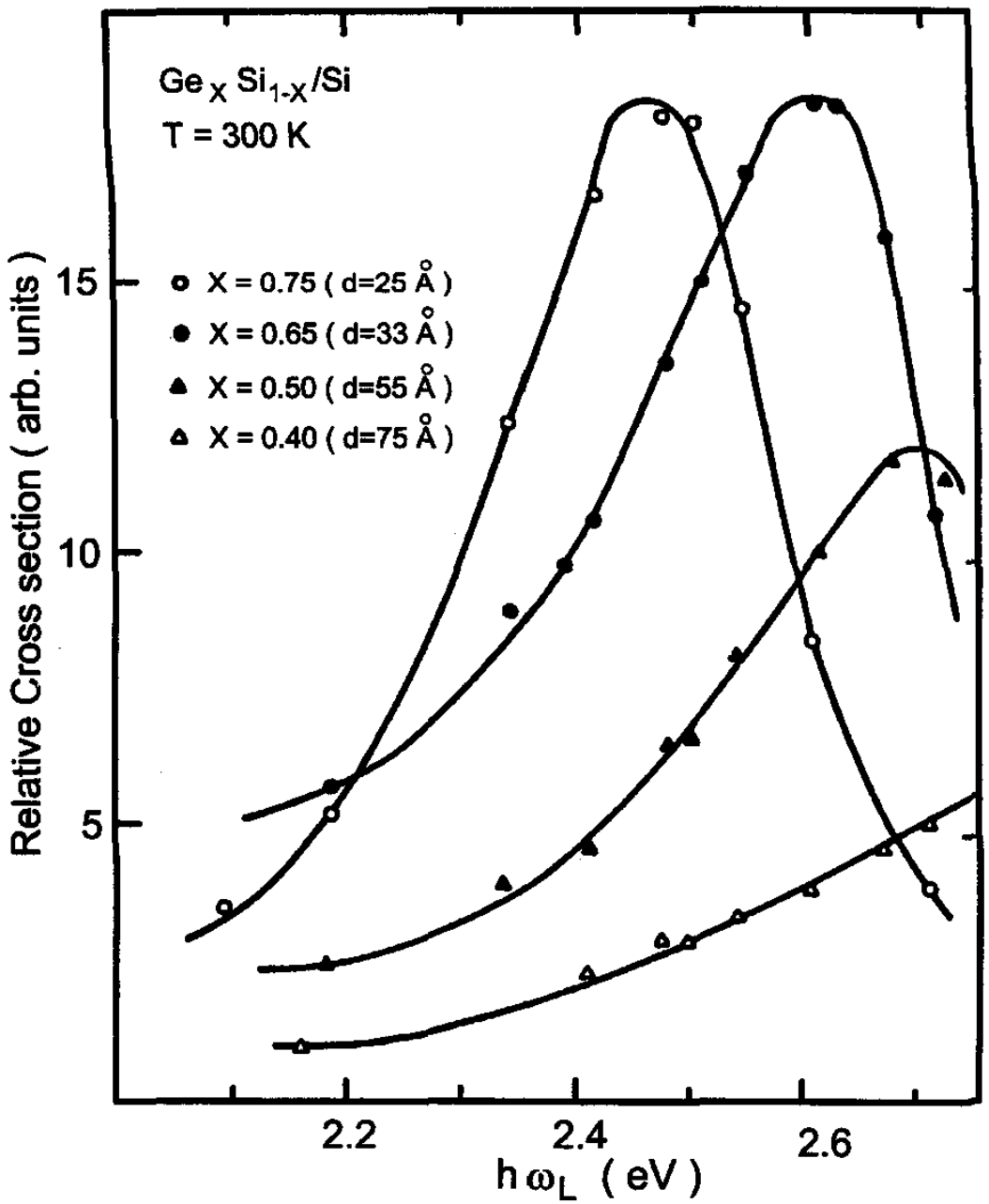
Ge X Si 1-X /Si
T = 300 K
X = 0.75 (d=25 Å)
X = 0.65 (d=33 Å)
X = 0.50 (d=55 Å)
X = 0.40 (d=75 Å)
Relative Cross section (arb. units)
15
10
5
2.2
2.4
2.6
h ω L (eV)

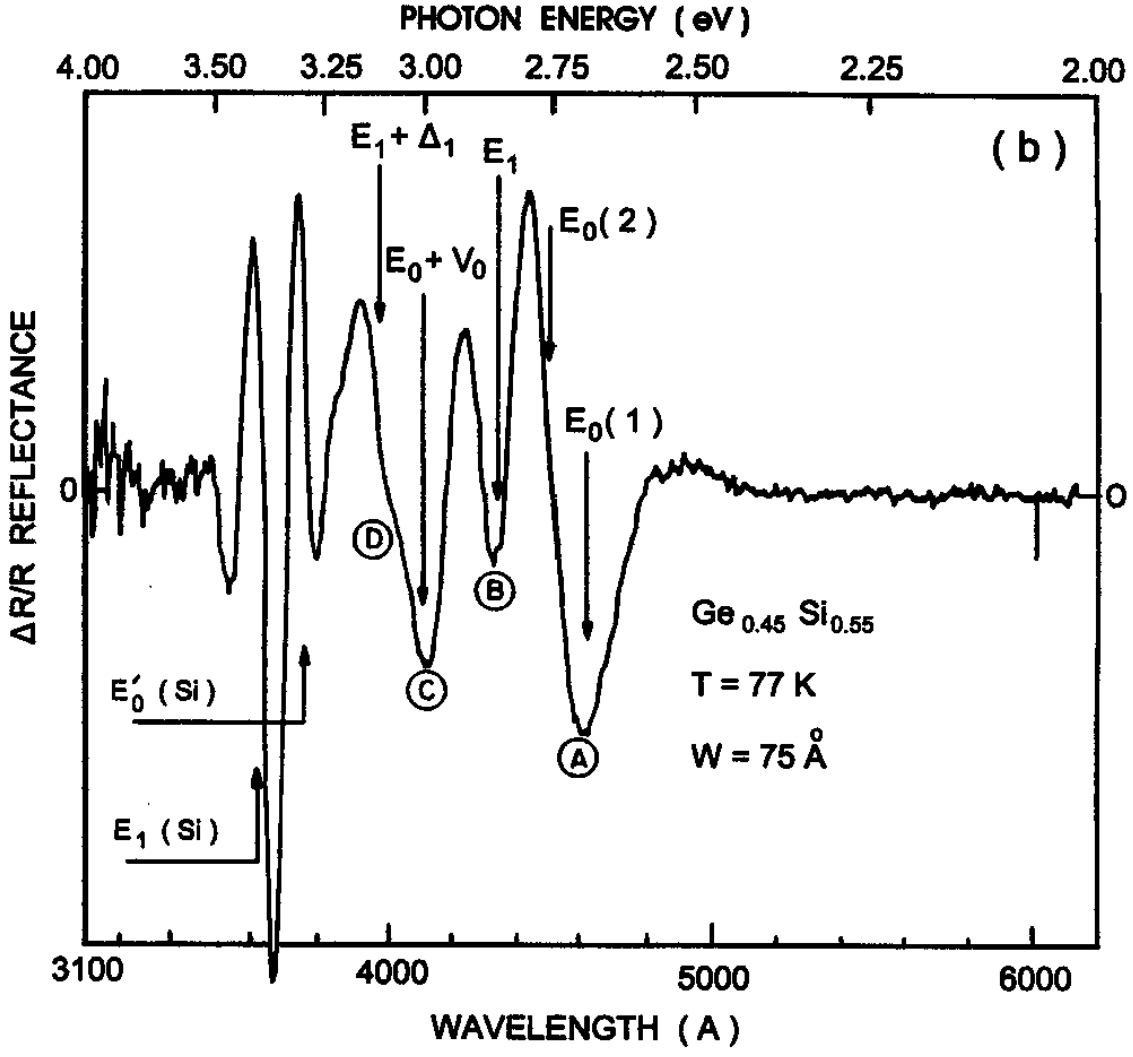
PHOTON ENERGY (eV)
4.00
3.50
3.25
3.00
2.75
2.50
2.25
2.00
(b)
$E_1 + \Delta_1$
E_1
$E_0 + V_0$
$E_0(2)$
$E_0(1)$
ΔR/R REFLECTANCE
0
0
D
B
C
A
E_0' (Si)
E_1 (Si)
$Ge_{0.45}$ $Si_{0.55}$
T = 77 K
W = 75 Å
3100
4000
5000
6000
WAVELENGTH (A)

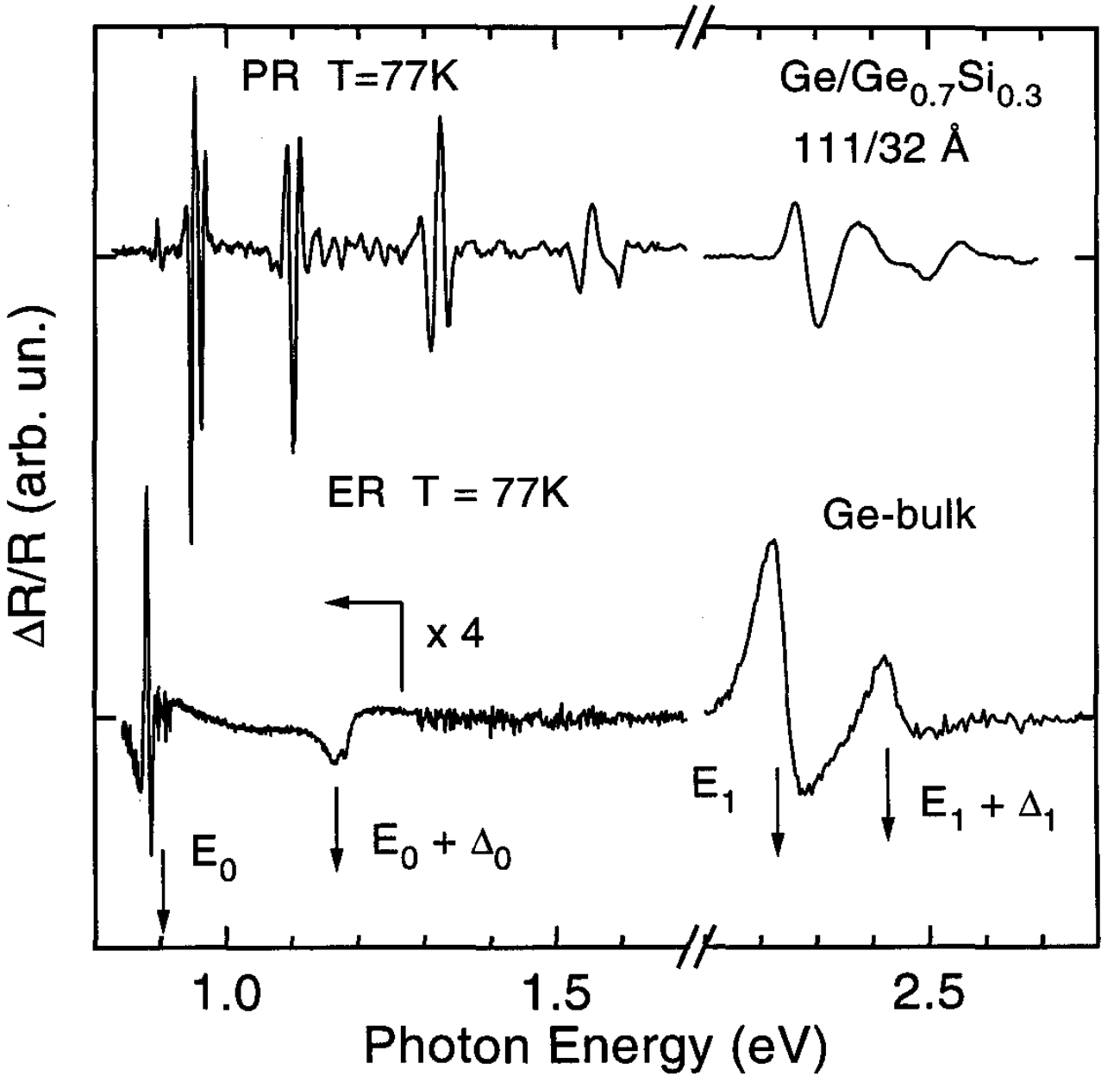
PR T=77K
Ge/Ge0.7Si0.3
111/32 Å
ER T = 77K
Ge-bulk
x 4
E0
E0 + Δ0
E1
E1 + Δ1
ΔR/R (arb. un.)
1.0
1.5
2.5
Photon Energy (eV)

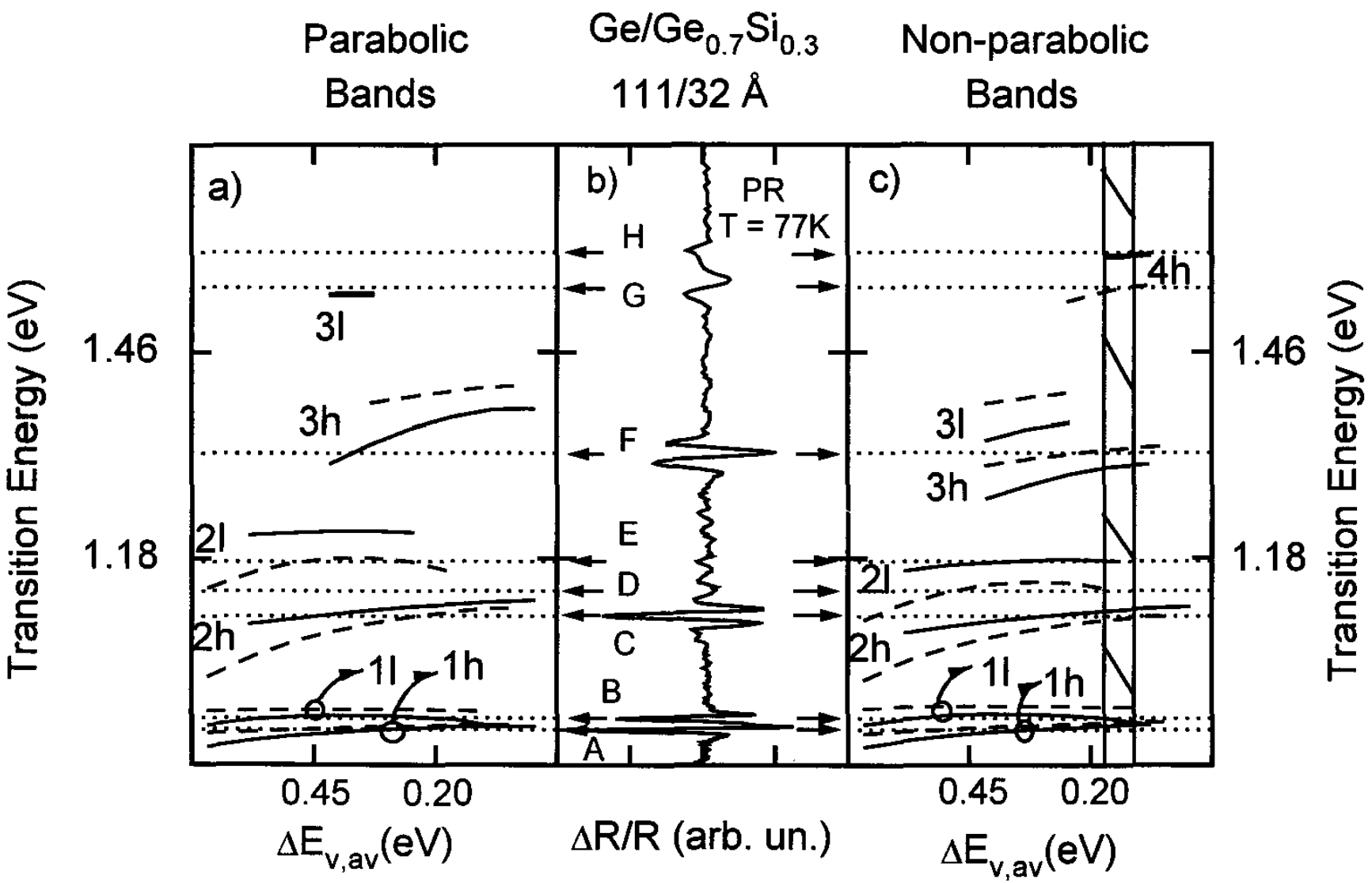
Parabolic Bands
Ge/Ge0.7Si0.3
111/32 Å
Non-parabolic Bands
a)
b)
PR
T = 77K
c)
H
G
F
E
D
C
B
A
3l
3h
2l
2h
1l
1h
4h
1.46
1.18
Transition Energy (eV)
0.45
0.20
ΔEv,av(eV)
ΔR/R (arb. un.)

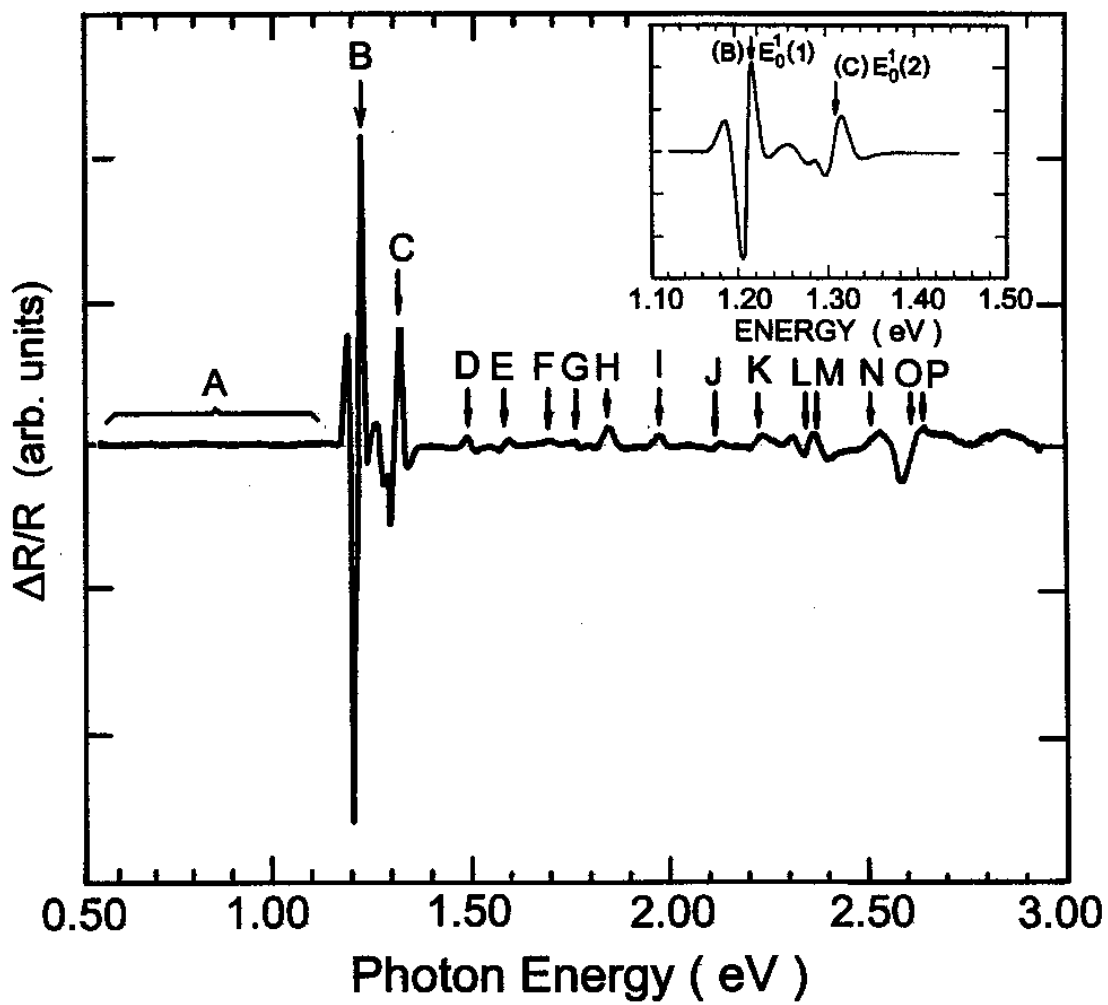
B
C
A
D E F G H
I
J
K
L M
N
O P
(B) $E_0^1(1)$
(C) $E_0^1(2)$
1.10 1.20 1.30 1.40 1.50
ENERGY (eV)
ΔR/R (arb. units)
0.50 1.00 1.50 2.00 2.50 3.00
Photon Energy (eV)

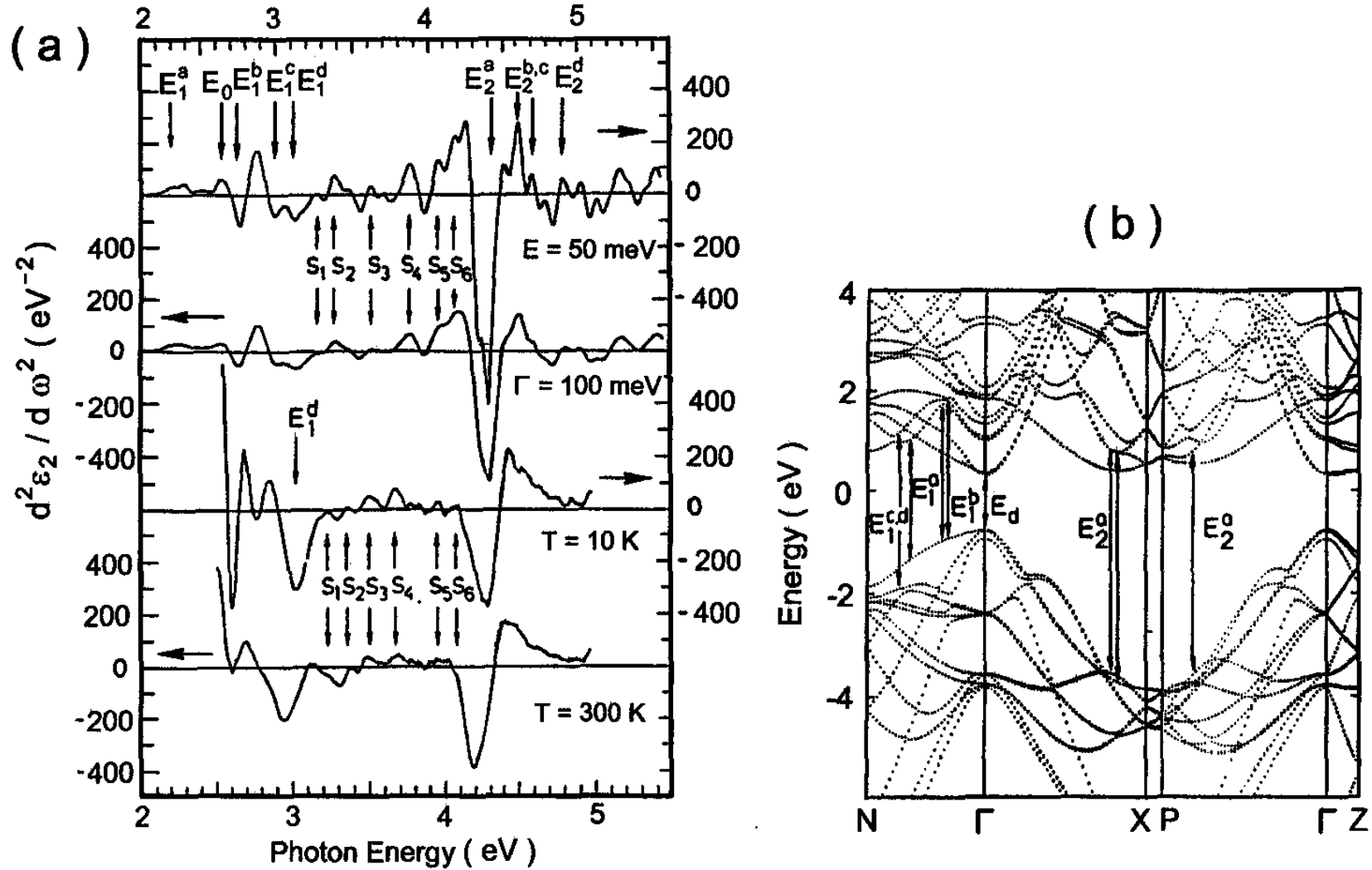
(a)
(b)
E_1^a E_0 E_1^b E_1^c E_1^d
E_2^a $E_2^{b,c}$ E_2^d
E = 50 meV
Γ = 100 meV
T = 10 K
T = 300 K
S_1 S_2 S_3 S_4 S_5 S_6
$d^2\varepsilon_2 / d\omega^2$ (eV^{-2})
Photon Energy (eV)
Energy (eV)
$E_1^{c,d}$ E_1^a E_1^b E_d
E_2^a E_2^a
N Γ X P Γ Z

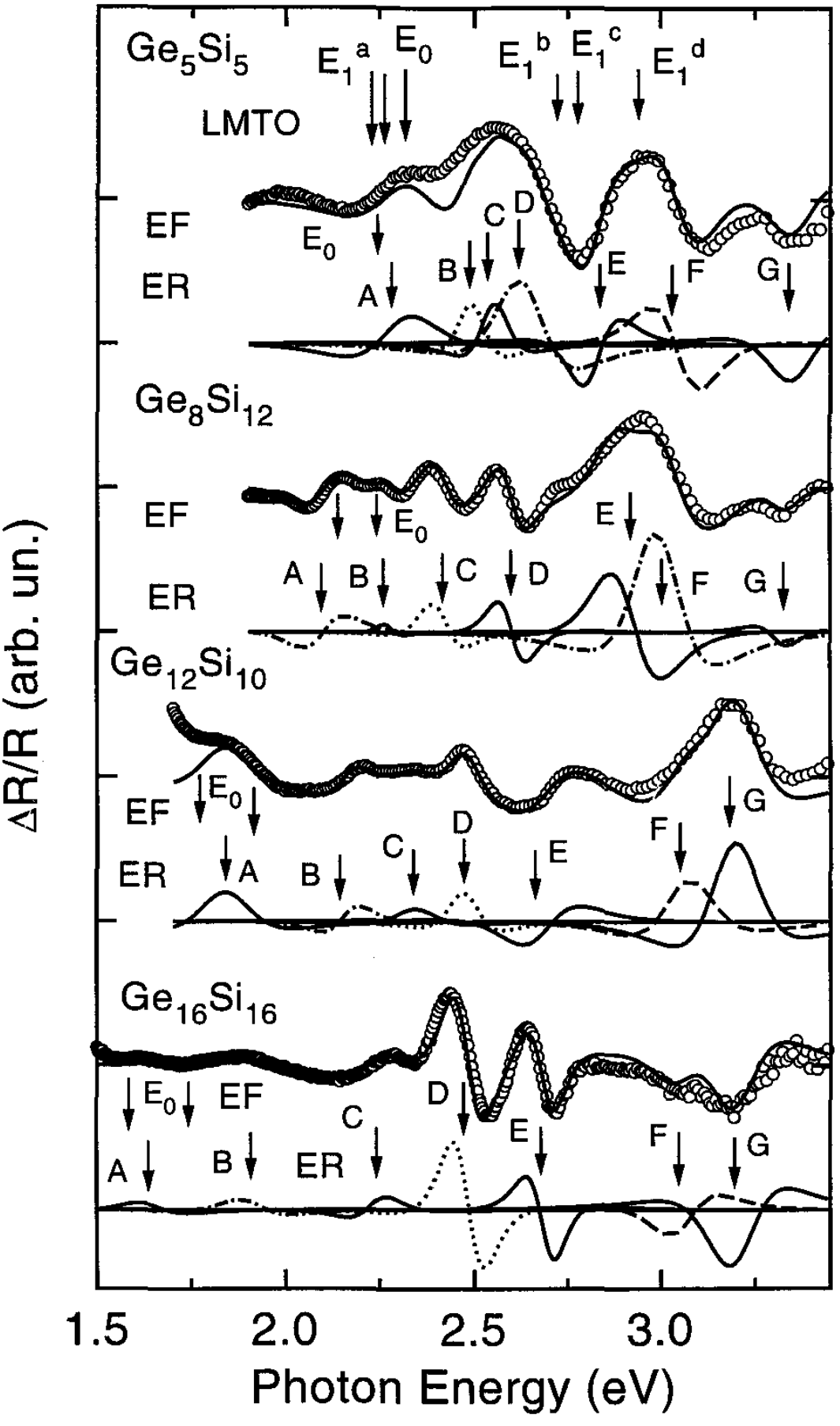
Ge5Si5
E1a
E0
E1b
E1c
E1d
LMTO
EF
ER
E0
A
B
C
D
E
F
G
Ge8Si12
Ge12Si10
Ge16Si16
ΔR/R (arb. un.)
1.5
2.0
2.5
3.0
Photon Energy (eV)

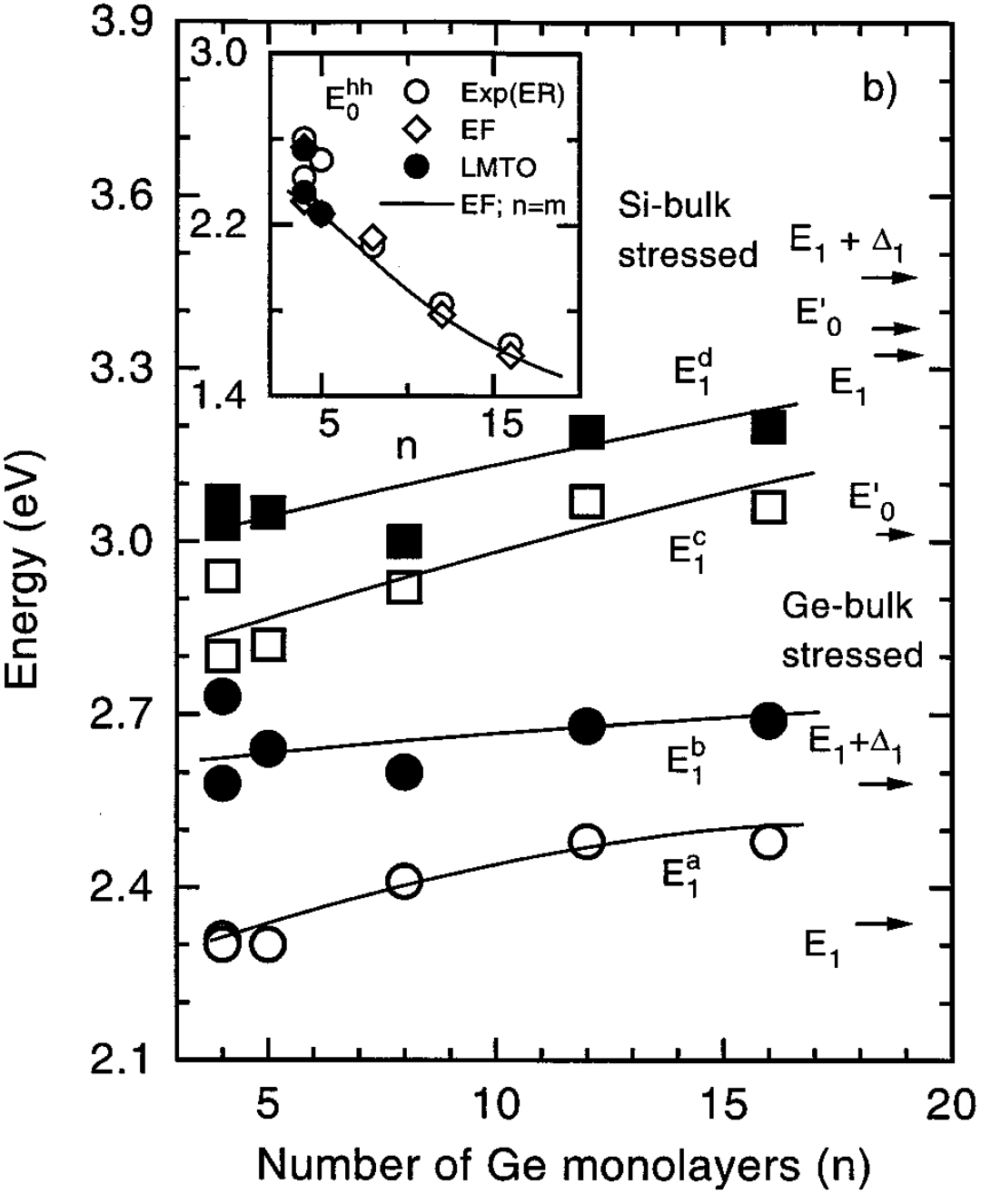
b)
Energy (eV)
Number of Ge monolayers (n)
Si-bulk
stressed
Ge-bulk
stressed
$E_1 + \Delta_1$
E'_0
E_1
E_1^d
E_1^c
E_1^b
E_1^a
$E_1+\Delta_1$
E_0^{hh}
Exp(ER)
EF
LMTO
EF; n=m
n

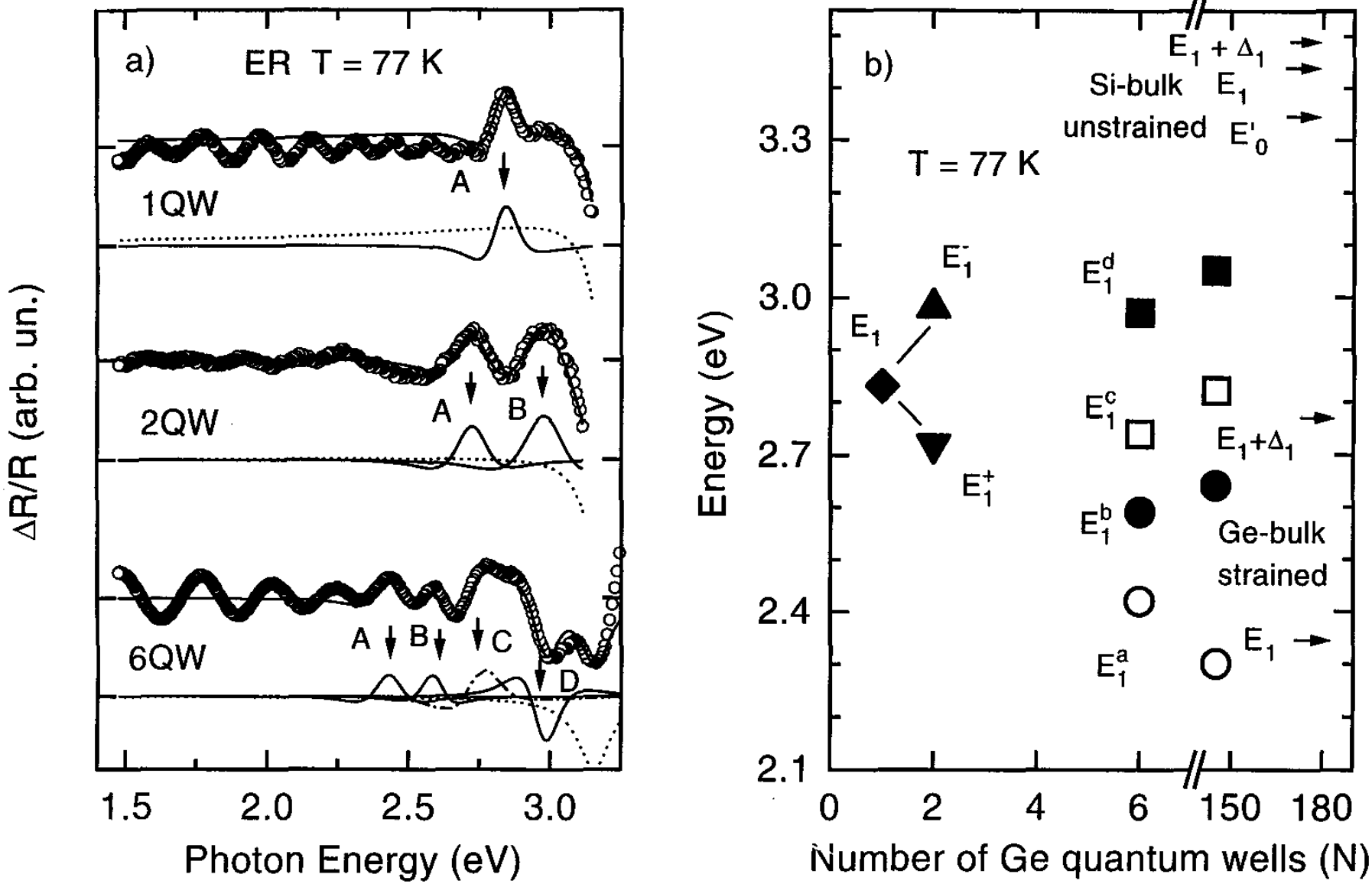
a)
ER T = 77 K
1QW
2QW
6QW
A
B
C
D
ΔR/R (arb. un.)
1.5
2.0
2.5
3.0
Photon Energy (eV)
b)
T = 77 K
$E_1 + \Delta_1$
Si-bulk E_1
unstrained E'_0
E_1^-
E_1
E_1^+
E_1^d
E_1^c
E_1^b
E_1^a
$E_1+\Delta_1$
Ge-bulk
strained
E_1
Energy (eV)
3.3
3.0
2.7
2.4
2.1
0
2
4
6
150
180
Number of Ge quantum wells (N)

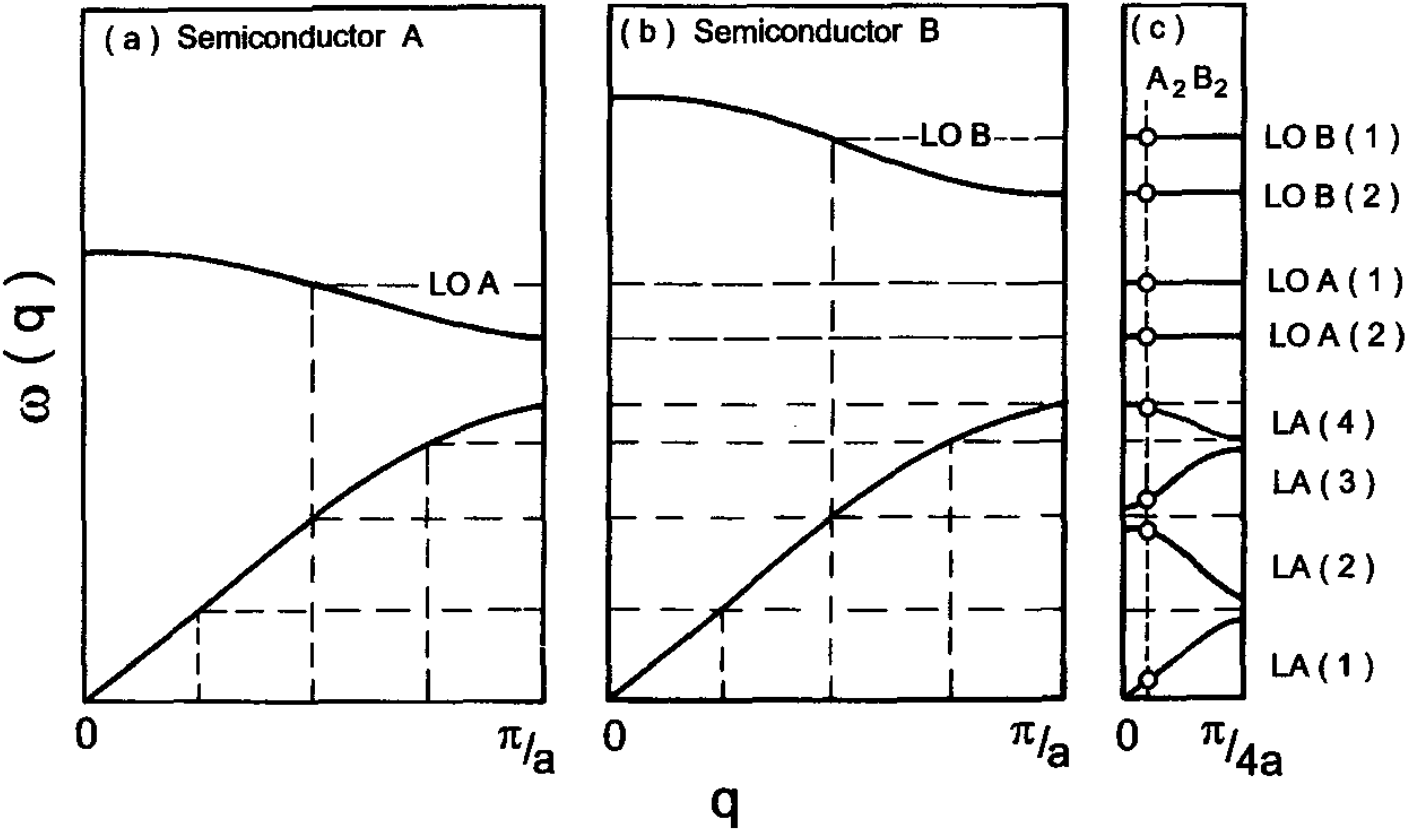
(a) Semiconductor A
LO A
(b) Semiconductor B
LO B
(c)
A2B2
LO B (1)
LO B (2)
LO A (1)
LO A (2)
LA (4)
LA (3)
LA (2)
LA (1)
ω (q)
0
π/a
0
π/a
0
π/4a
q

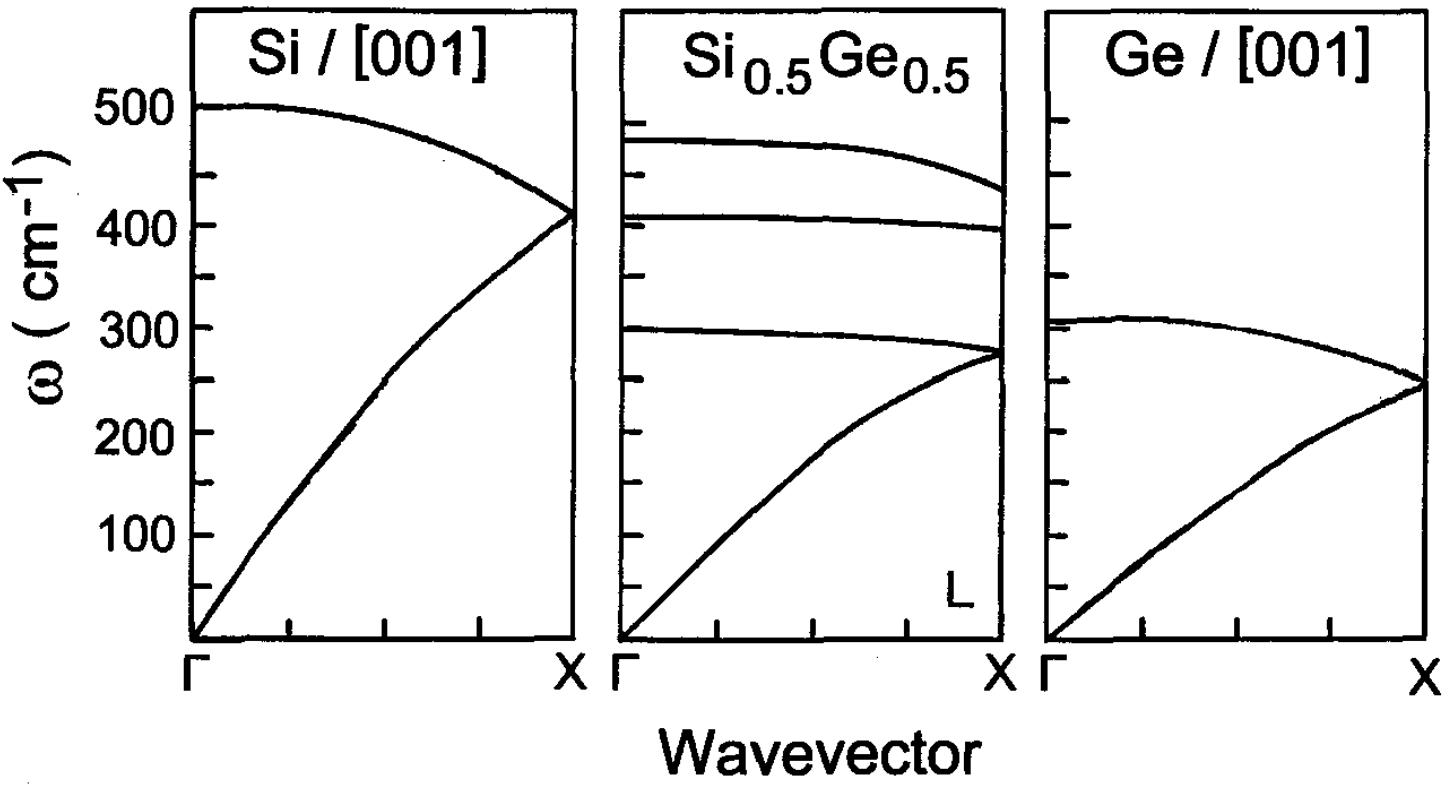
Si / [001]
Si0.5Ge0.5
Ge / [001]
500
400
300
200
100
ω (cm-1)
L
Γ
X
Γ
X
Γ
X
Wavevector

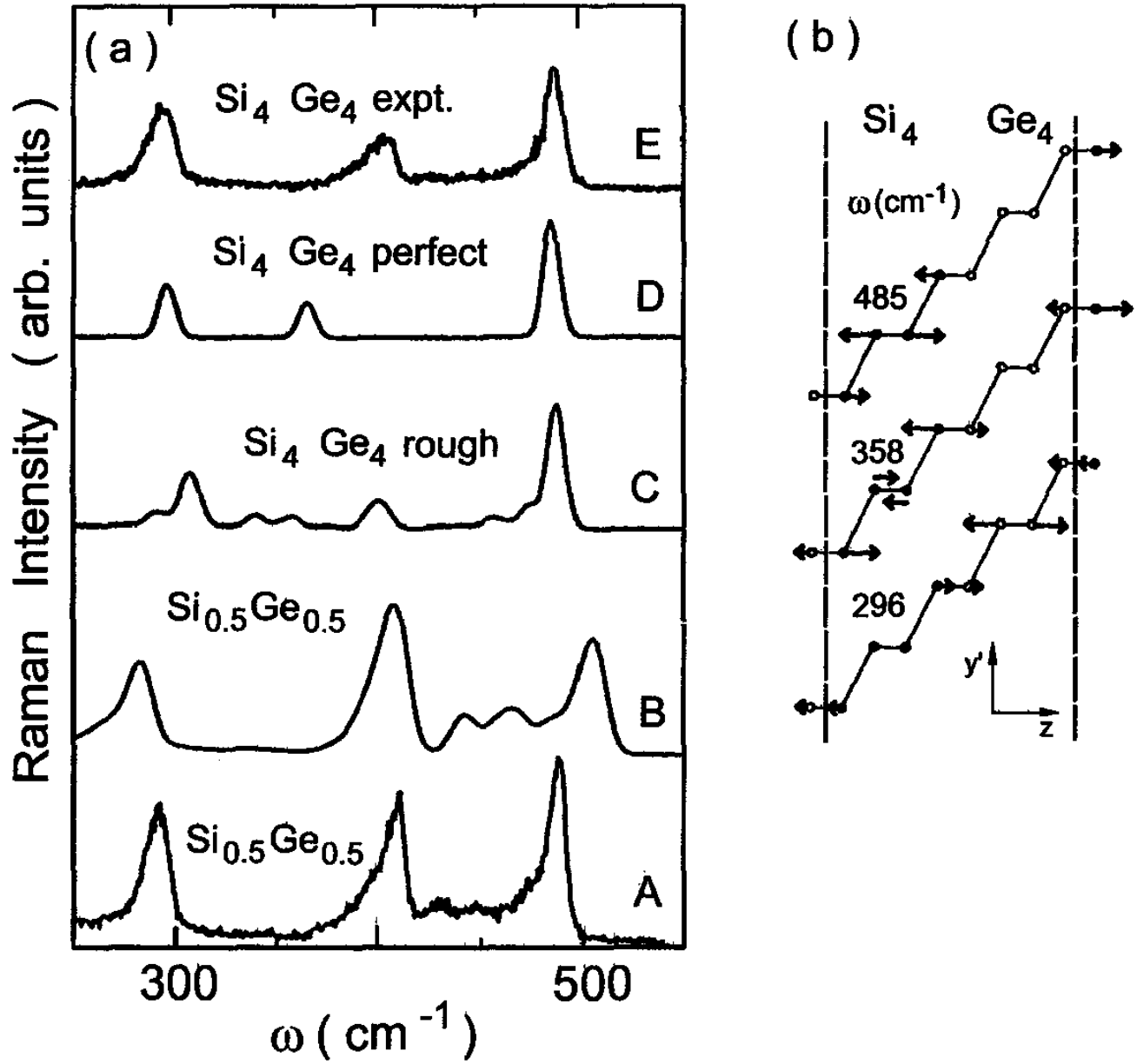
(a)
Si4 Ge4 expt.
E
Si4 Ge4 perfect
D
Si4 Ge4 rough
C
Si0.5Ge0.5
B
Si0.5Ge0.5
A
Raman Intensity (arb. units)
300
500
ω (cm-1)
(b)
Si4
Ge4
ω(cm-1)
485
358
296
y'
z

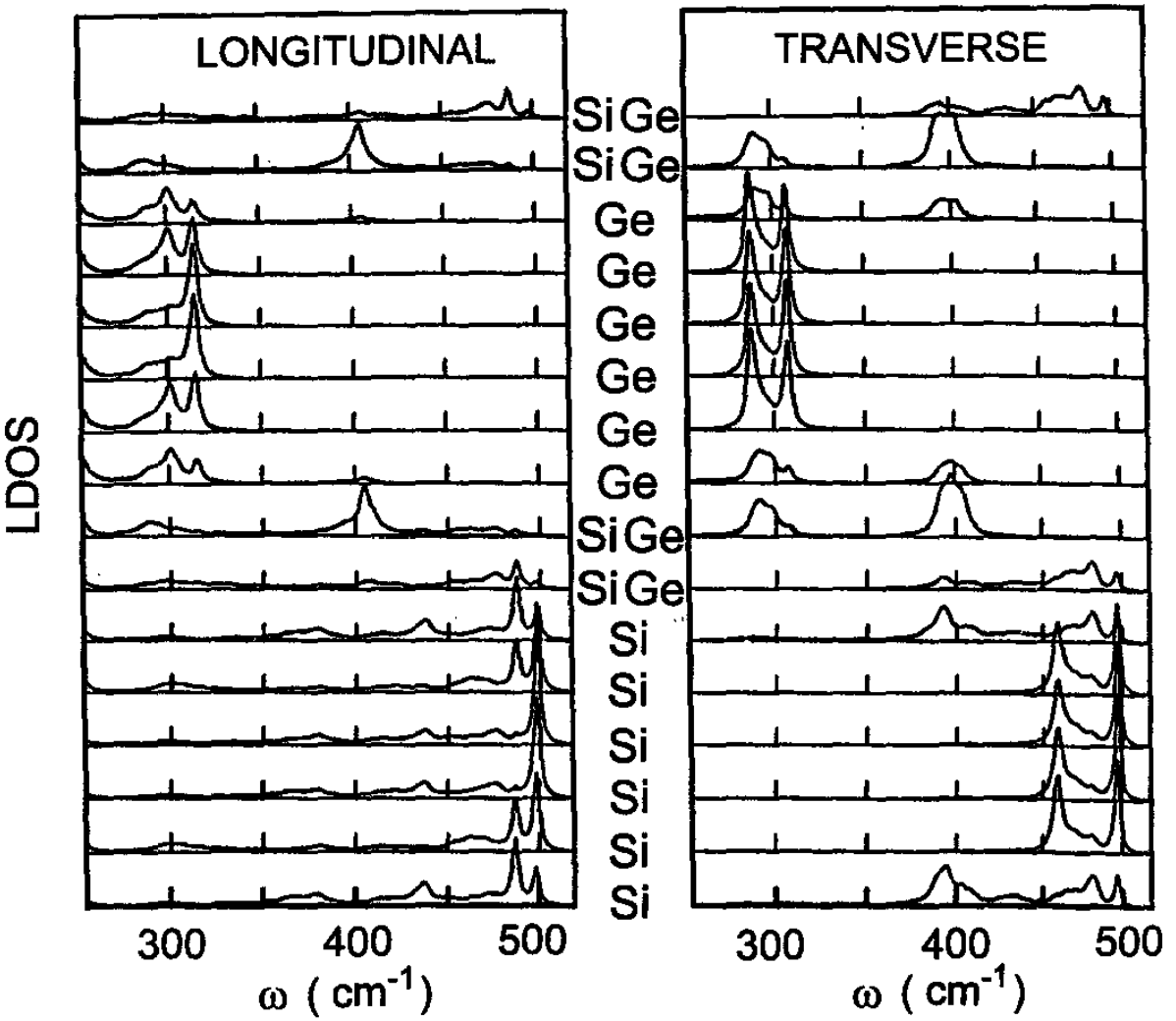
LONGITUDINAL
TRANSVERSE
LDOS
Si Ge
Si Ge
Ge
Ge
Ge
Ge
Ge
Ge
Si Ge
Si Ge
Si
Si
Si
Si
Si
Si
300
400
500
ω (cm-1)
300
400
500
ω (cm-1)

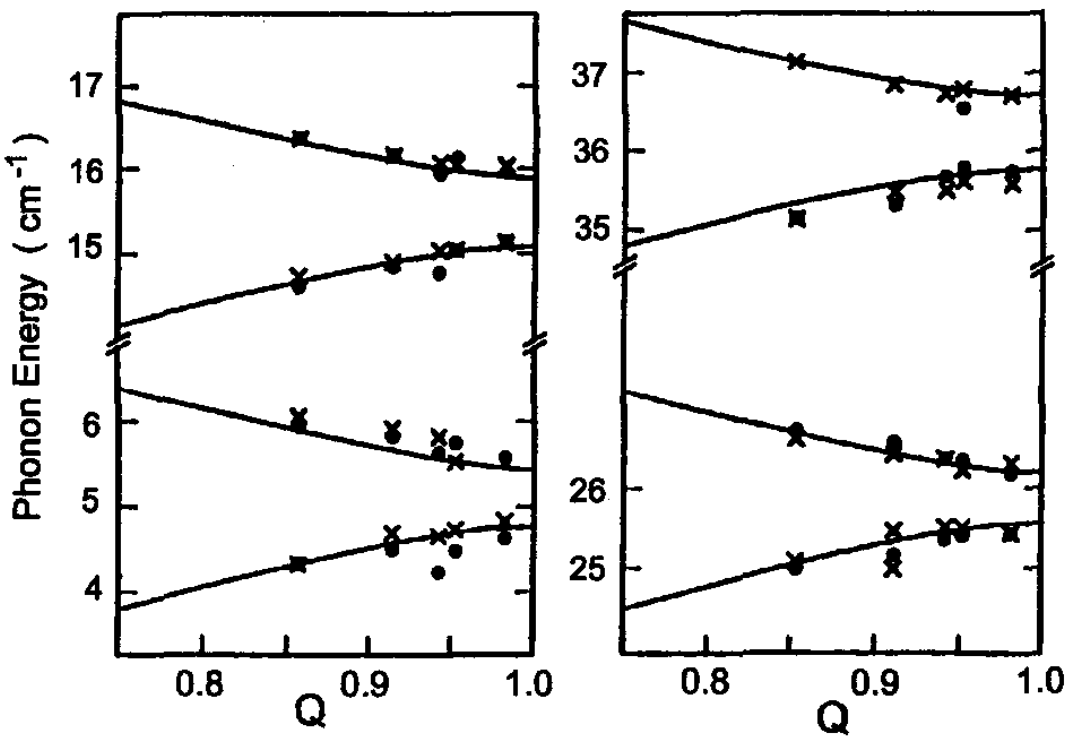
Phonon Energy (cm^{-1})
17
16
15
6
5
4
37
36
35
26
25
0.8
0.9
1.0
Q
0.8
0.9
1.0
Q

(a)

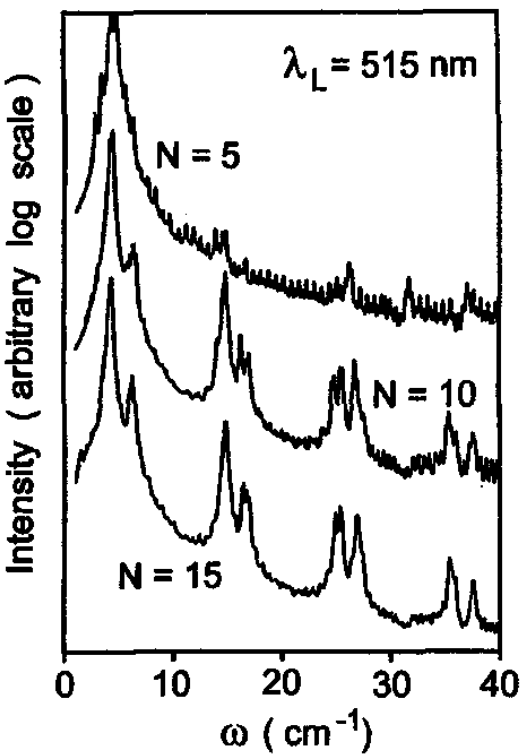
λ_L = 515 nm
N = 5
N = 10
N = 15
Intensity (arbitrary log scale)
0
10
20
30
40
ω (cm^{-1})

(b)

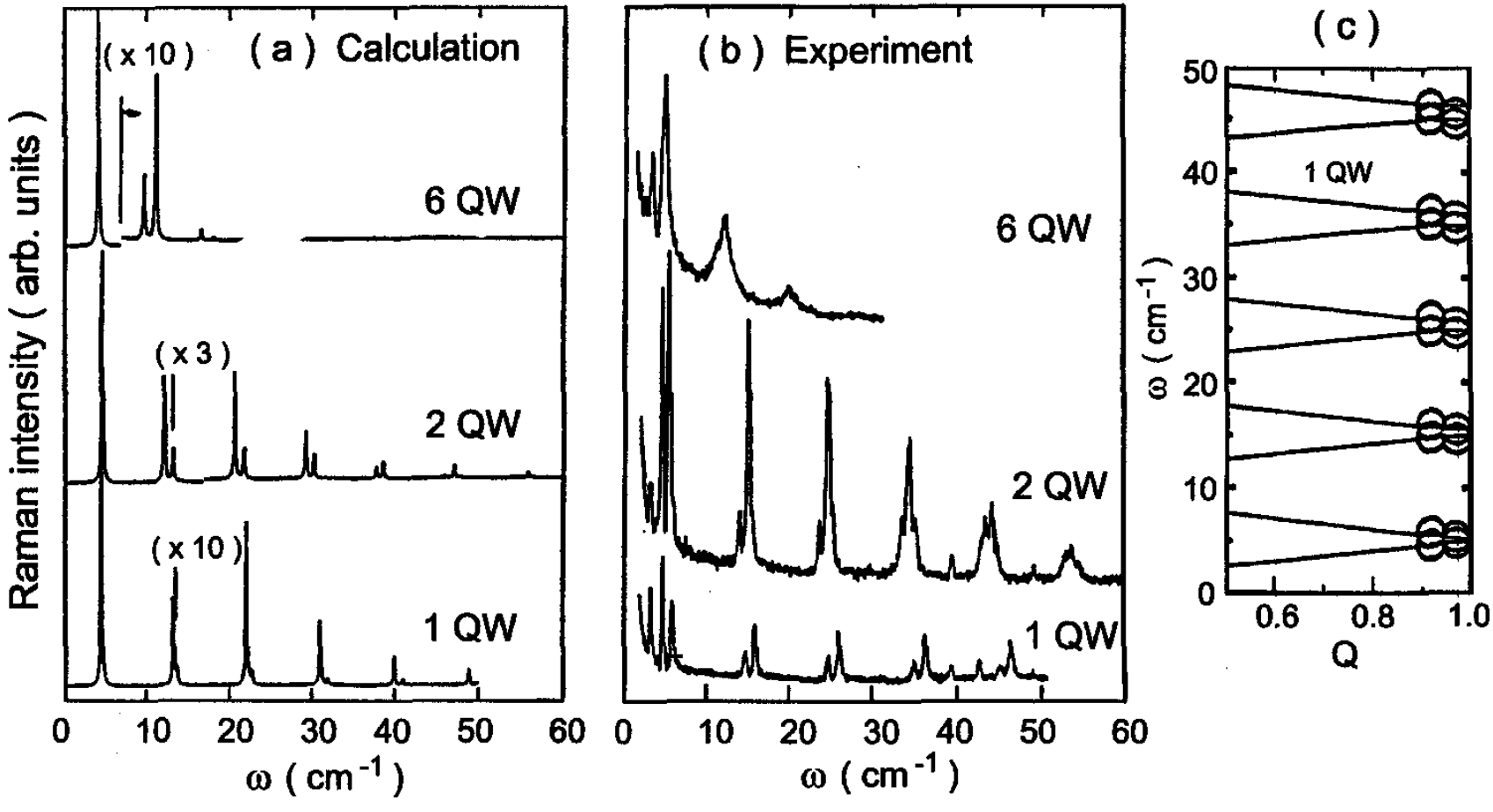
(a) Calculation
(x 10)
6 QW
(x 3)
2 QW
(x 10)
1 QW
Raman intensity (arb. units)
0 10 20 30 40 50 60
ω (cm -1)
(b) Experiment
6 QW
2 QW
1 QW
0 10 20 30 40 50 60
ω (cm -1)
(c)
1 QW
ω (cm -1)
0 10 20 30 40 50
0.6 0.8 1.0
Q

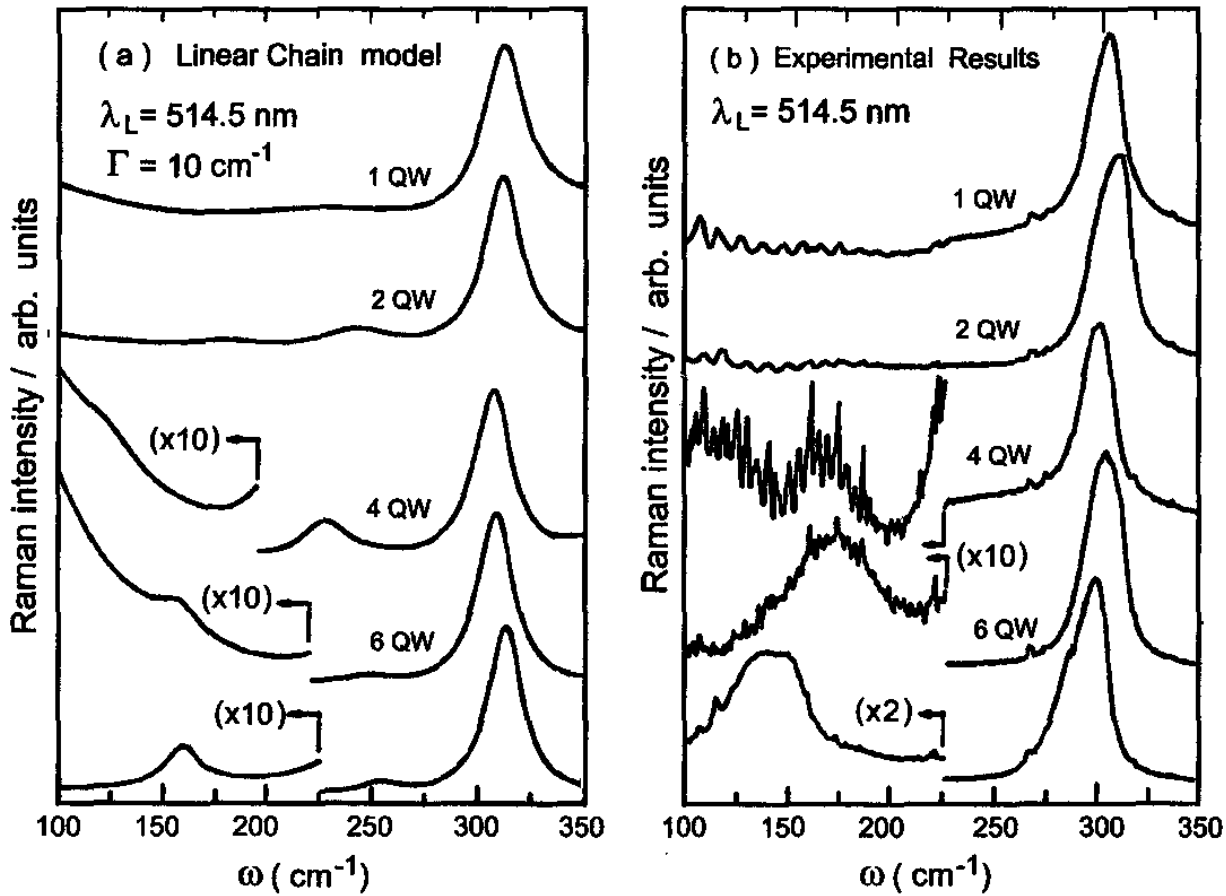
(a) Linear Chain model
λL= 514.5 nm
Γ = 10 cm-1
1 QW
2 QW
(x10)
4 QW
(x10)
6 QW
(x10)
Raman intensity / arb. units
100
150
200
250
300
350
ω (cm-1)
(b) Experimental Results
λL= 514.5 nm
1 QW
2 QW
4 QW
(x10)
6 QW
(x2)
Raman intensity / arb. units
100
150
200
250
300
350
ω (cm-1)

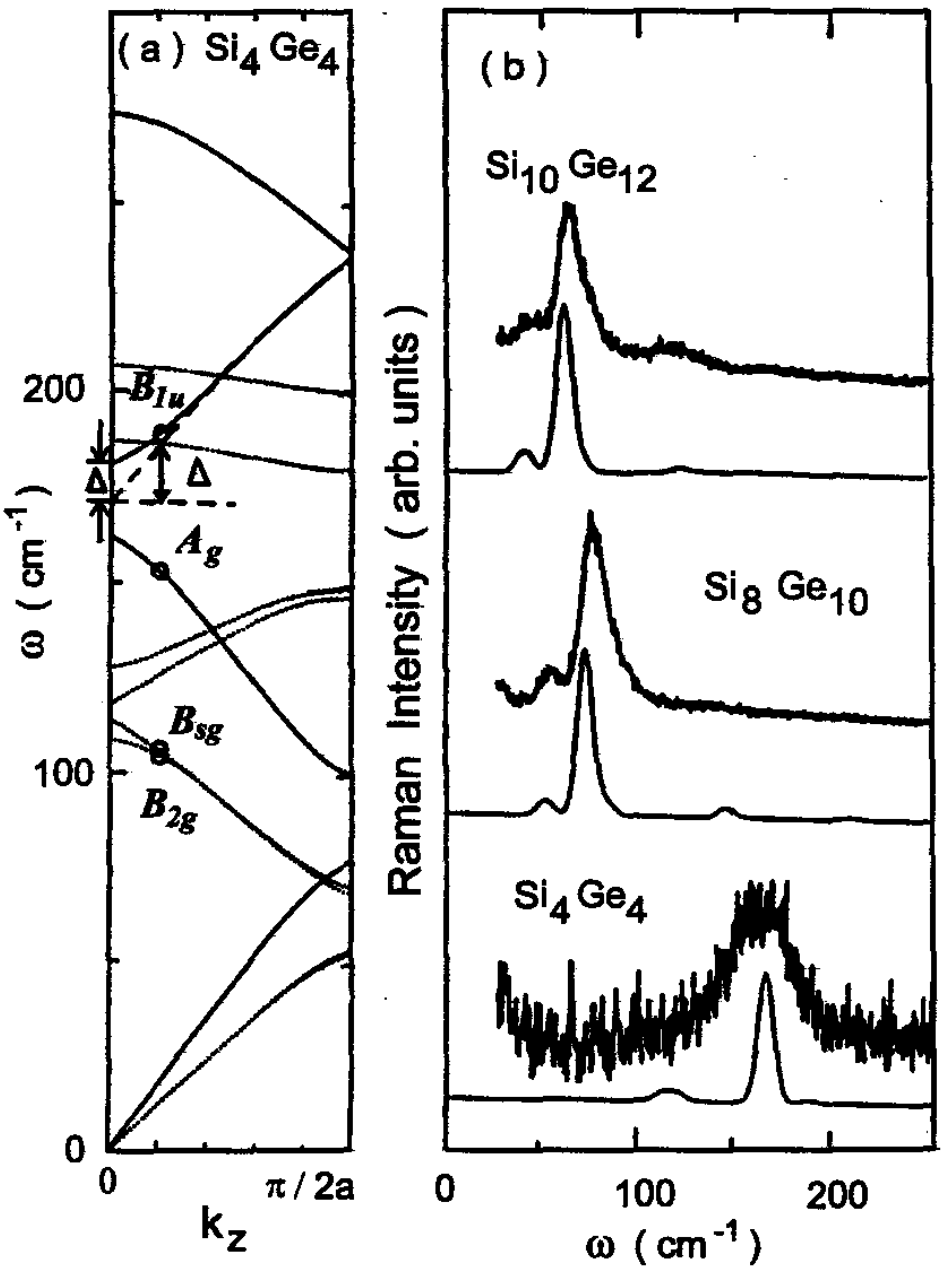
(a) Si_4Ge_4
200
100
0
ω (cm^{-1})
B_{1u}
Δ
Δ
A_g
B_{sg}
B_{2g}
0
π / 2a
k_z
(b)
$Si_{10}Ge_{12}$
Si_8Ge_{10}
Si_4Ge_4
Raman Intensity (arb. units)
0
100
200
ω (cm^{-1})

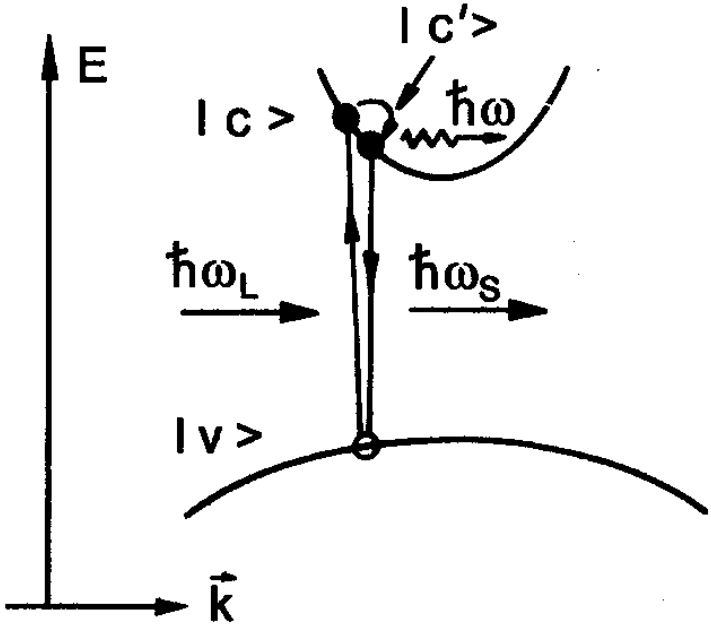

(a) A typical Ramam process

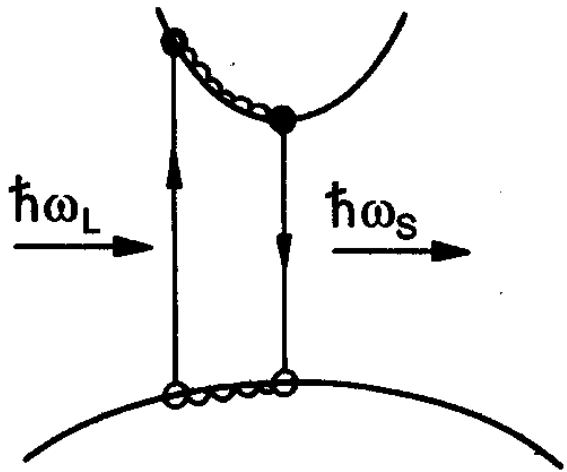

(b) A typical PL-process

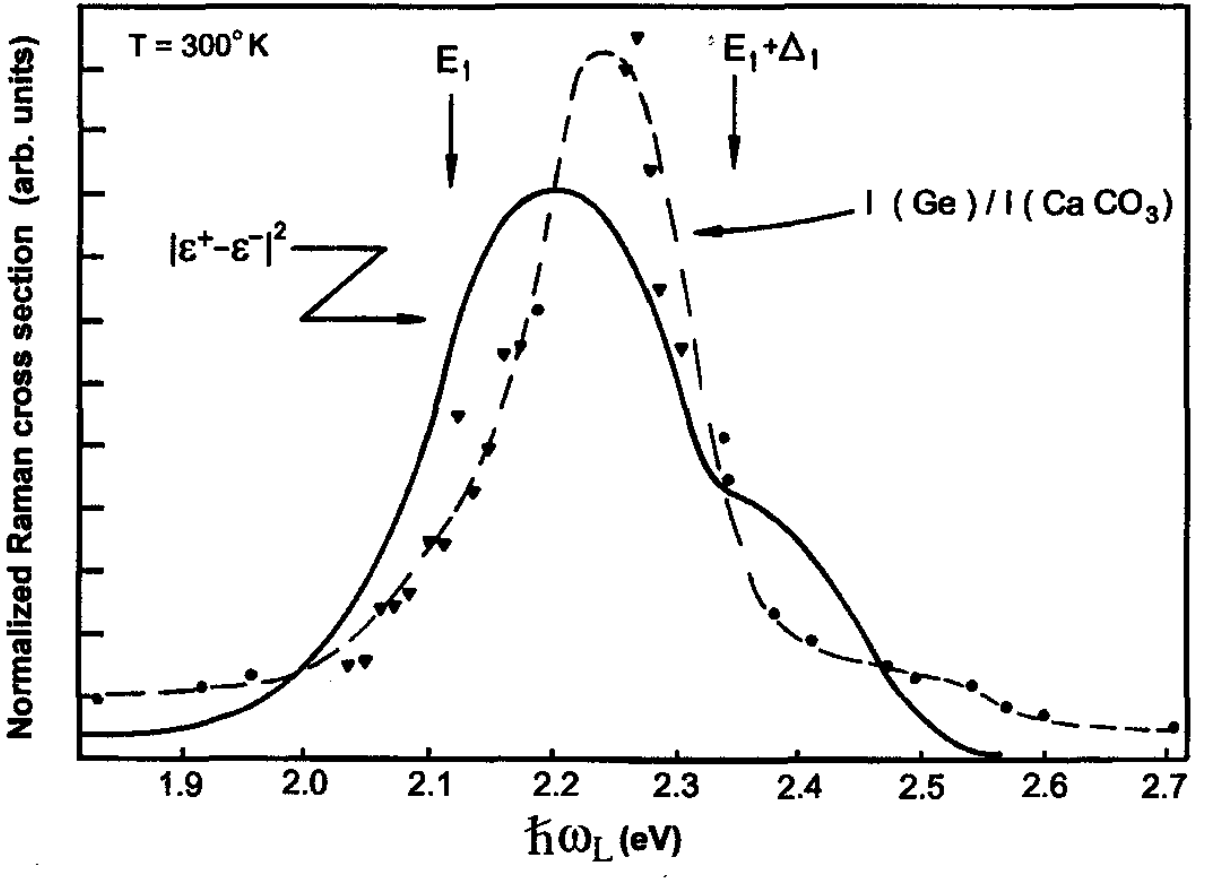
T = 300° K
E1
E1+Δ1
I (Ge) / I (Ca CO3)
|ε+-ε-|2
Normalized Raman cross section (arb. units)
1.9
2.0
2.1
2.2
2.3
2.4
2.5
2.6
2.7
ħωL (eV)

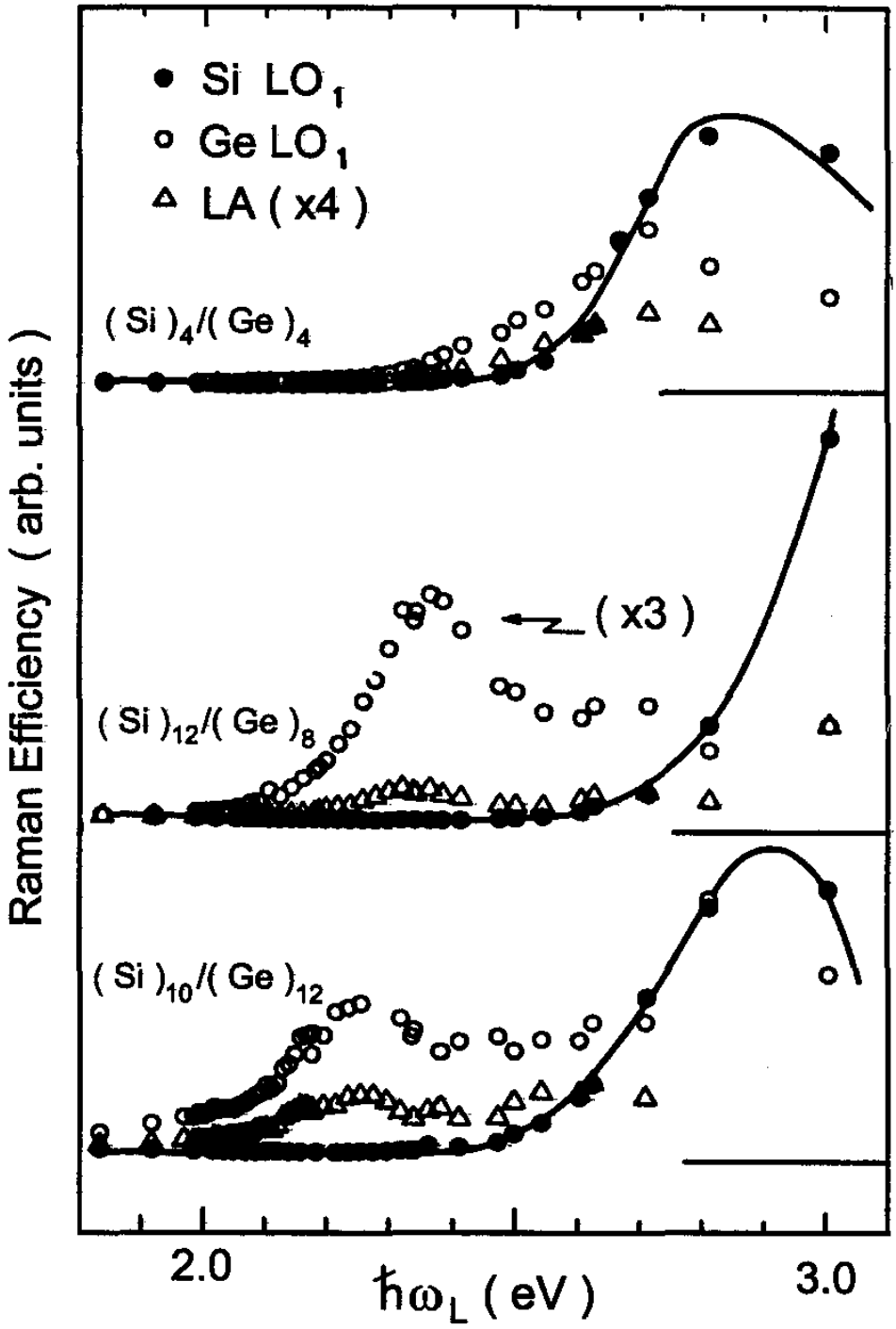
Si LO1
Ge LO1
LA (x4)
(Si)4/(Ge)4
(Si)12/(Ge)8
(x3)
(Si)10/(Ge)12
Raman Efficiency (arb. units)
2.0
3.0
ħωL (eV)

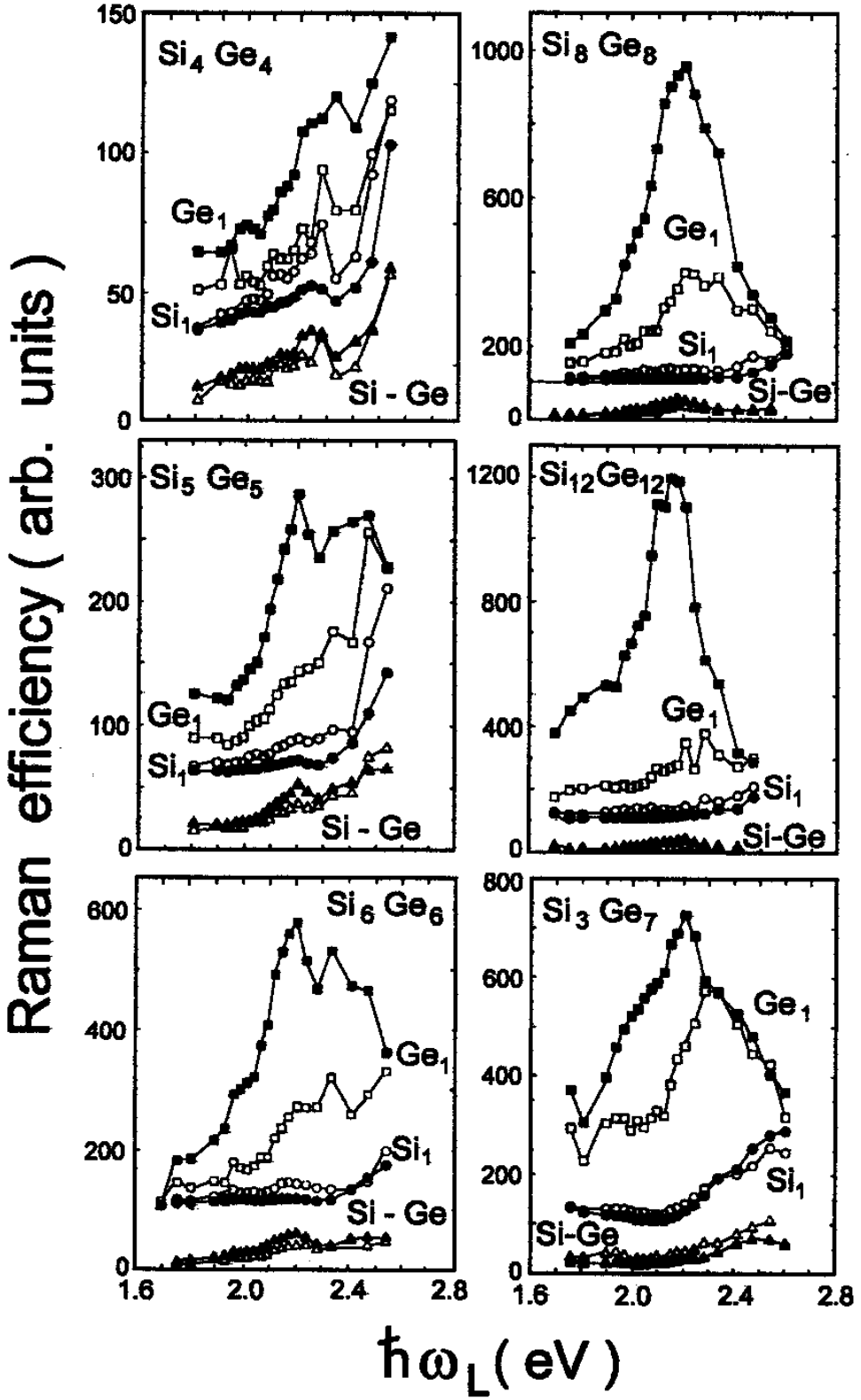
Raman efficiency (arb. units)
$\hbar\omega_L$ (eV)
$Si_4 Ge_4$
$Si_8 Ge_8$
$Si_5 Ge_5$
$Si_{12} Ge_{12}$
$Si_6 Ge_6$
$Si_3 Ge_7$
Ge_1
Si_1
Si - Ge
Si-Ge
150
100
50
0
1000
600
200
300
1200
800
400
600
400
200
800
1.6
2.0
2.4
2.8

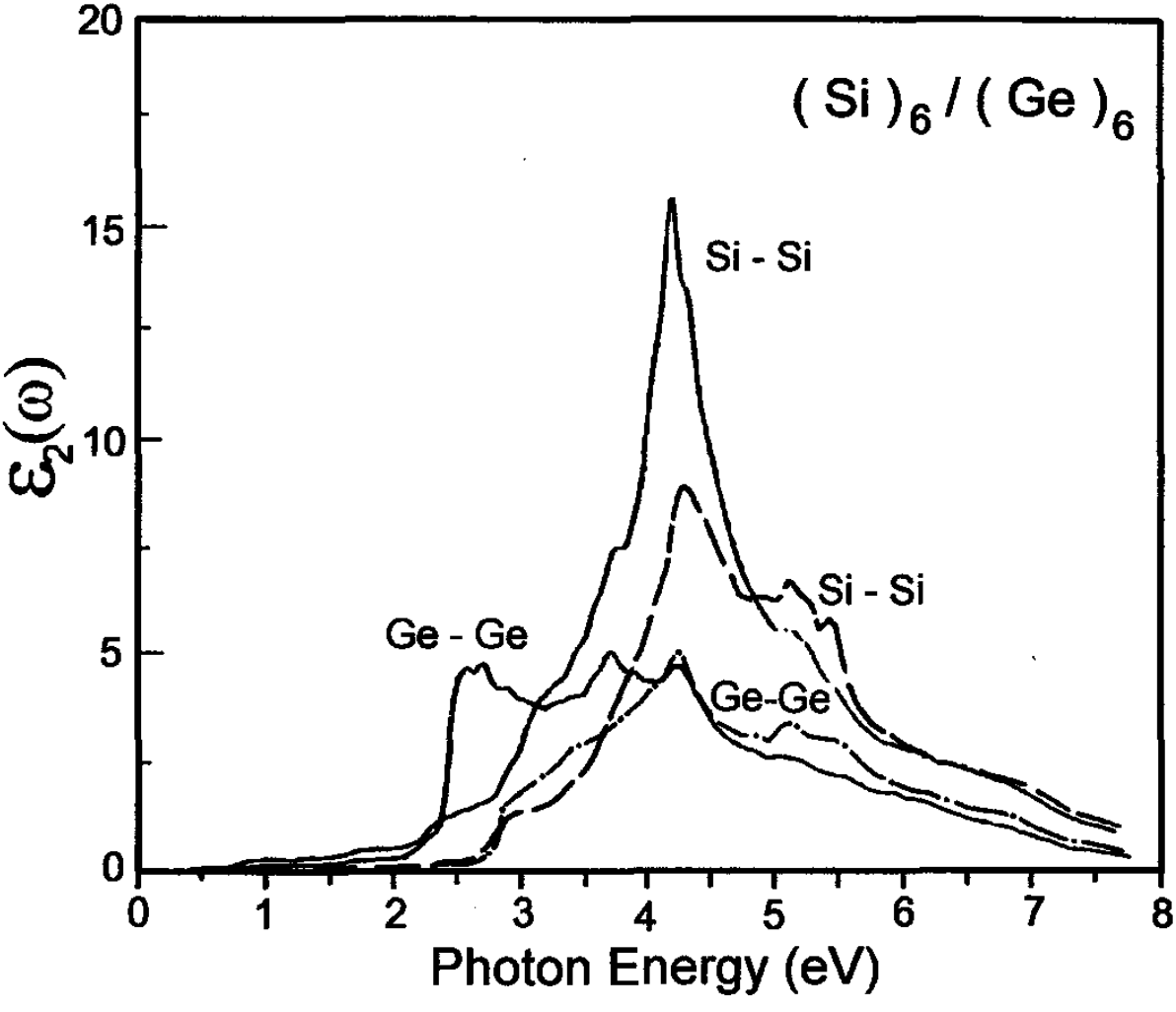
(Si)6 / (Ge)6
Si - Si
Si - Si
Ge - Ge
Ge-Ge
ε2(ω)
Photon Energy (eV)
0
5
10
15
20
0
1
2
3
4
5
6
7
8

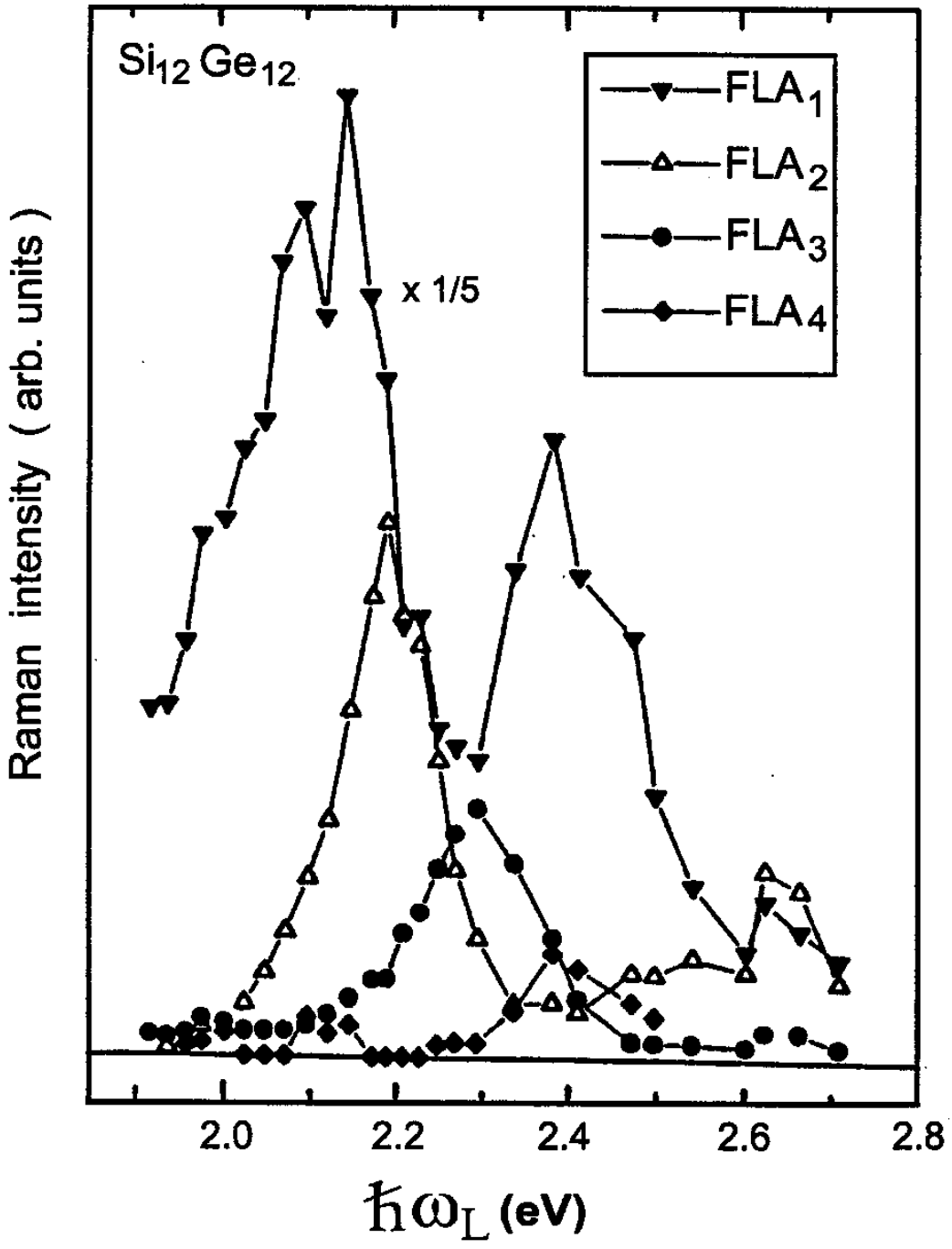
Si12 Ge12
FLA1
FLA2
FLA3
FLA4
x 1/5
Raman intensity (arb. units)
2.0
2.2
2.4
2.6
2.8
ħω_L (eV)

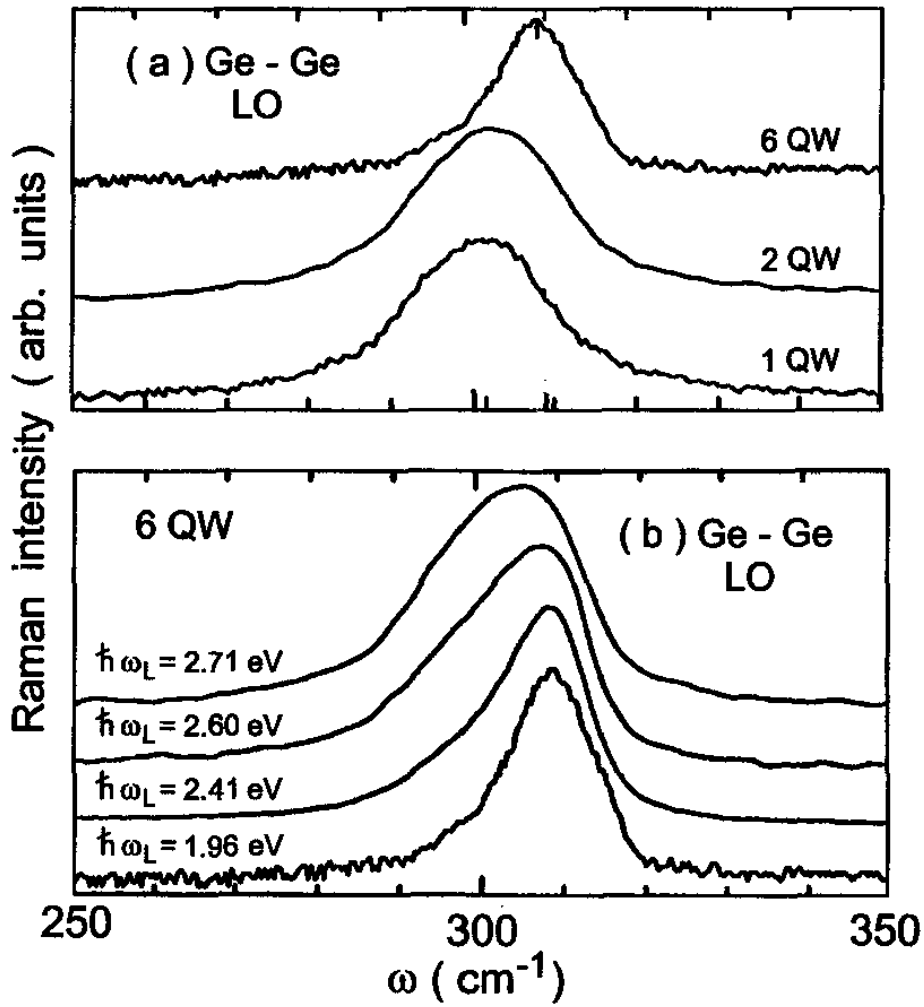
(a) Ge - Ge
LO
6 QW
2 QW
1 QW
6 QW
(b) Ge - Ge
LO
ħω_L = 2.71 eV
ħω_L = 2.60 eV
ħω_L = 2.41 eV
ħω_L = 1.96 eV
Raman intensity (arb. units)
250
300
350
ω (cm^-1)

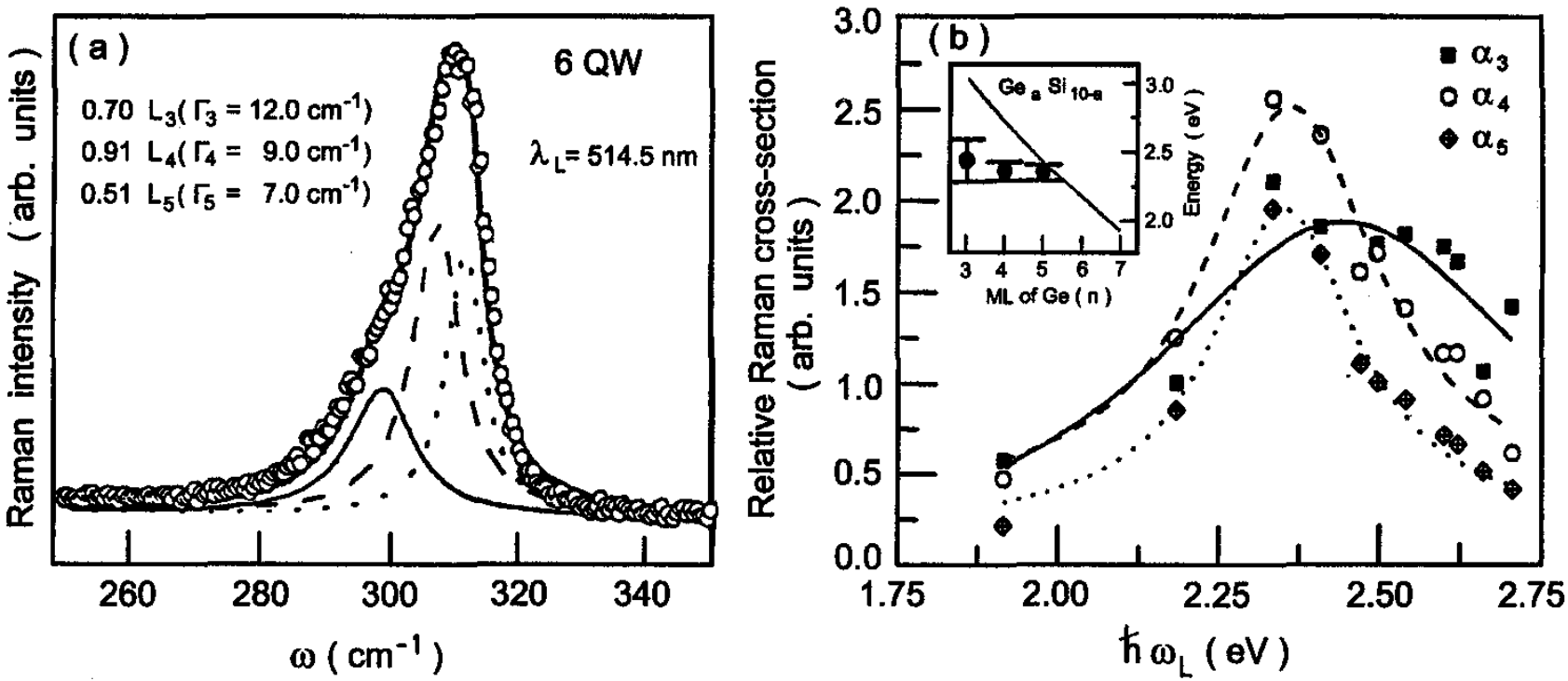
(a)
6 QW
0.70 L3(Γ3 = 12.0 cm-1)
0.91 L4(Γ4 = 9.0 cm-1)
0.51 L5(Γ5 = 7.0 cm-1)
λL= 514.5 nm
Raman intensity (arb. units)
260
280
300
320
340
ω (cm-1)
(b)
α3
α4
α5
Relative Raman cross-section (arb. units)
3.0
2.5
2.0
1.5
1.0
0.5
0.0
1.75
2.00
2.25
2.50
2.75
ħ ωL (eV)
Ge n Si 10-n
Energy (eV)
3.0
2.5
2.0
3
4
5
6
7
ML of Ge (n)

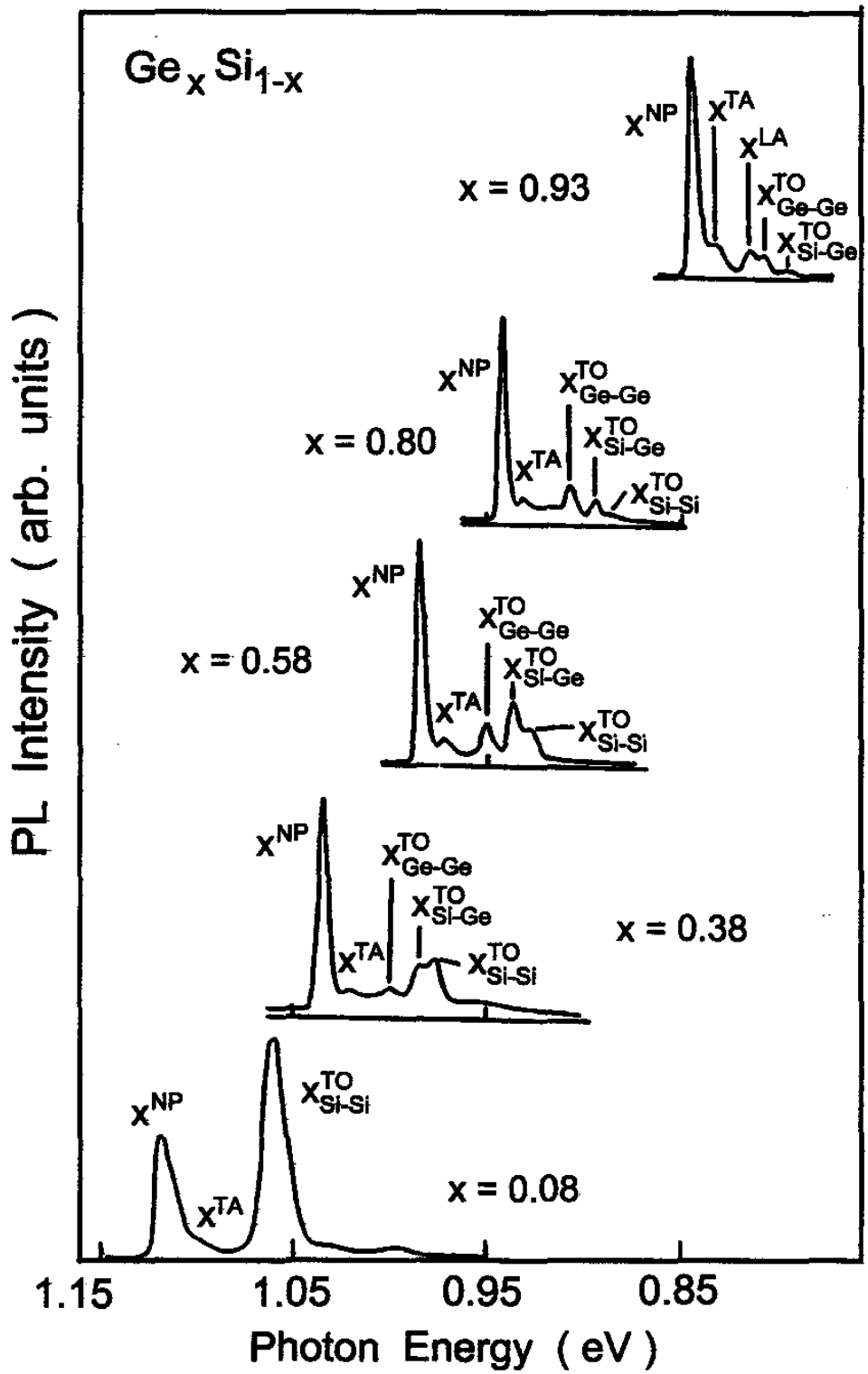
Ge x Si 1-x
x = 0.93
x = 0.80
x = 0.58
x = 0.38
x = 0.08
X NP
X TA
X LA
X TO Ge-Ge
X TO Si-Ge
X TO Si-Si
PL Intensity (arb. units)
1.15
1.05
0.95
0.85
Photon Energy (eV)

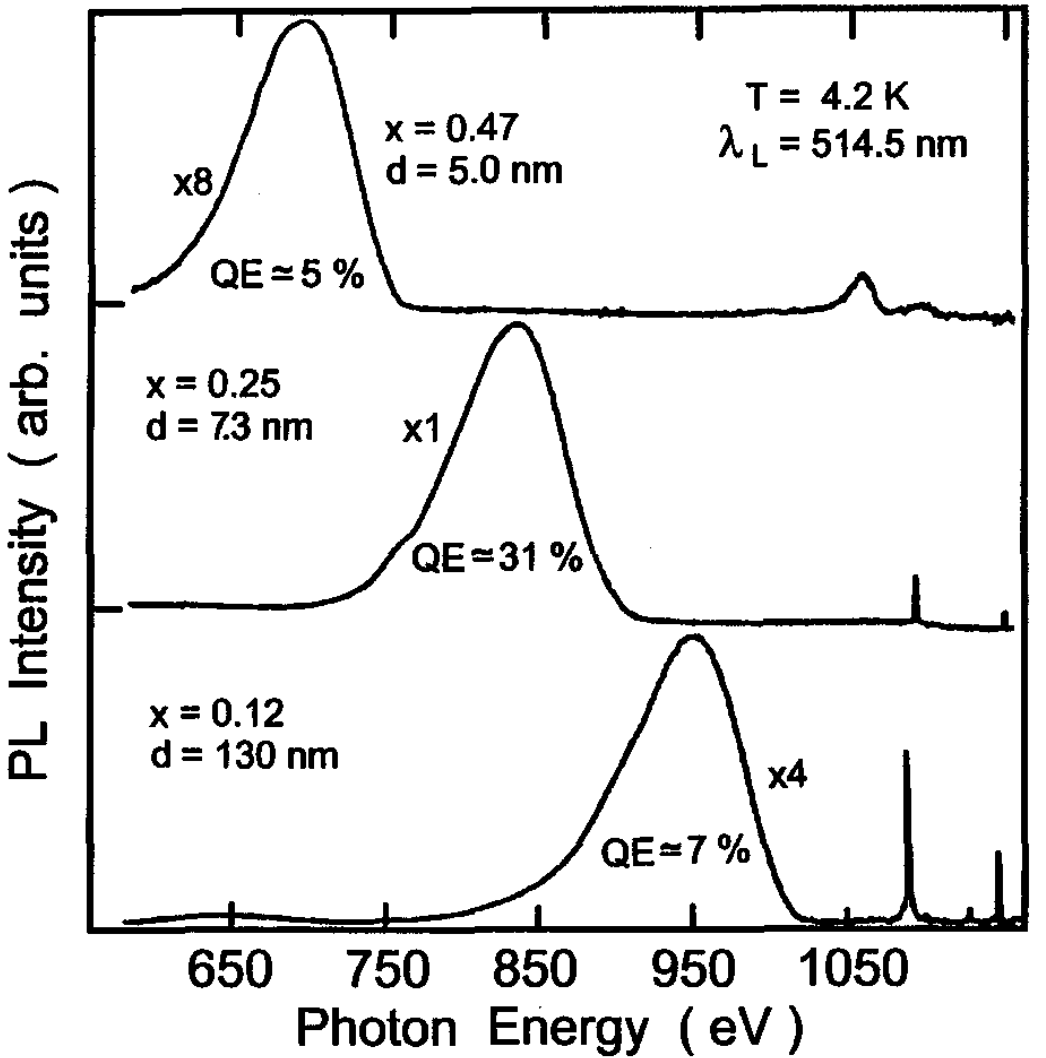
T = 4.2 K
λL = 514.5 nm
x = 0.47
d = 5.0 nm
x8
QE ≃ 5 %
x = 0.25
d = 7.3 nm
x1
QE ≃ 31 %
x = 0.12
d = 130 nm
x4
QE ≃ 7 %
PL Intensity (arb. units)
650
750
850
950
1050
Photon Energy (eV)

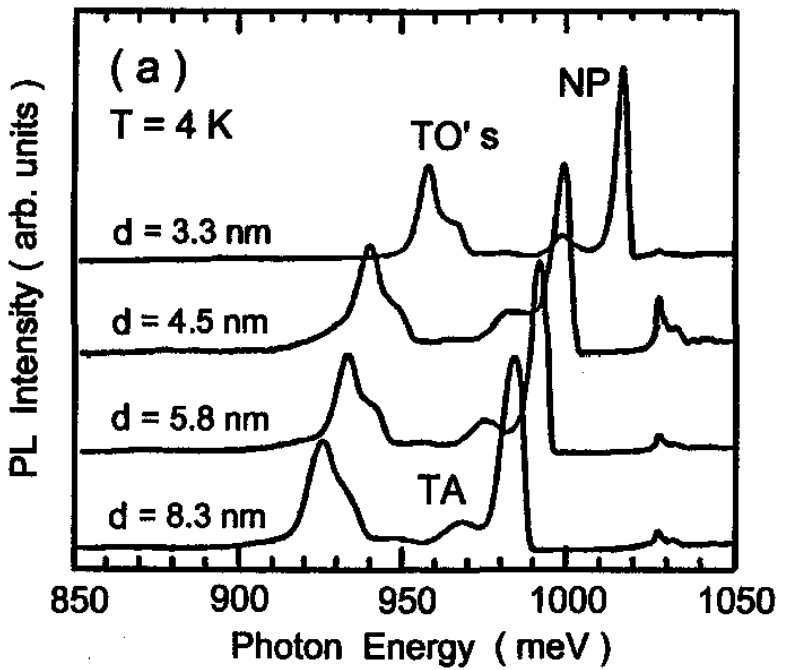
(a)
T = 4 K
NP
TO's
d = 3.3 nm
d = 4.5 nm
d = 5.8 nm
TA
d = 8.3 nm
PL Intensity (arb. units)
850
900
950
1000
1050
Photon Energy (meV)

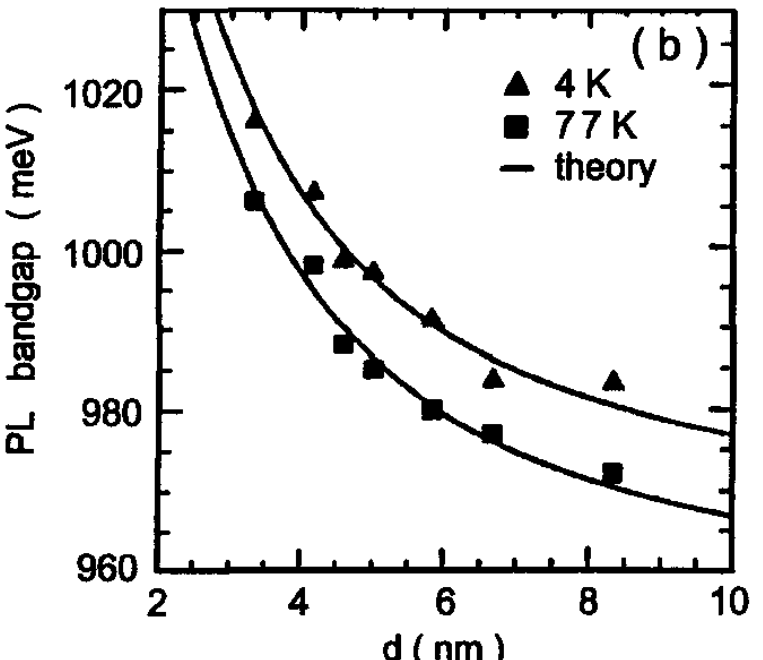
(b)
4 K
77 K
theory
PL bandgap (meV)
1020
1000
980
960
2
4
6
8
10
d (nm)

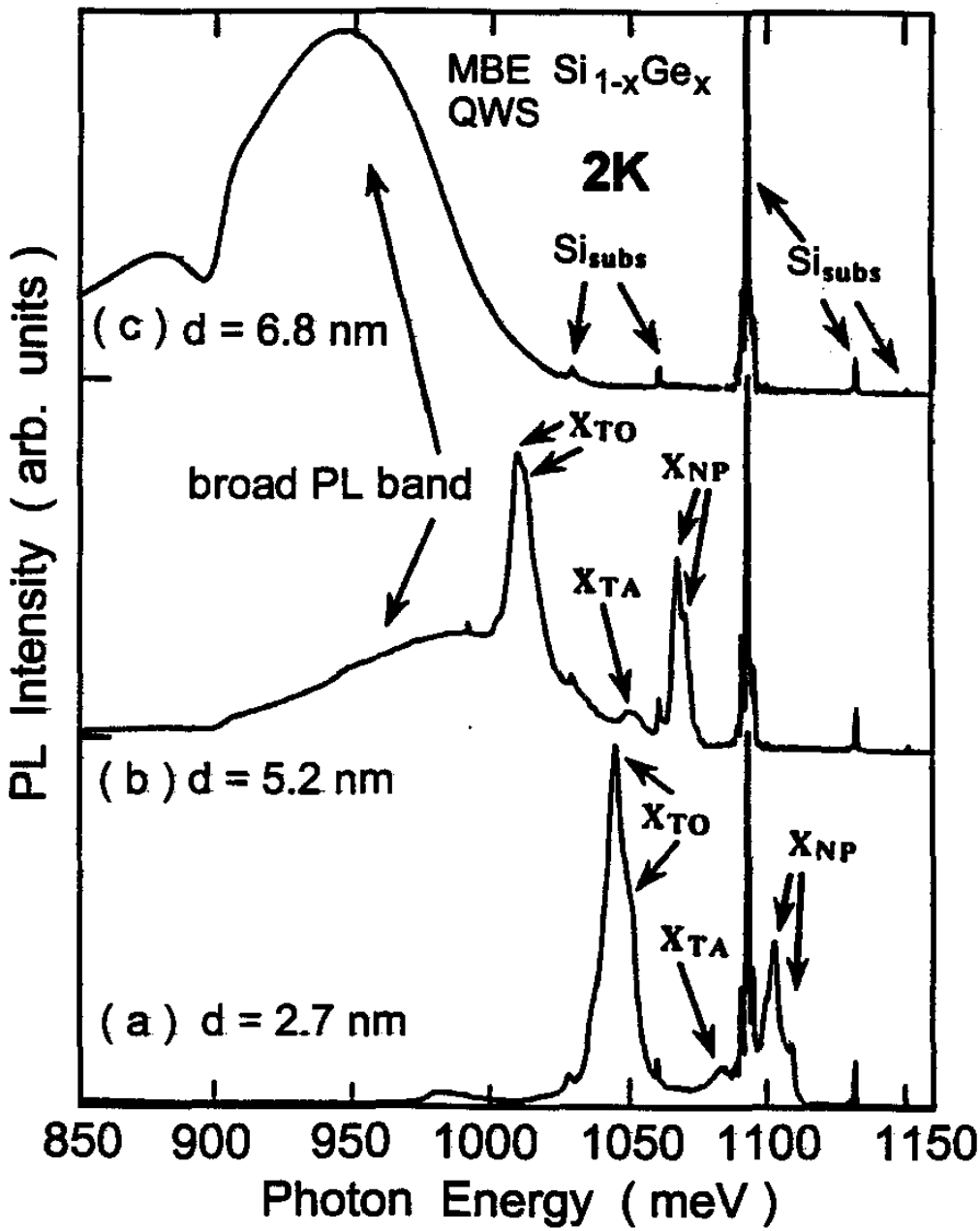
MBE Si 1-x Ge x
QWS
2K
Si subs
Si subs
(c) d = 6.8 nm
broad PL band
X TO
X NP
X TA
(b) d = 5.2 nm
X TO
X NP
X TA
(a) d = 2.7 nm
PL Intensity (arb. units)
850
900
950
1000
1050
1100
1150
Photon Energy (meV)

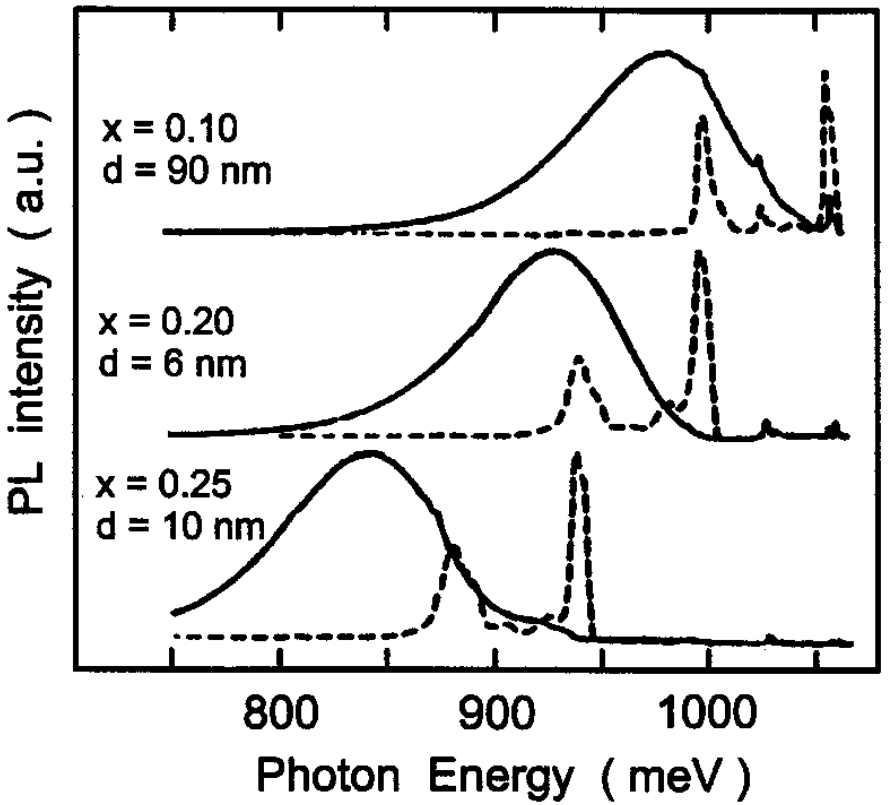
x = 0.10
d = 90 nm
x = 0.20
d = 6 nm
x = 0.25
d = 10 nm
PL intensity (a.u.)
800
900
1000
Photon Energy (meV)

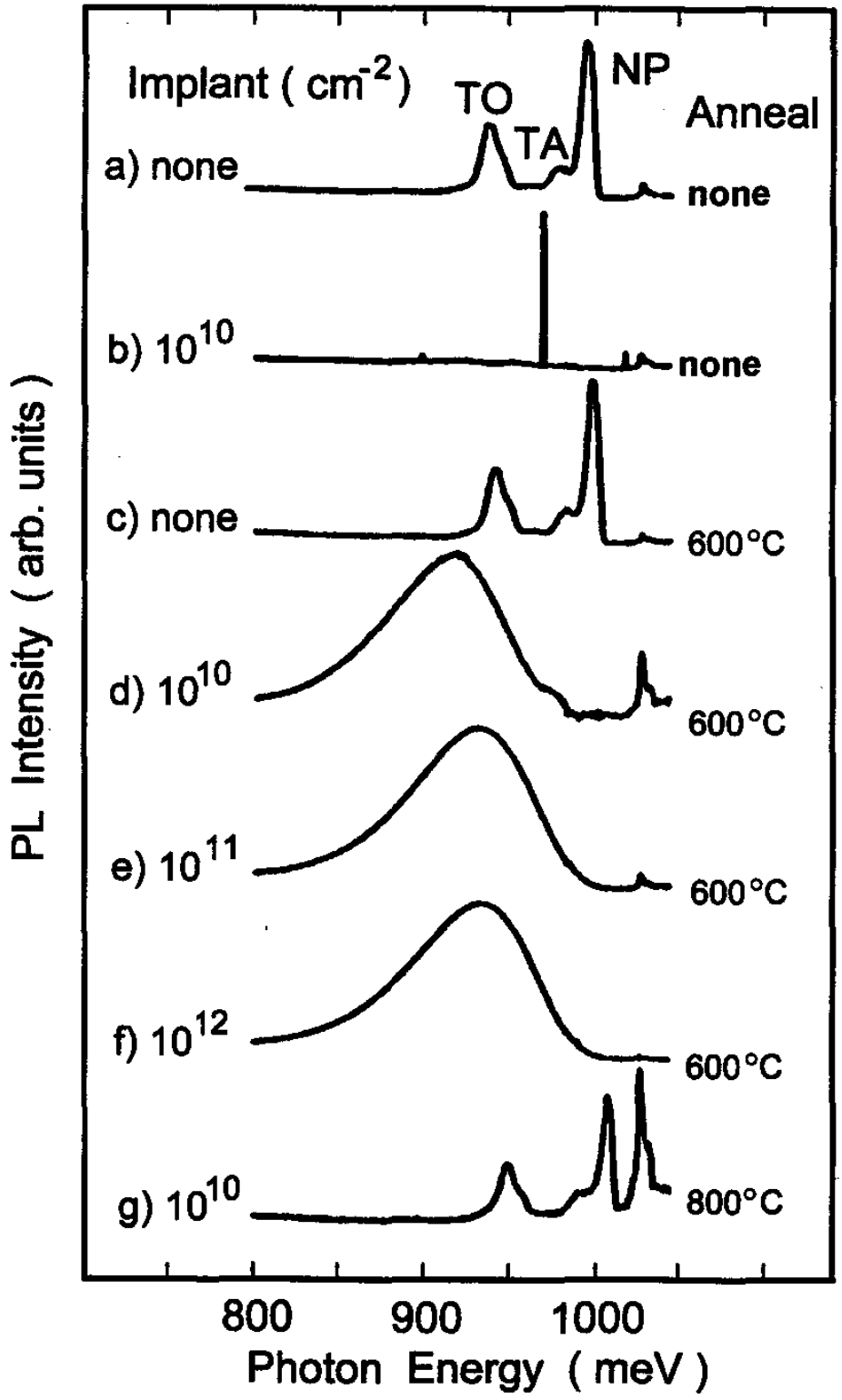
Implant (cm-2)
TO
TA
NP
Anneal
a) none
none
b) 10^10
none
c) none
600°C
d) 10^10
600°C
e) 10^11
600°C
f) 10^12
600°C
g) 10^10
800°C
PL Intensity (arb. units)
800
900
1000
Photon Energy (meV)